Thèse n° 10286

Topological Effects in Carbon-based Two-dimensional Nanostructures

Présentée le 26 septembre 2023

Faculté des sciences de base
Chaire de physique numérique de la matière condensée
Programme doctoral en physique

pour l'obtention du grade de Docteur ès Sciences

par

Yifei GUAN

Acceptée sur proposition du jury

Prof. F. Mila, président du jury
Prof. O. Yazyev, directeur de thèse
Prof. T. Neupert, rapporteur
Prof. M. Katsnelson, rapporteur
Prof. R. Fleury, rapporteur

École
polytechnique
fédérale
de Lausanne

2023

When we say we are a pile of atoms, we do not mean we are *merely* a pile of atoms,
because a pile of atoms which is not repeated from one to the other
might well have the possibilities which you see before you in the mirror.

——Richard Feynman

Ascendit a terra in coelum, iterumque descendit in terram,
et recipit vim superiorum et inferiorum.

——Emerald Tablet

Acknowledgements

First I would like to thank my thesis supervisor Prof. Oleg V. Yazyev. Oleg has greatly helped me with writing skills and doing presentations. Meanwhile, I was influenced deeply from Oleg in organizing my works and scientific datas - which are as important as producing the results. In research, Oleg also gives me the chance and trust to realize my own ideas and to participate in various collaborations, while he's always willing to provide his insight and advice. I am grateful for the support and guidance given throughout my Ph.D.

Followingly, I want to thank all the jury members, Prof. Frédéric Mila, Prof. Romain Fleury, Prof. Titus Neupert and Prof. Mikhail Katsnelson, for accepting the invitation and putting their time in reading the thesis.

I also want to give special thanks to Dr. Quansheng Wu and Dr. Shengnan Zhang, for their help in both science and life. It is not always easy to start a new series of research in a foreign land, since one has to hand on all the techniques while settling down to the place. Thanks to their help, my early stage of doctorate went quite smooth. Quansheng shared quite a lot of his experience on computational physics and the theory of topological insulators, which greatly boosted my research. Apart from that, they also provided me lots of useful informations about life in Lausanne.

This thesis involves different aspects of research, which would not be possible without the help from my collaborators. Therefore, I want to express my gratitude to Dr. Alex Kruchkov, Dr. Tomáš Bzdušek and Dr. Adrien Bouhon for the collaborations on theoretical works. I have learned a lot during the projects working with them. I also enjoyed the collaboration on experimental projects, with researchers from all over the Europe, Prof. Vincent Renard in Université Grenoble Alpes, Clement Dutreix in Univ. Bordeux and Edoardo Lopriore from the group of Prof A. Kis. As a theoretician, discussing with them helps me to think in a more visualized manner, which brings both topics of research and new perspectives to physics.

The years of 2020 and 2021 has been quite hard to go through, and they could be even tougher without the support from my friends. I thank Bingkun Qi, Cheng Shi, Yikai Yang, for hanging out (online and offline) during the past years as well as exchanging ideas in research. Starting from 2021, I was actively discussing with the members in LQP group: Jin Jiang, Zekang and Dr. Cheng Shen. They keep me updated with the newest trend and progress in twistronics. I also learned a lot from my friends Zhe Zhang and Jiyu Chen, who are working in similar disciplines as mine.

I have spent a lot of time working in the same room with my wonderful office mates Dr. Kristiāns Černevičs and Xiaoqian Liu. I am also benefited from the other members I encoun-

tered in the C3MP group: Dr. Vamshi Katukuri, Dr. Daniel Gosalbez, Dr. Marta Brzezinska, Dr. Ravi Yadav, Nikita Tepliakov, Oleg Malanyuk, Johan Felisaz, Gian Parusa, Henning Zhang and Dr. Michele Pizzochero, who have build up the friendly and delightful atmosphere of the group. I want to give a big thanks to Kristiāns and Xiaoqian who have helped with proofreading the manuscript, and Johan for taking care of examining the French abstract.
Additionally, I want to thank the secretaries Tanya Castellino, Annick Evequoz and Patricia Byron for their help with scientific and administration issues.
Finally, I would like to express a huge gratitude to my family, for their persistent love and support over the past years — that has been the biggest motivation of mine.

Lausanne, June 29, 2023

Abstract

Recent advances on low-dimensional and topological materials has greatly inspired the research in condensed matter physics. This thesis is devoted to the computational and theoretical study of topological effects in two-dimensional materials, especially nanostructures based on ne. The theoretical research contained in the thesis is in different levels: minimal models and tight-binding modeling of materials. Electronic interactions are discussed effectively as well.

In the first part of the thesis, I provide the theoretical study on a specific family of topological insulators: the Euler insulators, which are characterized by the Euler class. Noticing the relation between the mathematical expression of the Chern class and the Euler class, there rises the question about the edge states and magnetotransport features of Euler insulators. I show that the Euler insulators carry a series of signatures in their Landau levels. In contrast to trivial bands, the topological Euler bands exhibit a Landau level broadening under magnetic fields. Moreover, I found that the broadening becomes more significant in the case of larger Euler numbers. With the flat and degenerated bands serving as the simplest limit for investigating Euler insulators, I further unveil the edge signatures of Euler insulators. In the case of flat bands, the edge states of Euler insulators exhibit a series of crossings. The order of the crossings gives the largest Euler number, which can be seen from interpolating edge modes by a set of polynomials.

The second part of the thesis presents a collection of research on topological effects in twisted multilayer graphene. The computational studies are performed using atomistic tight-binding (TB) models, providing the topological phase in twisted multilayer systems. I explore the topological phase and quantum geometric tensors of twisted bilayer graphene, and the interplay between band topology and spin textures. To compare with the transport measurements, I also provide the results of Hofstadter butterfly spectra for different topological phases. The idea of probing the flat-band topology with quantum Hall response is then verified in an example material: twisted double bilayer graphene. In addition to the Hofstadter spectra, I also discuss the topological effects on electronic interactions in a qualitative manner.

Finally, I present the computational study of electronic transmission in wrinkled graphene sheets. By comparing the transmission in commensurate and incommensurate scenarios, I found a suppressed back-scattering in the incommensurate wrinkles. Therefore, I conclude that layer commensuration plays an important role in the transport of wrinkled 2D materials. The results provide guidelines to controlling the transport properties of graphene in presence of out-of-plane disorder.

Keywords: topological insulator, graphene, twisted multilayer graphene, quantum transport, quantum Hall effect

Résumé

Les avancées dans les matériaux topologiques et à basse dimension grandement inspiré la recherche en physique de la matière condensée.

Cette thèse est consacrée à l'étude théorique et numérique des effets topologiques dans les matériaux bidimensionnels, en particulier les nanostructures basées sur le graphène. La recherche théorique contenue dans la thèse se situe à trois niveaux différents : des modèles minimaux, une modélisation par liaisons fortes des matériaux et des interactions effectives.

Dans la première partie de la thèse, nous présentons l'étude théorique d'une famille spécifique d'isolants topologiques : les isolants topologiques d'Euler, caractérisés par la classe d'Euler. En remarquant la relation entre l'expression mathématique de la classe de Chern et la classe d'Euler, une question se pose quant aux états de bord et aux caractéristiques de magnétotransport des isolants d'Euler. Nous montrons que les isolants d'Euler portent une série de signatures dans leurs niveaux de Landau. Contrairement aux bandes triviales, les bandes d'Euler topologiques présentent un élargissement des niveaux de Landau lorsqu'ils sont soumis à un champ magnétique. De plus, nous avons constaté que cet élargissement est d'autant plus important que le nombre d'Euler est grand. Alors que les bandes planes et dégénérées servent de limite pour l'étude des isolants d'Euler, nous révélons davantage les signatures de bord des isolants d'Euler en prenant la limite de bande plane exacte. Dans le cas des bandes planes, les états de bord des isolants d'Euler présentent une série de croisements. L'ordre des croisements donne le plus grand nombre d'Euler, qui peut être vu en interpolant les modes de bord par un ensemble de polynômes.

La partie II de la thèse est une collection de recherches sur les effets topologiques dans le graphène multicouche tordu. Les études computationnelles sont réalisées avec des modèles de liaisons fortes atomistiques, permettant de calculer la phase topologique dans les systèmes multicouches tordus. Nous explorons la phase topologique et les tenseurs géométriques quantiques du graphène bicouche tordu, ainsi que l'interaction entre la topologie de bande et les textures de spin. Pour comparer avec les mesures de transport, nous fournissons également les résultats des papillons de Hofstadter pour différentes phases topologiques. L'idée de sonder la topologie de bande plane avec la réponse de Hall quantique est ensuite vérifiée dans un matériau d'exemple : le graphène bicouche double tordu. En plus des spectres de Hofstadter, nous discutons également des effets topologiques sur les interactions électroniques de manière qualitative.

Enfin, dans la partie III, nous présentons l'étude computationnelle de la transmission électronique dans des feuilles de graphène froissées. En comparant la transmission dans des scénarios commensurables et incommensurables, nous avons découvert une suppression de la rétrodiffusion dans les rides incommensurables. Par conséquent, nous concluons que la commensuration des couches joue un rôle important dans le transport des matériaux 2D froissés.

Mot clés : d'isolants topologiques, graphène, graphène multicouche tordu, transport quantique, effets Hall quantique

Contents

Acknowledgements **i**

Abstract (English/Français) **iii**

1 Introduction **1**
- 1.1 Topology of bands . . . 2
  - 1.1.1 From quantized Hall effect to Chern numbers . . . 3
  - 1.1.2 Euler numbers . . . 4
  - 1.1.3 Role of symmetries: tenfold classification and EBR . . . 5
- 1.2 Manifestation of topology in materials . . . 6
- 1.3 Graphene and twisted bilayer graphene . . . 10
  - 1.3.1 Hamiltonian of graphene . . . 11
  - 1.3.2 Berry phase and topological effects of Dirac cones . . . 12
  - 1.3.3 Twisted multilayer graphene . . . 12
- 1.4 Outline of the thesis . . . 15

2 Theory **17**
- 2.1 Schrödinger equation and Band theory . . . 17
- 2.2 Tight-binding Hamiltonian for electrons in solids . . . 18
- 2.3 The Slater-Koster model calculations . . . 20
- 2.4 Wilson loop calculation of topological numbers . . . 21
- 2.5 Investigating electron interaction on the basis of TB calculations . . . 23
- 2.6 Landauer-Buttiker Transmission and beyond . . . 24
- 2.7 Lanczos recursions and the calculation of Hofstadter butterfly in large systems 25

I Topological aspects of 2D materials **27**

3 Landau Levels of the Euler Class Topology **29**
- 3.1 Introduction . . . 29
- 3.2 Euler class topology . . . 31
- 3.3 Four-band real symmetric Hamiltonian . . . 32
- 3.4 Hofstadter Spectrum . . . 34
- 3.5 Flat-band limit . . . 35
- 3.6 Dispersive bands . . . 37

3.6.1 Magnetic sub-gaps 39
3.7 Discussion 40
3.8 The modelling of Euler insulating phases 41
3.8.1 The geometric approach 41
3.8.2 Topology of the Bloch Hamiltonian 42
3.8.3 Tight-binding Hamiltonian 44
3.9 From complex to real basis 44
3.10 Mirror Chern number and Euler class 47
3.10.1 All degenerate balanced phases are mirror-symmetric 51
3.10.2 Degenerate imbalanced phases 52
3.11 Hidden symmetry of the dispersive balanced phases and comparison with the QHS model 53

4 Bulk-boundary correspondence of imbalanced topological Euler insulators 57
4.1 Introduction 57
4.2 Flat-band Euler insulators 59
4.2.1 Imbalanced Euler insulators 60
4.3 Theory 61
4.4 Conclusions 64

II Topological effects in twisted multilayer graphene 67

5 Re-entrant magic-angle phenomena in twisted bilayer graphene 69
5.1 Introduction 69
5.2 Approach 72
5.3 Re-entrant magic angle spectra at integer magnetic flux 72
5.4 Magnetic spectrum distinct from Landau levels 73
5.5 Emergent particle-hole symmetry 74
5.6 Non-trivial quantum geometric properties 75
5.7 Quantum-geometric transport 76
5.8 Conclusions 77

6 Unconventional Flat Chern Bands and 2e Charges in Skyrmionic Moiré Superlattices 79
6.1 Introduction 79
6.2 Underlying skyrmion lattice 81
6.3 Band structure and unconventional Chern flat bands 82
6.4 Skyrmion-induced band topology and the phase diagram 84
6.5 Hofstadter spectra 86
6.6 Hall conductance sequences 87
6.7 Conclusion 88

7 Landau Levels as a Probe for Band Topology in Graphene Moiré Superlattices 89

7.1 Introduction 89
7.2 Distinct configurations of TDBG 90
7.3 Hofstadter's butterfly of TDBG and Wannier diagrams 91

III Quantum transport in graphene-based nanostructures 97

8 Electronic transport in graphene with out-of-plane disorder 99
8.1 Introduction 99
8.2 Methodology 101
8.3 Electronic transport across commensurate wrinkles 102
8.4 Conductance oscillations in the atomic chain model 104
8.5 Transport across incommensurate wrinkles 107
8.6 Transport across graphene folds 108
8.7 Tight-binding results for the transmission 109
8.8 Discussion 110

9 Concluding remarks 113
9.1 Overview 113
9.2 Outlook 114

Bibliography 124

Curriculum Vitae 125

1 Introduction

Solids have been characterized as conductors and insulators regarding the ability to conduct electrical currents. Long after the empirical classification of materials, the development of quantum mechanics revealed the underlying nature of conductivity: the band theory has worked out well the correspondence between electronic band structures and conductivity. According to the location of the Fermi surface in electronic bands, insulators are the solids where the Fermi level lies within the band gap, while in conductors the Fermi level crosses electronic bands. Band theory, which has its roots in the quantum theory of electrons, has demonstrated its effectiveness in tackling a wide range of problems.

However, it was realized that the quantum theory of electrons should not only contain the energy spectrum of electrons. The ensemble of eigenstates, on the other hand, constitutes the other side of quantum mechanics. More intriguingly, the quantum eigenstates are meant to be complex, which introduces the phase degree of freedom. A well-known scenario where the eigenstates play a dominant role is when a two-dimensional (2D) electron gas is placed in a magnetic field. The magnetic field involves in the phase of electronic states. By inserting a nontrivial overall phase, the quantized Hall effect emerges. Such robust and quantized conductance has inspired the study of the underlying geometry of electronic states. Thanks to the theory of topology, it is possible to characterize the overall structure of eigenstates over the Brillouin zone (BZ). Since the advancement in the quantum Hall effect (QHE) (von Klitzing *et al.*, 1980, von Klitzing, 1986, Hatsugai, 1993), the topological aspect of electronic states has been recognized in condensed matter physics (Thouless *et al.*, 1982, Kane and Mele, 2005a). Typically, the family of topological insulators is expected to exhibit different properties from the usual insulators due to the topology of occupied bands. The research on topological insulators shows that band geometry has its manifestation in various physical properties. For example, exotic behaviours of Chern insulators and quantum spin Hall (QSH) insulators (Kane and Mele, 2005a,b, Bernevig *et al.*, 2006, Bernevig and Zhang, 2006) shed light on the new approaches to engineering electrons in solids.

Symmetries play a crucial role in the topology of bands. The milestone work of tenfold classification demonstrated the stable topological phases in terms of global symmetries (Schnyder *et al.*, 2008, Kitaev, 2009, Chiu *et al.*, 2016). The discussion of topology and symmetries expands to crystalline symmetries (Fu and Kane, 2007, Turner *et al.*, 2012, Chiu and Schnyder, 2014, Chiu *et al.*, 2013, Fu, 2011, Fang *et al.*, 2012, Slager *et al.*, 2013, Shiozaki and Sato, 2014, Alexandradinata *et al.*, 2016, Cornfeld and Chapman, 2019). Further efforts were made to combine the geometrical characteristics with crystalline symmetries. Fully considering the crystalline symmetries, there arises the systematic classification of band topology in terms of irreducible representation combinatorics (Kruthoff *et al.*, 2017), symmetry-based indicators (Po *et al.*, 2017, Khalaf *et al.*, 2018), elementary band representation (EBR) (Bradlyn *et al.*, 2019, 2017), and real-space topological crystals (Song *et al.*, 2019a). With such theories based on Elementary Band Representation (EBR), it becomes possible to tabulate the topological properties of almost all known crystals. The theory of EBR has revealed the essential relationship between topology and the localization of Wannier orbitals, by systematically demonstrating the topological classes in all space groups. With the progress in topological classification, the discrepancy between stable classification and EBR unveils the fragile topology of bands (Song *et al.*, 2020a, Po *et al.*, 2018a, Song *et al.*, 2020b, Bouhon *et al.*, 2019). Such fragile phases are sensitive to the number of considered bands, which is different from the previous stable phases. Generally, the fragile topological bands could be trivialized by adding extra trivial bands, which cannot affect the stable indicators.

The above discussion has been focusing on electrons without interactions. However, the Coulomb interaction between electrons also plays a crucial role in modulating electronic behavior. Furthermore, the topology of bands closely relates to the real-space distribution of electronic states (Marzari and Vanderbilt, 1997, Xu *et al.*, 2021), which in turn mediates the interactions between them (Xie *et al.*, 2020, Bernevig *et al.*, 2021, Huhtinen *et al.*, 2022). A well-known example where the correlation effects and geometry of eigenstates meet each other is the fractional quantum Hall effect (FQHE). In addition to fractional excitation, the topology of bands also involves the BCS interaction in the superconducting phase. Such an effect is considered to contribute to the superconductivity in twisted bilayer graphene (TBG).

In this Chapter, I will introduce the effects of topological numbers in 2D nanostructures based on graphene. The introduction contains examples of topological phases in materials and a review of the progress in graphene-based materials specifically. However, it is not intended to provide detailed techniques, which will be given in the chapter that follows.

1.1 Topology of bands

As indicated by its name, topological band theory aims to describe bands by their topological properties. Mathematically, band structures are complex vector bundles over n-dimensional torus (the Brillouin zone), of which the topological characterization gives the band topology. Physically, the problem is about whether different sets of subbands can be adiabatically deformed to each other. The term “topological bands” indicates that the electronic states are distinct from those formed by maximally localized Wannier orbitals, or “trivial bands”. Fig.

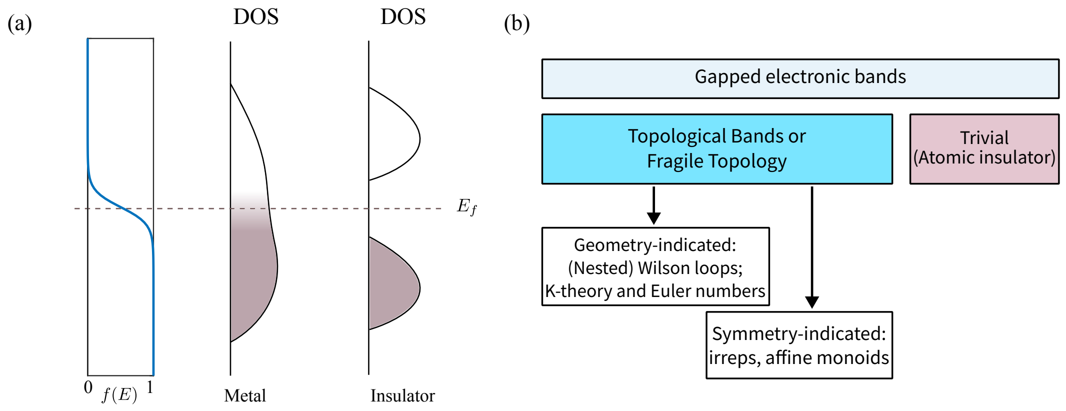
(a)
DOS
DOS
(b)
E_f
0
$f(E)$
1
Metal
Insulator
Gapped electronic bands
Topological Bands or Fragile Topology
Trivial (Atomic insulator)
Geometry-indicated: (Nested) Wilson loops; K-theory and Euler numbers
Symmetry-indicated: irreps, affine monoids

Figure 1.1 – (a) Fermi distribution and typical electronic density of states of metals and insulators. In metals, the Fermi level resides within an energy band, while in insulators the Fermi level is in a band gap. (b) A diagram of topological classification in gapped electronic bands. In contrast to trivial or atomic insulators, topological bands indicate that the bands cannot be projected into localized basis sets. The topology of the bands is characterized either by the geometry of the eigenstates or by the irreps of the symmetry groups. (This map is adapted from the work of Song *et al* (Song *et al.*, 2020a)).

1.1(b) shows a diagrammatic map for the classification of insulators. The trivial or atomic insulators indicate the case that the bands are formed by localized orbitals. Topological insulators, on the other hand, cannot be represented as a combination of maximally localized orbitals.

In this Section, I briefly cover the topological classification of bands, with an emphasis on Chern numbers and Euler numbers.

1.1.1 From quantized Hall effect to Chern numbers

The well-known quantum Hall effect has inspired the study on topological nature of bands. Such a quantum version of the Hall effect was first reported by von Klitzing *et al* (von Klitzing *et al.*, 1980, von Klitzing, 1984) with the measurement of quantized Hall resistance. In experiments, the Hall conductance of the sample shows quantization steps, which correspond to the Landau levels of 2D electronic gas. The theory was developed by Laughlin (Laughlin, 1981), who explained the relation of quantized conductance and gauge invariance.

After that, Thouless, Kohmoto, Nightingale and Nijs (TKNN) conducted the work of quantum Hall conductance in the presence of periodic potentials (Thouless *et al.*, 1982). Their result points out explicitly the dependence of Hall conductance on the index of Landau levels by the Kubo-Greenwood formula. Since the potential forms a periodic lattice, the Brillouin zone is in turn a 2D torus. The characterization number of a complex bundles over the 2D torus is given by the Chern number. It can be calculated by integrating the Berry curvature over the BZ:

$$C_m = -\frac{1}{2\pi}\int_{BZ} \Omega_m(\mathbf{k})d\mathbf{k} = -\frac{1}{2\pi}\int_{BZ} d\mathbf{k}[\langle\partial_{k_x}u|\partial_{k_y}u\rangle - \langle\partial_{k_y}u|\partial_{k_x}u\rangle], \tag{1.1}$$

which is indeed in the form of quantum Hall conductance as the correlation function of currents $\hat{j}_x$ and $\hat{j}_y$: $\sigma_H = \langle\hat{j}_x\hat{j}_y - \hat{j}_y\hat{j}_x\rangle$. Therefore, the quantization of Hall conductance is not a coincidence, but rooted in the topological nature of the bands.

The paper (Thouless *et al.*, 1982) paves the way towards topological properties of condensed matter physics, giving an observable that is related to a topological number which is called the TKNN number or Chern number. It was then discovered the invariant is closely related to the Berry phase of the Bloch functions. As reported by Halperin and TKNN (Hatsugai, 1993, Thouless *et al.*, 1982), the Hall conductance of the edge states is only determined by the TKNN number.

Since it is topological, the quantization of Hall conductance is robust against disorder, which ensures the precise measurement of the Hall conductance. The quantized Hall conductance then plays an important role in the newest definition of the SI unit systems for it provides an approach to measure some physical constants such as the charge of an electron.

1.1.2 Euler numbers

In the special cases where the system possess $\mathscr{P}\mathscr{T}$ or $C_2\mathscr{T}$ symmetries[1], there exists a global gauge where the eigenstates are real vectors. The Hamiltonian $H(\mathbf{k})$ is in turn real-symmetric:

$$C_2\mathscr{T}H(\mathbf{k}) = C_2H^*(-\mathbf{k}) = H^*(\mathbf{k}). \tag{1.2}$$

Computing the Berry curvature on such a ensemble of real eigenstates returns only null results, which further gives exactly zero Chern number in such systems. However, the bands could still possess nontrivial topology indicated by the Euler numbers. In contrast to the Chern number which depicts the topology of $U(N)$ bundles, the Euler numbers are defined on $SO(N)$ bundles and thus describes the topology of real eigenstates. The Euler number can also be expressed as an integration of differential forms:

$$E_\alpha = \frac{1}{2\pi}\int d\mathbf{k}\mathrm{Eu}_\alpha, \tag{1.3}$$

in which the Euler curvature Eu_α is defined on even-dimensional real vector bundle. Such a topological number provides geometry-indicated fragile topological phases: the classification falls into $\mathbb{Z}$-indicator in 2-band case, while it degenerates to $\mathbb{Z}_2$ if the number of bands is larger than 2. Such fragility makes it possible to construct “imbalanced” Euler phases in (2+2) bands. The Bloch condition imposes the total 4 bands to be topologically trivial, $E_4 = 0$. Since the

---

[1] $\mathscr{P}$, $\mathscr{T}$ indicate the parity and time-reversal symmetries, while C_n cyclic group represents the rotational symmetry.

4-band space falls into $\mathbb{Z}_2$ classification, $E_4 = 0$ only implies $E_+ + E_- = 0 \mod 2$.

It is also worth noticing that the Euler form in 2-band case duals to the Berry curvature of a single bands. Denoting the bands as $[u_1(k), u_2(k)]$, and a Chern basis is defined by a rotation:

$$\begin{aligned} v_+ &= (u_1 + iu_2)/\sqrt{2} \\ v_- &= (u_1 - iu_2)/\sqrt{2} \end{aligned} \tag{1.4}$$

it follows that the Berry curvature $F(v)$ is connected to the Euler characteristics by $F(v) = \pm \mathrm{Eu}(u)$.

1.1.3 Role of symmetries: tenfold classification and EBR

The Chern number is related to the localization of Wannier orbitals of certain subbands (Marzari and Vanderbilt, 1997). Following the ideas of Wannier obstruction, a systematic approach is then derived to tabulate topology with the crystal symmetries. Such methods are called elementary band representations (EBR). Since the main body of the thesis is not strongly relevant to EBR, here I only briefly cover the EBR with its basic ideas.

After the first prediction of 2D and 3D topological insulators (Bernevig and Zhang, 2006, Zhang *et al.*, 2009), various first-principle studies has been carried out to find candidates of topological materials. Besides the quickly increasing library of 2D and 3D topological materials, the classification theory of topological materials was also established. Kitaev has shown the topological phase in dimension $d = 1$-3 considering time-reversal (TR), chiral (C) and particle-hole (PH) symmetries. The work resulted to the tenfold classification of topology, which is based on Clifford algebra and the K-theory and thus applicable to arbitrary number of bands: adding trivial occupied bands does not change the topology.

In addition to the symmetries discussed in the tenfold classification, there are many other kinds of symmetries in crystals which are spatial symmetries. The work of (Fu and Kane, 2007) gives an approach to determine the topological invariant with wave functions on the high-symmetry points. Such method then inspired the study of topological phases protected by other symmetries (Fang *et al.*, 2012). Further works of the symmetry indicators of topology extend to general symmetry groups, making it possible to investigate the topology protected by all 230 space groups systematically. The idea is based on the distinction from atomic insulators: if the system is inequivalent to any atomic insulator, it is classified to be topological. This can be done with surprisingly simple mathematics. To investigate the symmetry, the irreducible representations (irreps) of the little groups on each high-symmetry point in the Brillouin zone are checked. The symmetry of the band structure is indexed by the “symmetry vector” composed of the multiplicity of irreps:

$$B = \{m^i_{K_1}; m^i_{K_2}; ...m^i_{K_n}\}$$

where $m^i_{K_j}$ denotes the multiplicity of irrep i of the little group at the jth Wyckoff point K_j. Due to the linearity of the representations, the topology of the bands can be determined by decomposing the symmetry vector B into a sum of vectors of atomic insulators:

$$B = \sum a_i B_i^{AI}$$

Based on the coefficients a_i in such decomposition, the set of occupied bands is classified into several distinct topological classes, and for each topological class, the topological index can be extracted from the symmetries (such as $\mathbb{Z}$ or $\mathbb{Z}_2$). If all a_i are positive integers, which means the bands are Wannierizable to localized Wannier functions, the system is topologically trivial. Otherwise, if some of the coefficients in a_i are rational fractions, the system is topologically nontrivial and may show nontrivial boundary states (Benalcazar *et al.*, 2019, 2017a). The distinction between these two cases is consistent with K-theory in the sense that the difference between integer and fractional decomposition is stable.

The group-theoretical classification is powerful in the computational search for topological materials, leading to an exhaustive study of the topology in over 40,000 materials (Bradlyn *et al.*, 2017, Autès *et al.*, 2019). Meanwhile, it also offers a new perspective to examine the topological classes. When carefully looking into the group-theoretical classification, a subtle zone shows up: if all coefficients in a_i are integers but some are negative, it also indicates a Wannier obstruction that is not stable. Such a kind of Wannier obstruction is removable by simply adding trivial occupied bands; thus, it is called the “fragile” topological phase. The fragile topology is not discussed in the K-theory approach since it is trivial in the many-band limit. However, in some real systems, the fragile phase can occur and lead to some new phenomena. For example, synthetic materials engineered with fragile topology exhibit in-gap states in twisted boundary conditions (Song *et al.*, 2020b), which provides an analogy of the bulk-boundary correspondence of Chern insulators.

The EBR theory based on irreps has explained the crystalline fragile topology from the algebraic perspectives. Meanwhile, the Berry-phase indicated index of crystalline fragile topology is still to be developed. Recently, some works have developed nested Wilson loops under crystal symmetries (Bouhon *et al.*, 2019), while a complete theory is still on its way.

1.2 Manifestation of topology in materials

Recognizing distinct topological classes of bands, there follows the question about their effect on physical properties of materials. The physical observables determined by topological numbers bridge the microscopic band structures with macroscopic phenomena. Furthermore, finding topological effects in materials is crucial for diagnosing different topological phases. The intrinsic robustness of the topological numbers could protect certain physical effects. Engineering such topological states promises to open another dimension of creating emergent electronic states in nanostructures. In the following paragraphs, I present the manifestation of topology and Berry curvature in materials. The discussion focuses on low-dimensional cases with $d = 1, 2$, while there are also generalizations in 3D (Benalcazar *et al.*, 2017a, Qi *et al.*, 2008).

In its simplest form, topology of bands describes the phase of wavefunction over the Brillouin zone. I start with the phase of wave functions and its relation to the real-space position of the charge center:

$$\bar{\mathbf{r}} = -i \ln\langle u(\mathbf{k}) | u(\mathbf{k} + 2\pi)\rangle, \tag{1.5}$$

where $u(\mathbf{k})$ denotes the periodic parts of selected eigenstates at momentum $\mathbf{k}$. Such a relation follows naturally from the periodicity of lattice. $\bar{\mathbf{r}}$ is sometimes called the Wannier center of the bands. The phase accumulated from k to $k + 2\pi$ can be written as an integration:

$$\langle u(\mathbf{k}) | u(\mathbf{k} + 2\pi)\rangle = \int d\mathbf{k} - i\langle u(\mathbf{k}) | \partial_{\mathbf{k}} | u(\mathbf{k})\rangle = \int A d\mathbf{k}, \tag{1.6}$$

where $A = \langle u | \partial_{\mathbf{k}} | u\rangle$ is a gauge field on the BZ known as the Berry connection. In its one-dimensional manifestation, such results of Wannier function leads to a modern theory of charge polarization in topological insulators (Coh and Vanderbilt, 2009, Resta, 2010). Note that the electronic contribution to polarization is traced by the Wannier centers:

$$\mathbf{P} = -\frac{2}{V_c} \sum_{i=1}^{N_{occ}} \mathbf{r}_i = -\frac{2i}{(2\pi)^3} \int d\mathbf{k} \langle u(\mathbf{k}) | \nabla_{\mathbf{k}} | u(\mathbf{k})\rangle. \tag{1.7}$$

The definition of 2D topological numbers suggests nontrivial response to gauge fields (Qi *et al.*, 2008, Resta, 2010, Chang and Niu, 2008, 1996, Gao *et al.*, 2015, Thonhauser *et al.*, 2005), as natural generalizations to the quantized Hall effect (von Klitzing, 1986, Thouless *et al.*, 1982). There are two effects rising from the topology of the bands: the quantum Hall (QH) response and orbital magnetization. I address such electromagnetic effects with a 2D electron gas in a weak periodic potential: in this scenario, the physics are well-captured by Landau levels of free electron gas, while the periodic potential enables topological arguments on a compact manifold. The QH response is defined as (Qi *et al.*, 2008):

$$\begin{aligned} \sigma_H &= \langle \hat{j}_x \hat{j}_y - \hat{j}_y \hat{j}_x \rangle \\ &= \frac{e^2}{h} \frac{1}{2\pi} \int dk_x \int dk_y F_{xy}, \end{aligned} \tag{1.8}$$

which is proportional to the Chern number. The QH response also induces response of the charge density ρ. Introducing a magnetic field B adiabatically versus time t, it follows that:

$$\begin{aligned} \frac{\partial \rho}{\partial t} &= -\nabla \cdot j = \sigma_H \frac{\partial B}{\partial t} \\ \rho(B) - \rho_0 &= \sigma_H B. \end{aligned} \tag{1.9}$$

This relationship is alternatively expressed by the Streda formula (Streda, 1982a,b) in a crystal

(Dana *et al.*, 1985a):

$$\sigma_H \frac{e^2}{h} = ec\frac{\partial N(E)}{\partial B}, \tag{1.10}$$

which relates the Hall conductance to the electron filling $N(E)$. Therefore, the band topology implies the quantized response to external magnetic fields.

In addition to the charge density, the energy of topological bands is also pumped by the magnetic field. Such a response is also called the orbital magnetization (Resta, 2010, Thonhauser *et al.*, 2005, Shi *et al.*, 2007, Thonhauser, 2011, Wu *et al.*, 2021, Sundaram and Niu, 1999), defined as the linear-order response to magnetic field $m_n(k)$ appearing in the perturbative response of energy bands:

$$\varepsilon_{n,\sigma}(\mathbf{k}, B) = \varepsilon_n(\mathbf{k}) + \mu_B g\sigma B + m_n(\mathbf{k})B, \tag{1.11}$$

where the term $\mu_B g\sigma B$ is the Zeeman effects from spins. The orbital magnetic moment is:

$$m_n(\mathbf{k}) = -\mu_B \frac{2m_e}{\hbar^2} \mathrm{Im}\left\{ \sum_{m\neq n} \frac{\langle n|\partial_{k_x} H|m\rangle\langle m|\partial_{k_y} H|n\rangle}{\varepsilon_n - \varepsilon_m} \right\}, \tag{1.12}$$

of which the form is closely related to the spectral representation of Berry curvature. Such response to magnetic field is generally not quantized. In the special limit of Landau levels, as the bands are dispersionless and effective mass m_e remains constant, the m_n of each Landau level is constant within small magnetic fields.

The topology of bands also relates closely to the spatial distribution of Wannier functions[2], (Marzari and Vanderbilt, 1997, Marzari *et al.*, 2012) which is concluded as Wannier obstruction to subbands (Marzari and Vanderbilt, 1997, Zhang *et al.*, 2020a). The term Wannier obstruction describes the effect that a set of topological subbands is prevented from forming localized Wannier orbitals. It can be seen from the spread functional of the bands:

$$\Omega = \sum_i [\langle r^2\rangle_i - \langle r\rangle_i^2]. \tag{1.13}$$

Ω contains two parts of contributions:

$$\Omega = \Omega_I + \tilde{\Omega}, \tag{1.14}$$

in which two positive-definite terms Ω_I and $\tilde{\Omega}$ represent the gauge-invariant part and gauge-dependent part of the spread functional. Minimizing Ω therefore indicates finding a smooth gauge that gives minimal $\tilde{\Omega}$. Indeed, both Ω_I and $\tilde{\Omega}$ relate closely to the topology of bands (Marzari and Vanderbilt, 1997, Marzari *et al.*, 2012). The minimum value of $\tilde{\Omega}$ is given by the Berry curvature, which is vanishing only if the bands are topologically trivial (Marzari and

---

[2] Wannier functions can be chosen differently up to a gauge transformation. For the instance, it's sufficient to take it as a basis of certain bands. An introduction on Wannier functions will be given in Chapter. 2

Vanderbilt, 1997). Moreover, the gauge-invariant component Ω_I equals to the integral of the quantum geometrical tensor $g(\mathbf{k})$:

$$\Omega_I = \frac{V}{(2\pi)^N} \int d\mathbf{k} \operatorname{Tr} g(\mathbf{k}), \tag{1.15}$$

the term $g(\mathbf{k})$ serves as a metric tensor on the Brillouin zone:

$$g(\mathbf{k}) = \sum_n \langle \partial u(\mathbf{k})|(1-|u(\mathbf{k})\rangle\langle u(\mathbf{k})|)|\partial u(\mathbf{k})\rangle. \tag{1.16}$$

Consequently, there is an obstruction towards building maximally localized Wannier orbitals with topological bands. The Wannier obstruction simutaneously invloves singularities in polarization if the Chern number is nonzero (Benalcazar *et al.*, 2017a,b).

The theory of Wannier obstruction further implies the signatures of edge states or corner states (Benalcazar *et al.*, 2017a,b, Song *et al.*, 2020c). As its simplest example, the Wannier charge centers in Chern insulators move through unit cells upon a momentum pumping. Such pumping leads to edge modes of Chern insulators, which can be seen by inserting a cut in the system. A generalization of the argument naturally gives the predictions to corner states, hinge states and defect modes (Benalcazar *et al.*, 2017b). In analogy to the formulas for polarization, the higher-moment operators are defined for quadrupole (q_{ij}) and octupole (o_{ijk}) moments as well (Benalcazar *et al.*, 2017a):

$$p_i = \int d^3\mathbf{r} \rho(\mathbf{r}) r_i, \tag{1.17}$$

$$q_{ij} = \int d^3\mathbf{r} \rho(\mathbf{r}) r_i r_j, \tag{1.18}$$

$$o_{ijk} = \int d^3\mathbf{r} \rho(\mathbf{r}) r_i r_j r_k. \tag{1.19}$$

Under certain symmetries, the electrical multipole moment can be quantized, giving localized corner modes in the gap carrying fractional charge (Benalcazar *et al.*, 2017b). These localized electronic modes has an effect on catalysis as well (Li *et al.*, 2022).

Wannier functions of the bands mediates the interactions between electrons. In real space, the effects come from the distribution of the wave functions:

$$H_{int}(\phi_i, \phi_j) = \langle \phi_i | \frac{e^2/2}{\mathbf{r}_{ij}} | \phi_j \rangle. \tag{1.20}$$

An example is the topological nematic states (Barkeshli and Qi, 2012), built from the hybrid Wannier functions. In the reciprocal space, the formula of Coulomb interaction closely relates to the overlap of momentum-eigenstates:

$$\lambda(\mathbf{k}, \mathbf{q}) = \langle U(\mathbf{k}+\mathbf{q})|U(\mathbf{k})\rangle, \tag{1.21}$$

sometimes also called the *form factors*. The expression is expected to behave differently in topological bands as compared to trivial bands. Such an effect was recently revealed to contribute to flat-band superconductivity (Xie *et al.*, 2020, Peotta and Törmä, 2015), giving a superfluid weight bounded by the geometry of flat bands:

$$\mathrm{Tr}\, D_s = \frac{8e^2\Delta}{\hbar^2}\sqrt{\nu(1-\nu)}\int \frac{d^2k}{4\pi^2}\mathrm{Tr}\, g. \tag{1.22}$$

The topological part may contribute significantly to the moiré superconductivity (Xie *et al.*, 2020, Cao *et al.*, 2018a).

Concerning the intriguing issue of flat-band superconductivity, the interplay between topology and (pseudo)spin textures is worth mentioning (Wilczek and Zee, 1983, Sondhi *et al.*, 1993). Briefly, in a O (3) nonlinear-σ model (NLσM) involving (pseudo) spins, the charge carried by a skyrmion is determined by:

$$\rho = CW, \tag{1.23}$$

where C is the Chern number of the bands and W is the skyrmion winding number.

1.3 Graphene and twisted bilayer graphene

The isolation of atomically thin graphene monolayer (Novoselov *et al.*, 2004) has greatly inspired the study of two-dimensional (2D) materials (Novoselov *et al.*, 2005). The family of 2D materials provides a large variety of electronic structures, including the massless Dirac fermions in graphene and the quantum spin Hall (QSH) phase in 1T'-MoS_2 (Qian *et al.*, 2014). Such electronic properties and topology of 2D materials are of interest in both condensed matter physics and microelectronics (Jang *et al.*, 2016, Ju *et al.*, 2015, Han *et al.*, 2018, Gomes *et al.*, 2012). The progress on 2D materials also drives the study of 2D nanostructures and metamaterials (Cao *et al.*, 2018a, Wang *et al.*, 2016, Moon and Koshino, 2014, Cao *et al.*, 2018b), aiming at the manipulation of electronic states in low-dimensional systems.

As the first discovered 2D material, graphene plays an important role in such 2D nanostructures (Po *et al.*, 2018b, Yazyev, 2013, Talirz *et al.*, 2016). Intrinsic graphene provides a good example of a system hosting massless fermions on a 2D honeycomb lattice (Gomes *et al.*, 2012, Son *et al.*, 2011, Mariani *et al.*, 2012) while by engineering on graphene, it is possible to tune the band structure such as creating a gap (Cao *et al.*, 2017, Haldane, 1988) or squeezing the band width (Bistritzer and MacDonald, 2011a). On the basis of graphene, many nanostructures and metamaterials are found with nontrivial band topology (Po *et al.*, 2018b, Luo, 2019, Liu *et al.*, 2020, Song *et al.*, 2019b) and correlated electronic states (Cao *et al.*, 2018a,b, Du *et al.*, 2009, Dean *et al.*, 2013). The study on these materials, including computational simulation and development of analytical models, will be helpful in understanding the origin of band topology (Po *et al.*, 2018b, 2019) and to design novel materials with intended electronic properties.

A family of graphene-based material, twisted multilayer graphene, has recently attracted

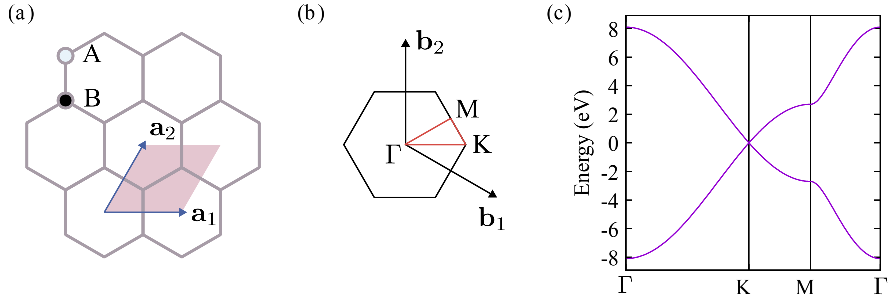

Figure 1.2 – Graphene lattice and a plot of its band structure. (a) The structure of graphene lattice. Each unit cell contain two carbon atoms labelled A and B. (b) Reciprocal lattice vectors of graphene lattice and the Brillouin zone. High-symmetry paths of momentum are shown in red. (c) Nearest-neighbour tight-binding band structure of graphene along the k path.

massive attention due to their exotic electronic properties since the observation of superconductivity and correlated insulating behavior in magic-angle twisted bilayer graphene (TBG) (Cao *et al.*, 2018a,b). Such electronic properties are related to flat electronic bands near the Fermi energy, which is a consequence of the twisted stacking.

Besides the experimental work, many theoretical models have been proposed for the moiré flat bands (Po *et al.*, 2018b, Song *et al.*, 2019b, Bistritzer and MacDonald, 2011b, Lian *et al.*, 2018, Zhang *et al.*, 2019, Liu *et al.*, 2019a, Tarnopolsky *et al.*, 2019, Hejazi *et al.*, 2019). These models provide useful perspectives for understanding the magic angle TBG, while the theoretical explanation to the correlated behavior is still not complete due to the complexity of moiré superlattice. On the experimental side, a common and effective way to characterize such moiré superstructures is the transport measurements with an out-of-plane magnetic field (Dean *et al.*, 2013, Lian *et al.*, 2018, Schultz *et al.*, 1998). Thanks to the moiré-induced superperiodicity, for moiré superlattices it is possible to further probe the fractal Landau level or Hofstadter butterfly (Dean *et al.*, 2013, Wang *et al.*, 2012, Kim *et al.*, 2017) which is conjectured to be related with fragile topology (Lian *et al.*, 2018).

I present an introduction to the family of materials: graphene and twisted bilayer graphene. This section covers the electronic structures of the materials, the topological effects and magnetotransport properties.

1.3.1 Hamiltonian of graphene

Graphene consists of a honeycomb lattice of carbon atoms. As shown in Fig. 1.2(a), each unit cell contains two sublattices, referred to as A and B atoms. The lattice constant of graphene is usually taken to be $a = 2.46$ Å, corresponding to the C-C bond length of 1.42 Å. It is worth presenting, the widely-used tight-binding Hamiltonian involving p_z orbitals, and the $k \cdot p$ model of graphene. Considering only the nearest-neighbour coupling of the orbitals, the

Hamiltonian writes:

$$H = \sum_{\langle i,j \rangle} t c_i^\dagger c_j, \tag{1.24}$$

where $\langle i, j \rangle$ denotes the nearest-neighbour bonds. In momentum space, it is expressed as a 2×2 matrix:

$$H(k_x, k_y) = t \begin{pmatrix} 0 & 1 + e^{-ik_x} + e^{-ik_y} \\ 1 + e^{ik_x} + e^{ik_y} & 0 \end{pmatrix}. \tag{1.25}$$

A sketch of the Brillouin zone and the band structure of graphene along the k-path is presented in Fig. 1.2 (b-c). Such a Hamiltonian gives linear dispersion at the Fermi level, near the two high-symmetry points K/K' which are referred as Dirac points. The $k \cdot p$ approximation of the Hamiltonian near each Dirac point gives:

$$H_{kp}^{\pm} = \pm \hbar v_f (\sigma_x k_x \pm \sigma_y k_y), \tag{1.26}$$

in which the signs ± correspond to valley K and K' respectively.

1.3.2 Berry phase and topological effects of Dirac cones

The Dirac cones of graphene carry nonzero Berry phase, which makes the material interesting in terms of topology. Such effect is seen by the winding of eigenstates along a loop enclosing the Dirac point. Taking the $k \cdot p$ Hamiltonian near one of the valleys: $H = \hbar v_f (\sigma_x k_x + \sigma_y k_y)$ and writing it in polar coordinates, the Hamiltonian becomes:

$$H(\phi, r) = \hbar v_f r \begin{pmatrix} 0 & e^{i\phi} \\ e^{-i\phi} & 0 \end{pmatrix}. \tag{1.27}$$

The eigenstates are then $\psi_\pm = (e^{i\phi/2}, \pm e^{-i\phi/2})$. While ϕ winds around the Dirac points, i.e. ϕ goes from 0 to 2π, each of $\psi_\pm$ gains a phase factor of π. Such a nonzero Berry phase makes graphene a promising precursor for 2D topological phases. By properly gapping the Dirac cones, it is possible to build the Haldane model with Chern numbers $C = \pm 1$.

Note that the two valleys are in opposite phases which imply opposite chiralities, such an effect leads to a signature of the Berry phase in inter-valley scatterings (Dutreix *et al.*, 2019).

1.3.3 Twisted multilayer graphene

The van der Walls (vdW) heterostructures of 2D materials are of special interest since they provide another dimension of manipulating the structure of the matter. Typically, the scenario of twisted stacking has attracted much attention: twisted multilayers of 2D materials enables tuning the periodicity of the lattice by the interlayer twist angle.

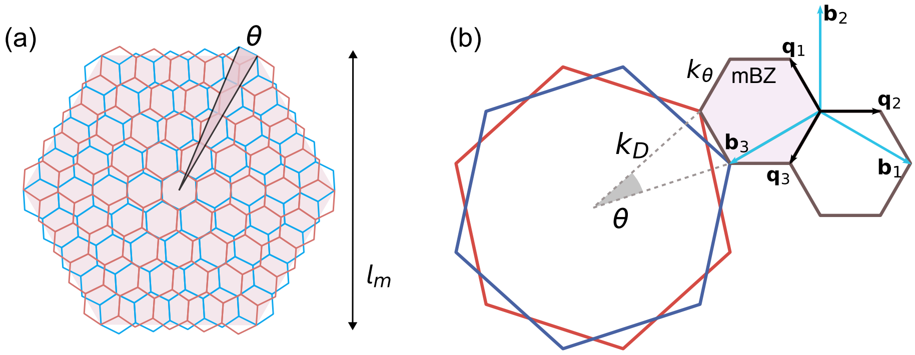

Figure 1.3 – (a) An example structure of twisted bilayer graphene. The twist angle θ determines the moiré lattice constant l_m. (b) Effect of interlayer twist in the reciprocal space and the moiré Brillouin zone. The reciprocal vector is given by $\mathbf{b} = \sqrt{3}\mathbf{k}_\theta$, where the distance between moiré Dirac points is $\mathbf{k}_\theta = 2\sin(\theta/2)\mathbf{k}_D$, where $\mathbf{k}_D$ is the graphene Dirac-point momentum.

Table 1.1 – Typical indices and their corresponding twist angles θ.

n	1	5	20	30	31
θ (deg)	21.79	6.01	1.61	1.08	1.05

As shown in Fig. 1.3, bilayer graphene with an interlayer twist features the moiré superperiodicity. The relation between the twist angle and the superlattice length is derived by the commensuration conditions. I use the commonly-accepted notation for twisted bilayer graphene, where the commensurate twist angles θ are defined on the lattice vectors $(m, n) = m\mathbf{a}_1 + n\mathbf{a}_2$ (see Fig. 1.3), where the interlayer twist is considered as a rotation operator $\hat{R}(m, n) = (n, m)$. The twist angle is given by

$$\theta_{nm} = \arg\left[\frac{m + n/2 + \sqrt{3}ni/2}{n + m/2 + \sqrt{3}mi/2}\right]. \tag{1.28}$$

The series $m = n + 1$ is predominantly examined as “minimal series” of twists. I present the table with a few typical indices and the corresponding twist angles between the layers. Within the series, θ decreases as n increases. The lattice constant l_m of the moiré supercell is determined by (m, n) as: $l_m = a\sqrt{m^2 + n^2 + mn}$, where $a = 2.46$ Å is the graphene lattice constant.

While the lattice constant is enlarged in the moiré supercells, the reciprocal lattice becomes smaller than that of graphene. Fig. 1.3(b) shows the relation between moiré Brillouin zone and the graphene BZ.

The local interlayer stacking is varying between AA and AB across the moiré cell. Consequently, the interlayer coupling between orbitals is also inhomogeneous.

The Hamiltonian of twisted bilayer graphene is expressed on the basis of $k \cdot p$ Hamiltonian of

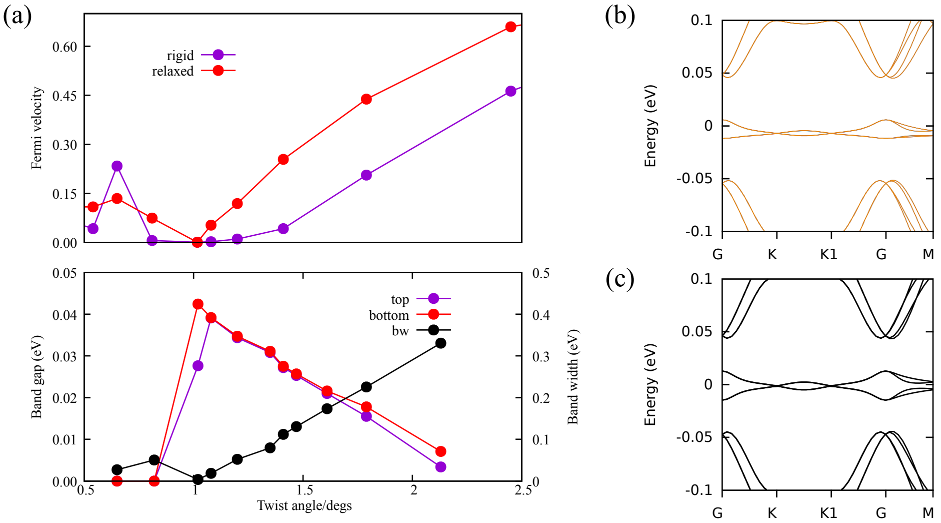

Figure 1.4 – (a) The evolution of Fermi velocity and bandwidth over twist angles, obtained from TB calculations. Vanishing Fermi velocity and bandwidths are present near $\theta = 1.1°$. The flat bands in TBG at magic angle $\theta = 1.08°$, from (b) tight-binding models and (c) $k \cdot p$ models.

graphene. In the vicinity of the K valley, the $k \cdot p$ Hamiltonian writes (Liu *et al.*, 2019a):

$$H^{+}(\mathbf{k}) = \begin{pmatrix} \hbar v_f(\mathbf{k} - K_1) \cdot \sigma & U \\ U^{\dagger} & \hbar v_f(\mathbf{k} - K_2) \cdot \sigma \end{pmatrix}, \tag{1.29}$$

in which $\hbar v_f(\mathbf{k} - K_i) \cdot \sigma$ are the Hamiltonian of each layer, K_i indicates the K points of the graphene layers. The U blocks contain interlayer coupling and encode the spatial dependence:

$$U = U_0 e^{i\Delta_K \cdot \mathbf{r}} = \begin{pmatrix} u_0 g(\mathbf{r}) & u_1 g(\mathbf{r} - \mathbf{r}_{AB}) \\ u_1 g(\mathbf{r} + \mathbf{r}_{AB}) & u_0 g(\mathbf{r}) \end{pmatrix} e^{i\Delta_K \cdot \mathbf{r}}, \tag{1.30}$$

where the phase factor $g(\mathbf{r}) = \sum_{j=1}^{3} e^{i\mathbf{q}_j \cdot \mathbf{r}}$ provides the interlayer coupling. The equation can be solved in the plane-wave basis. As shown in Fig. 1.4, there is a range of twist angles where the Fermi velocity is compressed. Such flat bands are also verified by the atomistic TB calculations with Slater-Koster Hamiltonian (Slater and Koster, 1954, Gargiulo and Yazyev, 2018).

The flat bands appearing at the “magic angles” provide a platform where various aspects of physics meet together. General flat bands are expected to exhibit electronic correlation since the kinetic energy is suppressed. In the case of TBG, the flat bands near the Fermi level are also featuring nontrivial topology, carrying Euler number $E = 1$. Moreover, transport measurements has revealed the correlated insulating phases and superconductivity in twisted bilayer graphene (Cao *et al.*, 2018a,b). Therefore, the flat-band physics involves the correlation effects of topological electronic bands.

The progress on twisted bilayer graphene has inspired a series of further studies aiming at studying the superconductivity in twisted multilayer graphene systems. Similar to twisted

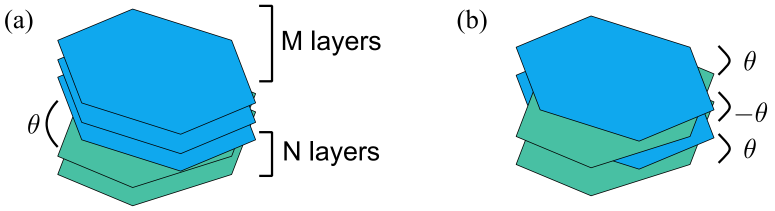

Figure 1.5 – Sketch of twisted multilayer systems. (a) Twisted $(M+N)$-layer graphene. (b) Alternating twisted multilayer graphene.

bilayer graphene, these systems also show flat bands near the Fermi level, as well as the unconventional superconductivity. Fig. 1.5 shows two classes of twisted multilayers, as generalizations of the TBG. The $(M+N)$ layers twisted graphene (Fig. 1.5a) has topological flat bands near the Fermi level. By controlling the stacking between M-layer graphene and N-layer graphene, the system can be engineered to carry arbitrary valley Chern numbers (Liu *et al.*, 2019b). The alternating twisted graphene features a composition of Dirac cones and flat bands. Both the magic angle and the superconducting transition temperature are changed in such multilayer scenario (Park *et al.*, 2022). In TBG and alternating twisted trilayer graphene, the critical temperature is around 3 K, while for 4-layer and 5-layer cases the temperature goes to 2.2 K. On the other hand, the "magic angle" increases as increasing the number of layers. In the limit of infinite layer alternating twisted graphene, the magic angle goes up to $\theta_M \approx 2.2°$.

1.4 Outline of the thesis

This thesis contains various aspects of topological effects in 2D materials. The research contains two levels of studies: theoretical models of topological systems and the related effects or physical observables in 2D materials. The outline of the following part will be:

- Chapter 2 presents the theory and methodology for studies of following chapters. It consists of the basic theory of band structure and topological band theory, as well as numerical methods for the calculations.
- Part I focuses on the theoretical studies of Euler insulators. As a unique class of fragile topological insulators, the properties of Euler insulators are still being explored. This part examines the Landau levels and edge states of Euler insulators, aiming to identify physical probes for such topological classes. The investigation into the Landau levels of Euler insulators reveals similarities with mirror-Chern insulators while also demonstrating the magnetization of Euler bands. This discovery is particularly intriguing when compared to the existing results for Chern insulators. In addition to the Landau levels, the edge states of Euler insulators are also investigated. We develop a theory of edge Hamiltonians for Euler insulators, which shows that the algebraic order of the edge

states is equal to the bulk Euler number. This study of edge theory provides observable properties for Euler insulators and further enriches the understanding of bulk-edge correspondence.

- Part II focuses on the study of twisted bilayer graphene. In recent years, the family of twisted multilayer materials has attracted significant attention due to the presence of unconventional correlated insulating states and superconductivity. Theoretical investigations on twisted multilayer graphene span several distinct levels. Using atomistic tight-binding models, we explore the electronic band properties of twisted bilayer graphene under strong magnetic fields, the interplay between band topology and magnetic skyrmions, and the Landau levels in twisted double bilayer graphene. These studies aim to deepen our understanding of the complex electronic behaviors observed in these materials and potentially uncover novel properties and phenomena.
- Part III contains the study of electronic transport in graphene with out-of-plane disorder. Using first-principles calculations, we discover the transmission across commensurate and incommensurate disorder. When wrinkles or folds match with the graphene lattice, a transmission oscillation is induced by backscattering. However, in the incommensurate case, the transmission shows vanishing backscattering. The contrast between these cases reveals the effect of lattice commensuration on the electronic transport in graphene with out-of-plane disorder..

2 Theory

This chapter delves into the theoretical foundations of the studies on two-dimensional solid-state materials. I begin with the fundamentals of the Schrödinger equation and then introduce the tight-binding (TB) approximation for electronic structure calculations. The theories presented in this chapter establish the formalism for a range of calculations based on TB models, providing the necessary background to understand the methods and techniques used in subsequent chapters. This comprehensive overview of the theoretical framework will serve as a solid basis for the exploration of various phenomena within the context of electronic properties of two-dimensional materials and nanostructures.

2.1 Schrödinger equation and Band theory

The motion of electrons follows the (time-independent) Schrödinger equation:

$$\hat{H}\psi = E\psi, \tag{2.1}$$

where in most cases the effects from nuclei is neglected taking the Born-Oppenheimer approximation (Combes *et al.*, 1981). Generally, the Hamiltonian $\hat{H}$ contains different terms including the electron kinetic energy T_e, the potential energy from nuclei V_n and the electron interactions V_{e-e}:

$$\hat{H} = T_e + V_n + V_{e-e} + ..., \tag{2.2}$$

and ψ is the many-body wavefunction. Solving the many-electron Schrödinger equation is typically difficult. To simplify the problem, the single-electron approximation is often employed by assuming that the electron-electron interaction term, V_{e-e}, is negligible. This approximation significantly reduces the computational complexity and makes the problem more tractable.

For crystals, it is considered that the system is spatially periodic, i.e. the Hamiltonian H and lattice translation $T_{\mathbf{r}}$ commute: $[\hat{H}, T_{\mathbf{r}}] = 0$ for lattice translations $\mathbf{r}$. The solutions of the single-electron Schrödinger equation has a general form called the Bloch functions:

$$\psi_n(\mathbf{k},\mathbf{r}) = e^{i\mathbf{k}\cdot\mathbf{r}} u_n(\mathbf{r}), \tag{2.3}$$

which are composed of a plane-wave function modulated by a function $u(\mathbf{r})$ with the same periodicity as the lattice.

As there is translational symmetry of the lattice, it is possible to construct the wavefunction with a set of orbitals residing in each unit cell, called the Wannier functions (WFs). The relation between these orbitals and the Bloch functions is:

$$\psi(\mathbf{k},\mathbf{r}) = \sum_{\mathbf{R}} e^{i\mathbf{k}\cdot\mathbf{R}} \phi(r-R), \tag{2.4}$$

where the function ϕ is defined for each unit cell, called the Wannier functions. Fig. 2.1(a) shows a comprehensive plot comparing the Bloch function and Wannier function.

Translational-invariant wave functions form the basis set of the Hamiltonian, and the energy levels become functions of the momentum **k**, which has a periodicity in reciprocal of the lattice constant. To illustrate this, I provide in Fig. 2.1(b) the band structures for one-dimensional systems with periodic potential $U(r)$. The Hamiltonian containing kinetic energy E_k and the periodic potential writes:

$$H = E_k + U(r), \tag{2.5}$$

where the potential $U(r+a) = U(r)$ has periodicity of a, the momentum thus exhibits a periodicity of $2\pi/a$. Different regimes emerge during the evolution from the limits of nearly-free electrons ($E_k \gg U$) to localized orbitals ($E_k \ll U$), while they other term is treated as a perturbation. Near $k = 0$, the nearly-free electron limit behaves asymptotically as $E \propto k^2$. By adding the on-site periodic potential, the full energy $E(k)$ develops into a series of energy bands. In the limit $E_k \ll U$, $E(k)$ appears as discrete energy levels that are barely dependent on k.

The band structure serves as the foundation for exploring the electronic properties of solids, including conductivity and the effective mass of electrons. In practice, calculating the band structure is an essential step in the study of quantum materials.

2.2 Tight-binding Hamiltonian for electrons in solids

An approach to model the electrons in solids is the tight-binding (TB) approximation, where the basis sets are taken as a discrete series of orbitals. The general formulation of TB Hamiltonians is:

$$H_{tb} = \sum_{i,j} t_{ij} c_i^\dagger c_j + \sum_i V_i c_i^\dagger c_i, \tag{2.6}$$

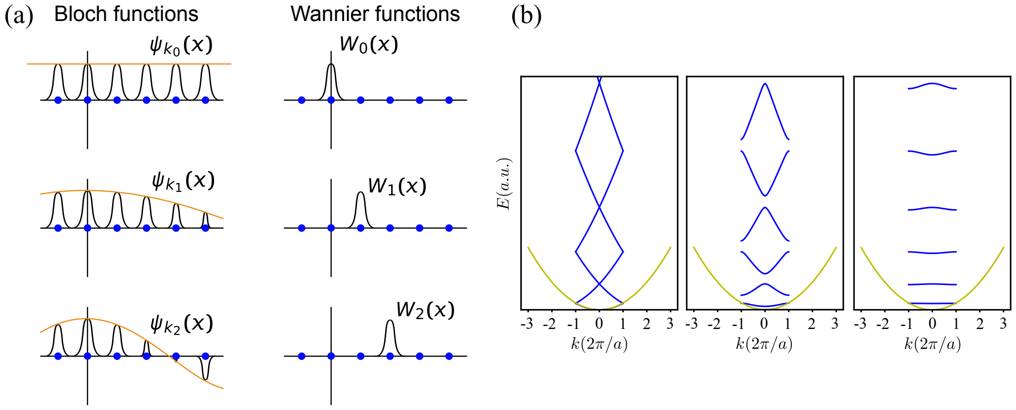

Figure 2.1 – (a) An illustrative plot of Bloch functions and Wannier functions (adapted from (Marzari *et al.*, 2012)). (b) Diagrammatic energy spectrum for a one-dimensional system on different levels of periodic potential U. The nearly-free-electron dispersion evolves into sets of bands in the presence of a periodic potential.

where the first term encompasses the kinetic energy of electrons through hopping integrals t_{ij}, while the second term includes the potential energy of the orbitals. The operators $c_i^\dagger, c_i$ represent creation and annihilation operators for localized-orbital states or Wannier functions. The TB Hamiltonian, given by Eq. 2.6, is related to the general Hamiltonian of electrons as follows:

$$\begin{aligned} t_{ij} &= \langle \psi_i | \hat{H} | \psi_j \rangle \\ V_i &= \langle \psi_i | \hat{H} | \psi_i \rangle \\ \psi_i &= c_i^\dagger |0\rangle. \end{aligned} \tag{2.7}$$

To close this subsection, I discuss the Peierls substitution which introduces magnetic fields in tight-binding models. In the presence of magnetic field $\mathbf{B} = \nabla \times \mathbf{A}$, the tight-binding hopping integrals are transformed to t'_{ij} by adding the integral of vector potential $\mathbf{A}$ into the phase factors:

$$\begin{aligned} t'_{ij} &= t_{ij} e^{i\theta} \\ \theta &= \int_{\mathbf{r}_i}^{\mathbf{r}_j} \mathbf{A} \cdot d\mathbf{r}. \end{aligned} \tag{2.8}$$

The phase factor explicitly alters the lattice's periodicity. Due to the magnetic flux, translation operators in a and b directions do not commute $T_a T_b = e^{i\phi} T_b T_a$ (Herzog-Arbeitman *et al.*, 2022). To restore translational invariance, the unit cell must be expanded to create a magnetic supercell satisfying $[T'_a, T'_b] = 0$. As an example, consider the Peierls substitution in a square lattice (Fig. 2.2(a)) in the Landau gauge $\mathbf{A} = [0, Bx, 0]$ with $\Phi = 2\pi\frac{p}{q}$. The magnetic unit cell is constructed with T_{qa} and T_b, ensuring the total flux $\Phi_m = 2p\pi$. The super-periodicity induced by the flux $\Phi = 2\pi p/q$ splits the spectrum into q subbands. As shown in Fig. 2.2(b), the energy

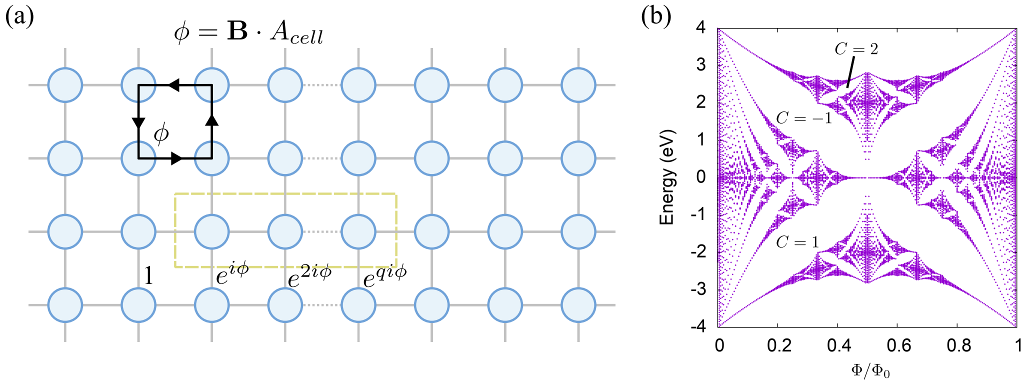

Figure 2.2 – (a) A sketch of the Peierls substitution in a square lattice. The flux per unit cell is proportional to the phase ϕ gained over a loop enclosing the area of the cell. The magnetic unit cell containing q unit cells is built for $\Phi = 2\pi p/q$. (b) The energy levels versus magnetic flux Φ in a square lattice, featuring a fractal pattern. Each gap in the fractal spectrum carries a topological Chern number, identified by the slope $\partial N/\partial B$.

levels form a fractal structure called the Hofstadter butterfly (Hofstadter, 1976). The gaps in the Hofstadter butterfly are marked with topological Chern numbers (Wannier, 1978).

2.3 The Slater-Koster model calculations

While the nearest-neighbour (NN) tight-binding model provides a quite faithful description of the electronic structure of flat monolayer graphene, the modelling of general graphene-based nanomaterials goes beyond the NN approximation. To account for both interlayer coupling and curvature effects in tight-binding calculations of graphene nanostructures, I utilize the Slater-Koster model (Slater and Koster, 1954, Zhu *et al.*, 2012). The p_z atomic orbitals of carbon atoms form the intralayer π bonds and the interlayer σ bonds, as shown in Fig. 2.3(a). The general form of the Hamiltonian including both contributions writes:

$$\hat{H} = \sum_{i,j} t^{\pi}_{ij} c^{\dagger}_i c_j + \sum_{i,j} t^{\sigma}_{ij} c^{\dagger}_i c_j.$$

Explicit expressions for the hoppings t^{π}_{ij} and t^{σ}_{ij} are dependent on the orientation of the two p_z orbitals on atom i, j (Zhu *et al.*, 2012)

$$t^{\pi}_{ij} = V^{\pi}_0 \exp\left(-\frac{r - a_0}{r_0}\right) |\sin\theta_i \sin\theta_j|, \tag{2.9}$$

$$t^{\sigma}_{ij} = V^{\sigma}_0 \exp\left(-\frac{r - d_0}{r_0}\right) |\cos\theta_i \cos\theta_j|. \tag{2.10}$$

Following the previous Slater-Koster parametrization (Zhu *et al.*, 2012, Crosse *et al.*, 2020), I set $V^{\pi}_0 = -2.7$ eV, $V^{\sigma}_0 = 0.48$ eV, characteristic distances $a_0 = 1.42$ Å, $d_0 = 3.35$ Å, and the

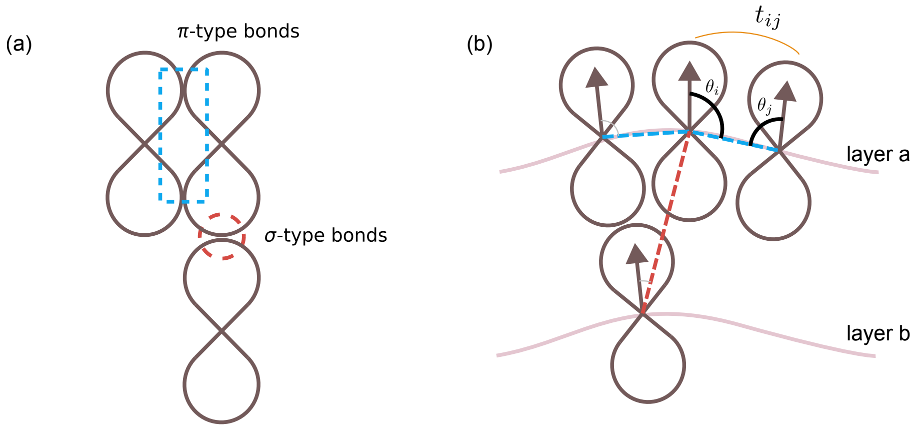

Figure 2.3 – Layout of p_z orbitals and different coupling regimes in the Slater-Koster models. (a) Couplings between p_z orbitals, including the π-bonds and σ-bonds. (b) Local orientations of p_z orbitals and the angles in Slater-Koster models for a coupling t_{ij} : θ_i and θ_j.

decay length $r_0 = 0.184a$. a is the graphene lattice constant, given by $a = \sqrt{3}a_0 = 2.46$ Å. In the orientation-dependent terms, angles θ_i and θ_j are defined as the angle between $\mathbf{r}_{ij}$ and the local normal vector at atomic positions $\mathbf{r}_i$ and $\mathbf{r}_j$, specifically, $\theta_i = \angle(\mathbf{r}_{ij}, \mathbf{n}_i)$ as shown in Fig. 2.3(b). These terms account for the effect of local curvature of the graphene sheet on the overlap between p_z orbitals.

2.4 Wilson loop calculation of topological numbers

The direct calculation of Chern numbers can be done by integrating the Berry curvature, while there is a drawback that such algorithm usually requires very dense momentum points to reach convergence and is thus inefficient. A widely-accepted formalism for calculating the topological invariants is the hybrid Wannier center calculation, or the Wilson loop calculations. Such a method involves finding the Wannier charge center (WCC) of a given set of subbands, and calculate the topological number by the winding of the WCCs.

In this section, I introduce the methods based on Wannier charge center (WCC) sheets to obtain the topological phase. WCC sheets demonstrate the pumping of Wannier functions in real space, which is closely related to the topology of bands. The Chern numbers of the bands are calculated using the formalism of hybrid Wannier function methods introduced by Soluyanov and Vanderbilt (Soluyanov and Vanderbilt, 2011). See also Refs. (Taherinejad *et al.*, 2014, Wu *et al.*, 2017) The Wannier functions $W_n(\mathbf{R})$ are conventionally defined as localized orbitals that are built through integral representation from the Bloch wave functions $u_{\mathbf{k}}$, (Wannier, 1962)

$$W_n(\mathbf{R}) = \frac{1}{(2\pi)^2}\int_{\mathrm{BZ}} d\mathbf{k} e^{i\mathbf{k}\cdot(\mathbf{r}-\mathbf{R})}|u_{n\mathbf{k}}\rangle. \tag{2.11}$$

On the contrary, the hybrid Wannier functions (HWFs) are wannierized only along one of the two spatial dimensions (e.g. x), thus remaining a Bloch-periodic function in momentum along the other dimension (e.g. k_y). HWFs had proved to be useful to diagnose the topological properties, in particular Chern numbers of flat electronic bands (Gresch *et al.*, 2017). The underlying idea is to compute the evolution of the hybrid Wannier functions $|W_n^{(h)}\rangle$ along a k_y-path, and the Chern number is given by the total winding of the Wannier centers. This approach is based on the observation that every nontrivial Chern number presents an obstruction for constructing maximally-localized Wannier functions (Marzari *et al.*, 2012). The numerical advantage of the implement is: instead of finding the full 2D Wannier functions, the program calculates the Wannier charge centers (WCCs) in one of the dimensions (e.g. x), and track it along the momentum on the other dimension (k_y). Here I present an example of the calculation of hybrid Wannier functions. For the 2D electronic system with its eigenstates in BZ being $|u_{\mathbf{k}}(k_x, k_y)\rangle$ in the conventional Bloch band framework, the Wannier charge centers (WCC) are defined through the phase accumulation ϕ_x,

$$|u_{\mathbf{k}}(k_x + 2\pi, k_y)\rangle = e^{i\phi_x}|u_{\mathbf{k}}(k_x, k_y)\rangle, \tag{2.12}$$

The numerical calculations are performed on the samplings of BZ. The phase factor ϕ_x is calculated by evolving from $k_x = 0$ to $k_x = 2\pi$, and tracing the accumulated phase in each increment

$$\phi_x(k_y) = \arg\left[\prod_{i=1}^{n-1} |u_{\mathbf{k}}(k_x^i, k_y)\rangle\,\langle u_{\mathbf{k}}(k_x^{i+1}, k_y)|\right] \tag{2.13}$$

in order to preserve the smooth gauge. Thus defined, the WCC winding on the cylinder determines the Chern numbers by counting the number of times the WCC is crossing the boundaries (Gresch *et al.*, 2017). The winding of the WCC provides the Chern number of a single or a composite band. In multiple-band systems, the total Chern number is determined by the sum of the winding of all the bands. This method is particularly useful for evaluating the Chern numbers of flat electronic bands. A numerical problem arises from the arbitrariness of the eigenstates: the gauge of the eigenstates may not be smooth. Such arbitrariness may eventually lead to a diverging WCC. In practice, singular-value-decomposition (SVD) is performed on the outer-product matrix obtained in each step

$$|u_{\mathbf{k}}(k_x^i, k_y)\rangle\,\langle u_{\mathbf{k}}(k_x^{i+1}, k_y)| = U\Sigma V^*. \tag{2.14}$$

Only the unitary part UV^* is kept, in order to avoid the numerical artifacts.

This approach ensures a smooth gauge over k_x and suppresses the arbitrary phase factors of the multi-band bundle. The winding of the Wannier charge center corresponds to the total Chern number of a set of bands. This can be seen from Eq. 2.13 after rewriting it in a continuous manner:

$$\phi_x(k_y) = \int_{k_x=0}^{2\pi/a} dk_x \langle \psi(k_x, k_y) | \partial_{k_x} | \psi(k_x, k_y) \rangle, \tag{2.15}$$

which comes from reformularing Eq. 2.12 and corresponds to the discretized version Eq. 2.13. And noticing Chern number is expressed as:

$$C = \frac{1}{2\pi} \int_{BZ} d\mathbf{k}\, 2\mathrm{Im} \langle \psi(k_x, k_y) | \partial_{k_y} \partial_{k_x} | \psi(k_x, k_y) \rangle, \tag{2.16}$$

C has the same value as the total winding number of Eq. 2.15:

$$C = \frac{1}{2\pi} \int dk_y \phi_x^{-1} \partial_{k_y} \phi_x. \tag{2.17}$$

2.5 Investigating electron interaction on the basis of TB calculations

Flat bands have garnered significant interest as platforms for adjustable strong electron correlations. In particular, flat bands are predominantly observed in moiré supercells within twisted multilayer systems. The twisting process not only offers extensive tunability for electronic states but also increases the size of unit cells. Performing a comprehensive many-body calculation for moiré supercells is highly challenging. To address the issue of interactions within moiré flat bands, I have devised methods that enable many-body postprocessing based on tight-binding (TB) results.

The idea of such methods is to evaluate the Coulomb interaction within the selected bands, usually the flat bands and their neighbors. There are basically two essentially equivalent approaches. A regular approach is to Wannierize the bands near the Fermi level and construct an effective TB model with much fewer bands. For moiré materials, such a Wannierization is usually performed as a secondary process for the bands calculated by TB models. For example, in the work (Davydov *et al.*, 2022), Wannierizing the TB results produces effective models with four bands or twelve bands. The Wannierization reduces the dimension of the problem from over ten thousands to much smaller numbers which enables further many-body calculations. The only limit of the method lies in Wannier obstruction of topological bands: if the concerned bands are topological several extra bands must be added into the TB model.

A parallel method for such many-body calculation is to use momentum-space eigenstates as the basis set (Abouelkomsan). The interacting Hamiltonian in the momentum space writes:

$$H_{int} = \sum_{\mathbf{q}} V(\mathbf{q}) : \rho(\mathbf{q}) \rho(-\mathbf{q}) :, \tag{2.18}$$

the symbol :: denotes the normal ordering of operators. The density operators $\rho(\mathbf{q})$ is defined as:

$$\rho(\mathbf{q}) = \sum_{k\in BZ} \sum_{i_1,i_2=1}^{N_{sel}} \lambda(\mathbf{k},\mathbf{q}) d^{\dagger}_{\mathbf{k}+\mathbf{q},i_1} d_{\mathbf{k},i_2}, \tag{2.19}$$

which is defined as projected electron density on the N_{sel} selected bands, summed over the orbitals. The $d^{(\dagger)}$ operators are the creation/annihilation operators for energy eigenstates from TB calculation. λ represents the overlap between the eigenstates on different momentum points, which involves the quantum geometry of states into the interaction.

2.6 Landauer-Buttiker Transmission and beyond

Fig. 2.4 (a) presents a typical diagram for two-terminal electronic transmission. In the paper (Meir and Wingreen, 1992), the tunneling current is formulated using Green's function:

$$J = \frac{ie}{\hbar}(G_{Ld} - G^{\dagger}_{dR}) = \frac{ie}{\hbar}\sum(V\langle c^{\dagger}_{ka} d_n\rangle - V^{*}\langle d^{\dagger}_{n} c_{ka}\rangle), \tag{2.20}$$

where $c^{(\dagger)}$ and $d^{(\dagger)}$ represents the annihilation/creation operators in the leads (c) or the device (d). Eq. 2.20 can be alternatively presented in a Landauer-like formalism:

$$J = \frac{ie}{2h}\int dE(\mathrm{Tr}\big[(f_L\Gamma_L - f_R\Gamma_R)(G^r - G^a)\big] + \mathrm{Tr}\big[(\Gamma^L - \Gamma^R)G^<\big]). \tag{2.21}$$

This is Eq. 6 in the original paper (Meir and Wingreen, 1992), where $f_{L(r)}$ are Fermi distribution functions, G is the device Green's function and Γ represents the effects of the lead:

$$\Gamma_{L(R)} = i[\Sigma_{L(R)} - \Sigma^{\dagger}_{L(R)}] \tag{2.22}$$

$$\Sigma_{L(R)} = V^{\dagger} G_{L(R)} V, \tag{2.23}$$

where V is the coupling between the device and the lead. Eq. 2.22 applies to the general cases of transmission, while in the case of weak interactions, it is a good approximation to consider the non-interacting transmission. In the noninteracting case, the transmission equation becomes the Landauer-Buttiker formula:

$$\begin{aligned} J &= \frac{e}{h}\int dE(f_L - f_R)\,\mathrm{Tr}\big[G^r\Gamma^L G^a\Gamma^R\big] \\ T(E) &= \mathrm{Tr}\big[G^r\Gamma^L G^a\Gamma^R\big], \end{aligned} \tag{2.24}$$

where $G^{a(r)}$ are the single-particle Green's functions of the device.

In practice, the leads connected to the device are usually modeled as semi-infinite and periodic structures. As shown in Fig. 2.4, a semi-infinite lead is considered as a series of repetitive unit cells with identical Hamiltonian H_i and inter-cell couplings T. For each of the semi-infinite leads, Green's function G_i is obtained through the recursive Green's function methods. In each

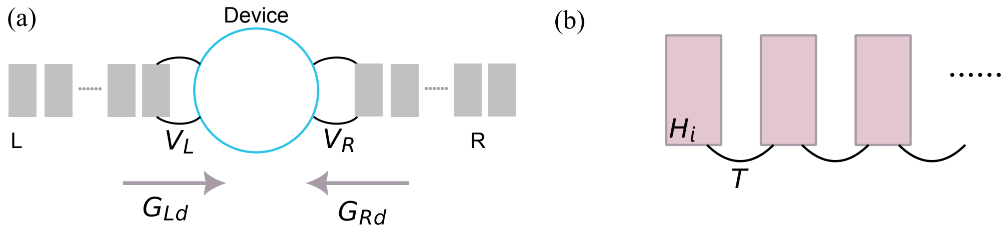

Figure 2.4 – (a) Diagrams of two-terminal transmission setup. The device region is connected to two leads formed by periodic units. (b) An illustration of recursive Green's function algorithm for the lead self-energies.

step, one layer is added to the lead, and the Green's function iterates as $g_j = [E-h-Tg_{j-1}T^\dagger]^{-1}$. The lead Green's function from the i-th semi-infinite lead G_i is taken as the converged value of g, that is, $G_i = g_j^{j\to\infty}$. Subsequently, the self-energy term from the i-the lead is obtained by $\Sigma_i = V_i G_i V_i^\dagger$, where $V_i^{(\dagger)}$ depicts the coupling of the lead to the scattering region.

2.7 Lanczos recursions and the calculation of Hofstadter butterfly in large systems

The Landau level calculation serves as the basis for magneto transport in the quantum regime. Numeric calculation of the Landau levels in crystal systems requires a specific choice of gauge. In practice, I apply the periodic Landau gauge with $\phi = \phi_0 p/q$. The magnetic supercell is q times the original unit cell. As a consequence, there follows the problem of increasing matrix dimension, especially for the calculation of the Hofstadter butterfly in moiré systems. In the models of twisted bilayer graphene, the dimension of the Hamiltonian goes up to a million, calling for special numerical techniques.

Regular diagonalization methods with complexity $O(N^3)$ fail quickly due to the high consumption of computational resources. In order to perform the required calculation of the Hofstadter and Wannier diagrams, I use the Lanczos algorithm implemented in the WannierTools package (Wu *et al.*, 2017). The Lanczos algorithm solves the eigenvalue or density of states problems by iteration, requiring much less memory than the direct diagonalization. The idea of the algorithm is to apply iteratively the Hamiltonian matrix to the set of initial vectors, and subsequently transform the Hamiltonian into a tridiagonal form during the process. To diagonalize a Hamiltonian H, the algorithm starts with an initial vector $|v_1\rangle$ whose norm is 1, each iteration contains the following steps:

1. The main diagonal element is obtained through $\alpha_i = \langle v_i|H|v_i\rangle$;
2. Generate the second vector $|v_{i+1}\rangle = H|v_i\rangle - \alpha_i|v_i\rangle$;
3. Find the sub-leading diagonal $\beta_i = ||H|v_{i+1}\rangle||$;
4. Rescale $|v_{i+1}\rangle = |v_{i+1}\rangle/\beta_i$.

The operations are further performed iteratively until the convergence is achieved. By the above iteration, the Hamiltonian is transformed into a tridiagonal form:

$$H_{\mathrm{tri}} = \begin{pmatrix} \alpha_1 & \beta_1 & 0 & 0 & 0 \\ \beta_1 & \alpha_2 & \beta_2 & 0 & 0 \\ 0 & \beta_2 & ... & \beta_{n-1} & 0 \\ 0 & 0 & \beta_{n-1} & \alpha_n & \beta_n \\ 0 & 0 & 0 & \beta_n & ... \end{pmatrix}. \tag{2.25}$$

Having the tridiagonalized Hamiltonian, the density of states (DOS) is thereafter evaluated through the Green's functions,

$$\rho(E+i\varepsilon) = -\operatorname{Im}\operatorname{Tr}([G(E+i\varepsilon)]) = -\operatorname{Im}\operatorname{Tr}[(E+i\varepsilon)I-H]^{-1}. \tag{2.26}$$

One further applies the continued fraction method to calculate $G=[(E+i\varepsilon)I-H]^{-1}$. For the complex frequency $\Omega=E+i\varepsilon$, the continued fraction representation is

$$G(\Omega) = (\Omega - H_{\mathrm{tri}})^{-1} = \frac{1}{\Omega - \alpha_1 - \frac{\beta_1^2}{\Omega-\alpha_2-\frac{\beta_2^2}{\Omega-...}}}. \tag{2.27}$$

Further-on, the DOS in the selected energy range is obtained by calculating $\operatorname{Tr} G(E)$.

Topological aspects of 2D materials

Part I

3 Landau Levels of the Euler Class Topology

Two-dimensional systems with $C_2\mathcal{T}$ $(P\mathcal{T})$ symmetry exhibit the Euler class topology $E \in \mathbb{Z}$ in each two-band subspace realizing a fragile topology beyond the symmetry indicators. By systematically studying the energy levels of Euler insulating phases in the presence of an external magnetic field, we reveal the robust gaplessness of the Hofstadter butterfly spectrum in the flat-band limit, while for the dispersive bands the gapping of the Landau levels is controlled by a hidden symmetry. We also find that the Euler class E of a two-band subspace gives a lower bound for the Chern numbers of the magnetic subgaps. Our study provides new fundamental insights into the fragile topology of flat-band systems going beyond the special case of $E = 1$ as *e.g.* in twisted bilayer graphene, thus opening the way to a very rich, still mainly unexplored, topological landscape with higher Euler classes.

This Chapter is adapted from the paper:
Yifei Guan*, Adrien Bouhon*, Oleg V. Yazyev
Landau Levels of the Euler Class Topology,
Phys. Rev. Research 4, 023188 (2022)

My contribution includes: initializing the idea of investigating Landau levels of Euler insulators, performing the numerical calculations and proposing the theory to interpret the Hofstadter butterfly with Streda formula.

3.1 Introduction

Since the discovery of the integer quantum Hall effect (QHE) (von Klitzing *et al.*, 1980, von Klitzing, 1986) the concept of topology has played an increasing role in condensed matter physics (Hatsugai, 1993, Thouless *et al.*, 1982, Laughlin, 1981, Stone, 1992, Thouless, 1998, Avron *et al.*, 1983, 1989). The prediction of the quantum spin-Hall effect (Kane and Mele, 2005a,b, Bernevig *et al.*, 2006, Bernevig and Zhang, 2006) and the three-dimensional topological insulators (TI) (Fu *et al.*, 2007, Chen *et al.*, 2009, Qi and Zhang, 2011) protected by time-reversal symmetry have then opened the way to the realization of many novel electronic states and has attracted much attention to the topological aspects of electronic band structures. The role of symmetries has proven essential for the tenfold classification of topological phases of matter (Schnyder *et al.*, 2008, Kitaev, 2009) and its extension to crystalline symmetries (Chiu *et al.*, 2016, Fu and Kane, 2007, Turner *et al.*, 2012, Chiu and Schnyder, 2014, Chiu *et al.*, 2013, Fu, 2011, Fang *et al.*, 2012, Slager *et al.*, 2013, Shiozaki and Sato, 2014, Alexandradinata *et al.*, 2016, Cornfeld and Chapman, 2019). This has recently culminated in systematic classification schemes that address the global band structure topology (Watanabe *et al.*, 2016) in terms of irreducible representation combinatorics (Kruthoff *et al.*, 2017, Bouhon and Black-Schaffer, 2017, Shiozaki *et al.*, 2017), symmetry-based indicators (Po *et al.*, 2017, Khalaf *et al.*, 2018), topological quantum chemistry (Bradlyn *et al.*, 2017, Höller and Alexandradinata, 2018), and real-space topological crystals (Song *et al.*, 2019a, 2020c, Thorngren and Else, 2018, Shiozaki *et al.*, 2018). The discrepancy between the stable symmetry indicators and the topology of split elementary band representations has then led to the definition of crystalline fragile topology for few-band subspaces (Song *et al.*, 2020a, Po *et al.*, 2018a, Song *et al.*, 2020b, Bouhon *et al.*, 2019, Ahn *et al.*, 2019a, Peri *et al.*, 2020).

In its most intriguing form, fragile topology arises without symmetry indicators and is protected by an anti-unitary symmetry that squares to +1 and leaves the momentum invariant, e.g. $P\mathcal{T}$ symmetry in spinless systems, or $C_2\mathcal{T}$ symmetry in two-dimensional spinless and spinful materials, in which case it is called the Euler class topology (Ahn *et al.*, 2018, Bouhon *et al.*, 2020a,b, Zhao and Lu, 2017). Two-dimensional Euler insulating phases have been found to exhibit very rich physics, ranging from the non-Abelian braiding of nodal points (Ahn *et al.*, 2019a, Wu *et al.*, 2019) in electronic band structures (Bouhon *et al.*, 2020a, Chen *et al.*, 2021), in acoustic metamaterials (Jiang *et al.*, 2021) and in the phonon band structures of silicates (Peng *et al.*, 2022a) and Al_2O_3 (Peng *et al.*, 2022b), where it also explains the stability of the Goldstone modes degeneracy at Γ (Park *et al.*, 2021a, Lange *et al.*, 2022). Furthermore, the Euler class topology has been found at the origin of Hopf linking signatures in quenched optical lattices (Ünal *et al.*, 2020), and in the topology in magic-angle twisted bilayer graphene (TBG) (Song *et al.*, 2020a, Po *et al.*, 2019, Liu *et al.*, 2019a).

The unveiling of further robust physical signatures for the Euler class topology is very timely. Recently, the effect of an external magnetic field on effective models of the moiré flat bands in TBG has been reported (Lian *et al.*, 2020a), as well as in other twisted bilayer systems (Lian *et al.*, 2020b). By facilitating much higher magnetic flux per unit cell, moiré super-lattices represent a great venue for the measurement of the Hofstadter butterfly spectrum (Dean *et al.*, 2013, Dana *et al.*, 1985b) as shown in (Wu *et al.*, 2021, Cao *et al.*, 2018b). Reversely, the effect of different band structure topologies on the Hofstadter spectrum has been shown to lead to rich distinctive features (Herzog-Arbeitman *et al.*, 2020).

In this Chapter, we study the effect of the Euler class topology on the Hofstadter spectrum of two-dimensional systems. We reveal qualitative signatures of the Euler class in the flat-band limit and more general non-degenerate and dispersive (non-flat) band structures. In particular, we provide the first systematic study of balanced and imbalanced Euler topological phases, which are characterized by equal, and, respectively, distinct Euler classes below and above the energy gap. While the flat-band limit exhibits a robust gapless Hofstadter spectrum, we unveil a hidden symmetry that controls the gaplessness of the Hofstadter spectrum of the dispersive balanced Euler insulators. We furthermore show that the Hofstadter spectrum of the imbalanced Euler phases is generically gapless.

3.2 Euler class topology

The $C_{2z}\mathcal{T}$ symmetry of a two-dimensional system has $[C_{2z}\mathcal{T}]^2 = +1$ and leaves the momentum of the Bloch states invariant within the two-dimensional Brillouin zone. This guarantees the existence of a basis with a real and symmetric Bloch Hamiltonian, $H \to \widetilde{H} = \widetilde{H}^T \in \mathbb{R}^N \times \mathbb{R}^N$ (Bouhon *et al.*, 2020a). We are here excluding non-orientable phases characterized by π-Berry phases along some non-contractible loops of the Brillouin zone (Ahn *et al.*, 2018, Bouhon *et al.*, 2020b). The Euler class $E \in \mathbb{Z}$ of real oriented rank-2 vector bundles (Hatcher, 2003) then characterizes the two-dimensional topology of every (orientable) two-band vector subspace V^α of the band structure, which we label by $\alpha = I, II, \ldots,$ *i.e.* $V^\alpha = \langle u^\alpha_a, u^\alpha_b \rangle_{\mathbb{R}^2}$ is the vector space spanned by the eigenvectors $\{u^\alpha_n\}_{n=a,b}$ corresponding to the eigenvalues $\{\epsilon^\alpha_n\}_{n=a,b}$ obtained from the spectral decomposition $\widetilde{H} u^\alpha_n = \epsilon^\alpha_n u^\alpha_n$, where we assume the energy ordering $\epsilon^\alpha_n < \epsilon^{\alpha+I}_n$ $(n = a, b)$. Then, the topology for any group of bands with more than two bands is reduced to the second Stiefel-Whitney class $w_2 = E \bmod 2 \in \mathbb{Z}_2$ (Ahn *et al.*, 2019a, 2018, Bouhon *et al.*, 2020a,b, Zhao and Lu, 2017), *i.e.* there is a $\mathbb{Z} \to \mathbb{Z}_2$ reduction specific to fragile topology. In particular, any two-band subspace with an even Euler class is trivialized when a third (trivial) band is added to the band-subspace. The Euler class of the α-th two-band subspace is computed through the integral (Xie *et al.*, 2020, Ahn *et al.*, 2019a, 2018, Bouhon *et al.*, 2020a, Zhao and Lu, 2017)

$$E_\alpha = \frac{1}{2\pi} \int_{\mathrm{BZ}} dk_1 dk_2 \, \mathrm{Eu}_\alpha, \tag{3.1}$$

over BZ$=[-\pi,\pi)^2$, the Brillouin zone of the two-dimensional lattice, with the integrand given by the Euler curvature

$$\begin{aligned} \mathrm{Eu}_\alpha &= \mathrm{Pf} F[(u^\alpha_a \; u^\alpha_b)], \\ &= (\partial_{k_1} u^\alpha_a)^T \cdot (\partial_{k_2} u^\alpha_b) - (\partial_{k_2} u^\alpha_a)^T \cdot (\partial_{k_1} u^\alpha_b), \end{aligned} \tag{3.2}$$

here defined as the Pfaffian of the two-state Berry curvature

$$\begin{aligned} F[(u^\alpha_a \; u^\alpha_b)] &= F[|\mathbf{u}_\alpha\rangle], \\ &= -\mathrm{i} \left(\langle \partial_{k_1} \mathbf{u}_\alpha | \partial_{k_2} \mathbf{u}_\alpha \rangle - \langle \partial_{k_2} \mathbf{u}_\alpha | \partial_{k_1} \mathbf{u}_\alpha \rangle \right), \end{aligned} \tag{3.3}$$

with the matrix of two column eigenvectors $|\mathbf{u}_\alpha\rangle = (u^\alpha_a \; u^\alpha_b)$. Alternatively, the Euler class can be obtained as the winding of the two-band Wilson loop (Bouhon *et al.*, 2019, Xie *et al.*, 2020, Ahn *et al.*, 2019a, 2018, Bouhon *et al.*, 2020a), see Fig. 3.1. Interestingly, Eq. 3.2 motivates yet another way to compute the Euler class. Defining the *Chern basis*

$$\begin{aligned} v_+^\alpha &= (u_a^\alpha + \mathrm{i} u_b^\alpha)/\sqrt{2}, \\ v_-^\alpha &= (u_a^\alpha - \mathrm{i} u_b^\alpha)/\sqrt{2}, \end{aligned} \tag{3.4}$$

and writing the one state Berry curvature $F[v_+^\alpha] = (\partial_{k_1} v_-^\alpha)^T \cdot (\partial_{k_2} v_+^\alpha) - (\partial_{k_2} v_-^\alpha)^T \cdot (\partial_{k_1} v_+^\alpha)$, we readily find $\mathrm{Eu}_\alpha = F[v_+^\alpha]$, from which we obtain (Bouhon *et al.*, 2020a) the Euler class as a one-band Chern number

$$E_\alpha = \frac{1}{2\pi} \int_{\mathrm{BZ}} dk_1 dk_2 \, F[v_+^\alpha] = C. \tag{3.5}$$

In the limit of degenerate bands ($\epsilon_a^\alpha = \epsilon_b^\alpha$), the Chern basis becomes an eigenbasis of $\widetilde{H}$. This plays an important role in the flat-band limit discussed below. An essential observable associated with the Euler class E_α is the number $2|E_\alpha|$ of *stable* nodal points hosted by the $\alpha(=I,II)$-th two-band subspace (*i.e.* the nodes cannot be annihilated as long as the energy gaps above and below the two-band subspace remain open), see *e.g.* the four stable nodes in each two-band subspace of Fig. 3.1(a) for the Euler phase with $E_I = E_{II} = 2$. These nodes cannot be annihilated as long as the energy gaps above and below the two-band subspace remain open (Ahn *et al.*, 2019a, Bouhon *et al.*, 2020a,b). This must be contrasted for instance with the two nodes of graphene that can be annihilated upon breaking the C_6 crystal symmetry while preserving $C_2\mathcal{T}$ symmetry.

3.3 Four-band real symmetric Hamiltonian

In the following, we consider a four-orbital system that is insulating at half-filling $\nu = N_{\mathrm{occ}}/N_{\mathrm{orb}} = 1/2$, with N_{orb} the total number of orbitals (*i.e.* either four spinless orbitals, or two spin-1/2 pairs) and N_{occ} the number of bands below the energy gap. The most general four-band real symmetric Bloch Hamiltonian is spanned by nine real independent terms, *i.e.*

$$\widetilde{H} = \sum_{i,j=0,x,y,z} h_{ij} \Gamma_{ij}, \tag{3.6}$$

for $\Gamma_{ij} = \sigma_i \otimes \sigma_j$ and $i,j = 0,x,y,z$ with $\sigma_{x,y,z}$ the Pauli matrices and $\sigma_0 = \mathbb{1}$, under the constraint that only the terms with $\mathrm{Im}\,\Gamma_{ij} = 0$ are kept. Thus, the most general Bloch Hamiltonian is parametrized by only ten parameters,

$$\{h_{00}, h_{0x}, h_{0z}, h_{x0}, h_{xx}, h_{xz}, h_{yy}, h_{z0}, h_{zx}, h_{zz}\} \in \mathbb{R}. \tag{3.7}$$

In the following, we,discard the term h_{00} since it does not affect the topology.

We first consider the Hofstadter butterfly in the limit of flat bands. The flat-band limit of the Euler insulating phases implies the two-by-two degeneracy of the bands since each two-band subspace with a non-zero Euler class hosts stable nodal points, as we have seen above. The most general four-band Bloch Hamiltonian (real and symmetric) with a gapped and flat spectrum, *i.e.* we set the eigenvalues to $(\epsilon_1, \epsilon_2, \epsilon_3, \epsilon_4) = (-1,-1,1,1)$, takes the form (see Sec.

3.8)

$$\begin{aligned}\widetilde{H}[\mathbf{n},\mathbf{n}'] = n'_1(&-n_1\Gamma_{zz}+n_2\Gamma_{zx}+n_3\Gamma_{x0})\\ -\, n'_2(&+n_1\Gamma_{xz}-n_2\Gamma_{xx}+n_3\Gamma_{z0})\\ +\, n'_3(&+n_1\Gamma_{0x}+n_2\Gamma_{0z}-n_3\Gamma_{yy}) \quad ,\end{aligned} \tag{3.8}$$

which depends on two unit vectors

$$\begin{aligned}\mathbf{n}^{(\prime)} &= (n_1^{(\prime)}, n_2^{(\prime)}, n_3^{(\prime)})\\ &= (\cos\phi^{(\prime)}\sin\theta^{(\prime)}, \sin\phi^{(\prime)}\sin\theta^{(\prime)}, \cos\theta^{(\prime)}).\end{aligned} \tag{3.9}$$

The Bloch Hamiltonian Eq. 3.8 thus defines a mapping from the Brillouin zone onto two unit spheres, $(k_1, k_2) \mapsto (\mathbf{n},\mathbf{n}') \in (\mathbb{S}^2, \mathbb{S}^{2'})$, the Fourier transform of which defines a tight-binding model (Bouhon *et al.*, 2020b). The topology of Eq. 3.8 is then determined by two skyrmion numbers,

$$q = W[\mathbf{n}] \text{ and } q' = W[\mathbf{n}'], \tag{3.10}$$

computing the winding of the unit vectors through

$$W[\mathbf{n}^{(\prime)}] = \frac{1}{4\pi}\int_{\mathrm{BZ}} dk_1 dk_2\, \mathbf{n}^{(\prime)} \cdot (\partial_{k_1}\mathbf{n}^{(\prime)} \times \partial_{k_2}\mathbf{n}^{(\prime)}) \in \mathbb{Z}. \tag{3.11}$$

The Euler classes of the two two-band subspaces are then readily obtained from the Skyrmion numbers (Bouhon *et al.*, 2020b) (see Sec. 3.8)

$$E_I = q - q', \quad E_{II} = q + q'. \tag{3.12}$$

We importantly note that the sign of the Euler classes can be flipped in pair, *i.e.* $(E_I, E_{II}) \to (-E_I, -E_{II})$, under an adiabatic transformation of the Hamiltonian which is obtained from the nontrivial action of the generator of $\pi_1[\mathsf{Gr}^{\mathbb{R}}_{2,4}] = \mathbb{Z}_2$ on $\pi_2[\mathsf{Gr}^{\mathbb{R}}_{2,4}] = \mathbb{Z}^2$ (Bouhon *et al.*, 2020b).

In the following we distinguish between two classes of phases, the *balanced* phases for which $|E_I| = |E_{II}|$, and the *imbalanced* phases with $|E_I| \neq |E_{II}|$. The balanced phases are readily obtained by setting one skyrmion number to zero, *e.g.* fixing $\mathbf{n}' = (0,1,0)$ Eq. 3.8 gives

$$\begin{aligned}\widetilde{H}_{\mathrm{bal}}[\mathbf{n}] &= \widetilde{H}[\mathbf{n},(0,1,0)],\\ &= -n_1\Gamma_{xz} + n_2\Gamma_{xx} - n_3\Gamma_{z0},\end{aligned} \tag{3.13}$$

which is characterized by $q' = 0$ and $E_I = E_{II} = q$. Moreover, it can be shown that every pair of balanced phases $(E_I, E_{II}) = (\bar{q}, \bar{q})$, i.e. setting $q = \bar{q}$ and $q' = 0$, and $(E_I, E_{II}) = (-\bar{q}, \bar{q})$, i.e. setting $q = 0$ and $q' = \bar{q}$, are homotopy equivalent (Bouhon and Slager, 2022). The imbalanced phases are then realized when both skyrmion numbers q and q' are nonzero, such that the nine terms in Eq. 3.8 are nonzero. Limiting ourselves to $E_I + E_{II} \leq 4$ and $E_I, E_{II} \geq 0$, we discuss the balanced phases for $(E_I, E_{II}) = (1,1), (2,2)$, and the imbalanced phases for $(E_I, E_{II}) = (0,2), (1,3)$. Fig. 3.1 presents the band structure and the Wilson loop of the balanced phase (E_I, E_{II})=(2,2). Since we do not find any qualitative difference in the Hofstadter spectrum

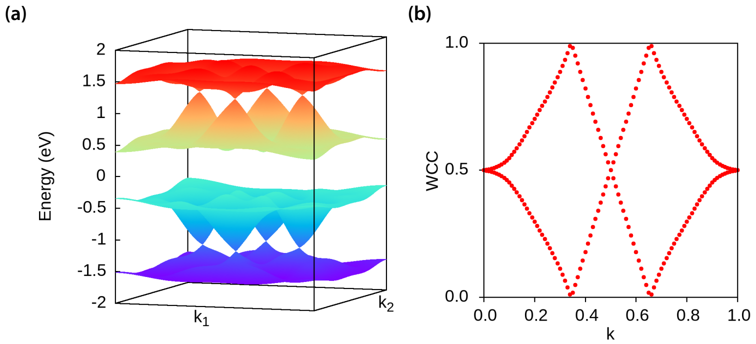

Figure 3.1 – (a) Band structure of the tight-binding model of the balanced phase with the Euler class $E_I = E_{II} = 2$. Four nodal points are present in each two-band subspace as a manifestation of the nontrivial Euler topology. (b) The value of the Euler class can be computed through the winding number, here 2, of the two-band Wilson loop.

between the phases $(E_I, E_{II}) \sim (-E_I, -E_{II})$ and $(E_I, -E_{II}) \sim (E_I, -E_{II})$, it is enough to show the results for $E_I, E_{II} \geq 0$.

3.4 Hofstadter Spectrum

The effect of an external magnetic field $\mathbf{B} = \nabla \times \mathbf{A}$ is most conveniently introduced through the Peierls substitution $t_{ij} \to \tilde{t}_{ij} = t_{ij} \exp(\mathrm{i}\phi_{ij})$ with $\phi_{ij} \propto \int_{\mathbf{R}_i}^{\mathbf{R}_j} \mathbf{A} \cdot d\mathbf{r}$ (Graf and Vogl, 1995). Restricting to a rational magnetic flux, *i.e.* $\phi = \int_{\text{u.c.}} B d^2\mathbf{r} = 2(r/s)\phi_0$ with r and s coprime integers ($\phi_0 = h/e$ is the magnetic flux quantum), the magnetic tight-binding Hamiltonian acquires a reduced periodicity with a magnetic unit cell (Herzog-Arbeitman *et al.*, 2020) that is s times as large as the non-magnetic one. It follows that the rotation C_{2z} acts as a nontrivial permutation of the s sub-lattice sites of the magnetic unit cell, leading to the breaking of $C_{2z}\mathcal{T}$ symmetry. We emphasize that while C_{2z} is not necessarily a symmetry of the Hamiltonian, $C_{2z}\mathcal{T}$ alone imposes the C_{2z}-symmetric spatial configuration of the atomic orbitals since $\mathcal{T}$ does not affect the position operator. In other words, any orbital φ_β located away from a C_{2z} center, say $\mathbf{r}_\beta$, must have a C_{2z} partner located at $C_{2z}\mathbf{r}_\beta$. As a consequence of the breaking of $C_{2z}\mathcal{T}$ by the external magnetic field, the $2E_\alpha$ nodal points of each two-band subspace become gapped leading to magnetic Chern bands, see Section 3.6.

We show the standard Hofstadter butterfly spectrum of a gapped phase with trivial bands in Fig. 3.2(a), computed here for a two-band system with each band with finite bandwidth. In particular, the gap of the zero-field phase is preserved at a finite field. On the contrary, the Hofstadter spectrum of the nontrivial Chern phase is gapless, see Fig. 3.2(b) for the two-band system now with $C = \pm 1$ Chern numbers. The closing of the gap is here explained by the change of the filling factor of the principal gap as a function of the magnetic flux, *i.e.* according to the Streda formula $\nu = C\phi/2 + 1/2$ for a filling $\nu_0 = 1/2$ at zero fields (Dana *et al.*, 1985b).

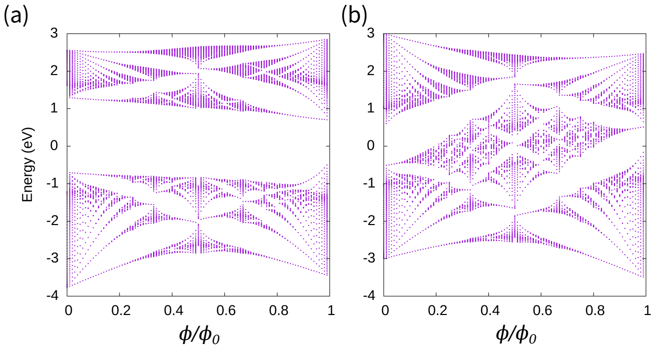

Figure 3.2 – Hofstadter butterfly spectrum for a gapped two-band model with (a) trivial bands and (b) topological bands with the Chern numbers $C = +1$ in the lower band and $C = -1$ in the upper band. The Chern gap reaches the band edge in (b) as predicted by the Streda formula.

Similarly, while the Hofstadter spectrum of the phase with trivial Euler topology ($E_I = E_{II} = 0$) is gapped, we show that the nontrivial Euler phases exhibit gapless Hofstadter spectra with the crossing of the Landau levels at half-filling ($\nu = 1/2$), *i.e.* within the gap of the zero-field phases, at a finite magnetic flux. In this work, we identify several qualitative features of the Hofstadter spectrum that relate to the finite Euler classes $E_{I,II}$ of the phases at zero fields. The Hofstadter spectrum, band structures and the Wilson loop calculations are performed with the open-source package WannierTools (Wu *et al.*, 2018).

3.5 Flat-band limit

In the limit of small flux, the effect of an external magnetic field B on the energy levels takes the semi-classical form (Gao *et al.*, 2015, Shi *et al.*, 2007, Alexandradinata and Glazman, 2018, Wang *et al.*, 2019)

$$\epsilon_{n,B}(k) \approx \epsilon_{n,0}(k) + m_n(k)\,B, \tag{3.14}$$

where $\epsilon_{n,0}(k)$ is the energy eigenvalue at zero flux, and $m_n(k)$ describes the orbital magnetic susceptibility of the n-th band. In the case of TBG, it has been shown that $m_n(k)$ is related to the band topology at zero fields (Wu *et al.*, 2021). More generally, the orbital magnetic susceptibility has contributions both from Berry curvature (Resta, 2010, Thonhauser *et al.*, 2005, Thonhauser, 2011) and from the quantum geometry of the bands (Piéchon *et al.*, 2016, Hwang *et al.*, 2021). By minimizing the effect of dispersion, the flatness of the bands thus makes the Landau levels a good probe of the topology and the quantum geometry of the bands (Rhim *et al.*, 2020).

Figure 3.3 shows the Hofstadter butterfly spectrum for different Euler phases in the flat-band limit. We find the qualitative trend that the crossing point of the Landau levels at half-filling moves toward zero for higher Euler classes, *i.e.* the minimum magnetic field at which the Landau levels cross, ϕ_{cross}, decreases with increasing Euler classes.

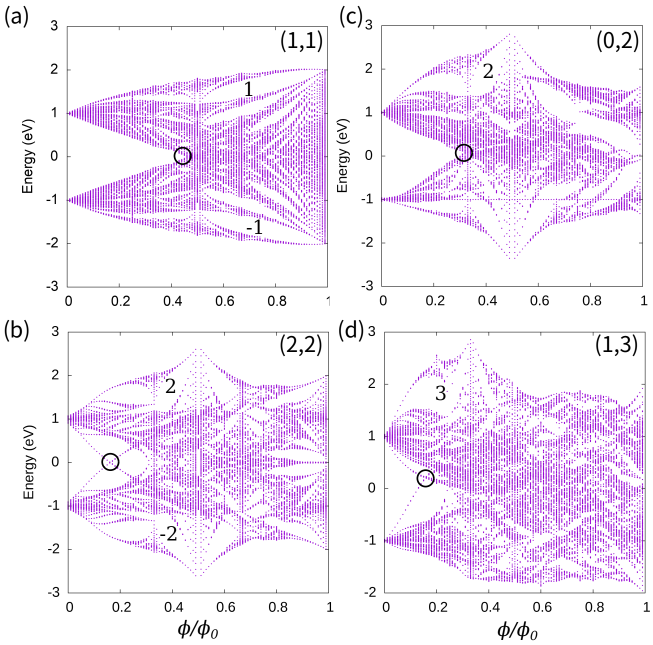

Figure 3.3 – Hofstadter butterfly spectra calculated in the flat-band limit for the balanced phases with Euler classes (E_I,E_{II}) of (a) (1,1), (b) (2,2) and the imbalanced phases with (E_I,E_{II}) of (c) (0,2) and (d) (1,3). The Chern numbers of the main magnetic band gaps are written on the pictures.

We now give the rationale for the gap-closing of the Hofstadter butterfly. Starting with the balanced phases, Fig. 3.3(a,b), we show in Sec. 3.10 that every $C_{2z}\mathscr{T}$-symmetric Bloch Hamiltonian with *two-by-two* degenerate bands is *necessarily* symmetric under an effective basal mirror symmetry $m_z = C_{2z}I$, with I the inversion symmetry and C_{2z} a spinful π-rotation (*i.e.* $C_{2z}^2 = -1$) around the axis perpendicular to the basal plane of the two-dimensional system. The degenerated system is thus symmetric under the magnetic point group $2'/m = \{E, m_z, C_{2z}\mathscr{T}, I\mathscr{T}\}$, with $[C_{2z}\mathscr{T}]^2 = +1$ and $[I\mathscr{T}]^2 = -1$, where the $I\mathscr{T}$ symmetry implies Kramers degenerate bands at all momenta. We conclude that the degenerate limit exists for all balanced Euler insulating phases without the need for fine-tuning. In other words, the degeneracy of the bands is always associated with a symmetry of the Hamiltonian such that it is not accidental (see Sec. 3.10 for a detailed exposition). We also find that the Chern basis Eq. 3.4, *i.e.* an eigenbasis of the balanced Hamiltonian in the flat-band limit, is an eigenbasis of the m_z symmetry operator (Sec. 3.10). There is thus a one-to-one correspondence between the Euler class and the mirror Chern number of the occupied bands, that is (Sec. 3.10)

$$E_I = E_{II} = -C^{(-\mathrm{i})} = C^{(\mathrm{i})} \in \mathbb{Z}. \tag{3.15}$$

Interestingly, the enrichment of $C_{2z}\mathscr{T}$-symmetric phases with m_z symmetry implies that each two-band vector subbundle becomes oriented with the signed Euler class as topological invariant, *i.e.* $E_I^{(-\mathrm{i})} \in \mathbb{Z}$, by virtue of attaching a fixed orientation to each mirror-eigenvalue sector (Sec. 3.10). Given that m_z-symmetry is preserved at finite magnetic field B_z, the crossings between Landau levels of distinct mirror eigenvalues are protected by symmetry. We now can derive the qualitative trend as a function of the Euler class from the Streda formula $\nu = C^{(\mp \mathrm{i})}\phi/2 + \nu_0$ with $\nu_0 = 1/2$ the filling at zero flux (Dana *et al.*, 1985b). Indeed, the subband with Chern number $C^{(\mp \mathrm{i})}$ must reach the band edge ($\nu = 0, 1$) at $\phi = 1/|C^{(\mp \mathrm{i})}|$, which gives an upper bound for the gap-closing flux in each m_z-eigensector (see Fig. 3.2(b) showing the Hofstadter spectrum of a generic Chern insulating phase with $C = +1$ in the lower band). More precisely, the occupied Landau levels at half-filling with a Chern number $C_v = \max\{C_I^{(-\mathrm{i})}, C_I^{(\mathrm{i})}\}$ at zero flux must reach the filling $\nu = C_v/2 + 1/2$ at the flux $\phi = 1$ (*e.g.* $\nu = 1$ if $C_v = 1$), while the conduction Landau levels at half-filling with a Chern number $C_c = \max\{C_{II}^{(-\mathrm{i})}, C_{II}^{(\mathrm{i})}\}$ at zero flux must reach the filling $\nu = -C_c/2 + 1/2$ (note the sign change for the conduction bands) at the flux $\phi = 1$ (*e.g.* $\nu = 0$ if $C_c = 1$). Furthermore, if $C_v = C_I^{(-\mathrm{i})} > 0$ (and thus $C_v = C_I^{(\mathrm{i})} > 0$), then $C_c = C_{II}^{(\mathrm{i})} > 0$ (and $C_c = C_{II}^{(-\mathrm{i})} > 0$), since $C_I^{(\mp \mathrm{i})} + C_{II}^{(\mp \mathrm{i})} = 0$. We hence conclude that Landau levels of distinct m_z-eigenvalues must cross at half-filling (see also (Herzog-Arbeitman *et al.*, 2020)), with the trend through Eq. 3.15 of a smaller gap-closing flux for a higher Euler class. This is in agreement with the numerical results.

We now consider the imbalanced phases ($|E_I| \neq |E_{II}|$) in the flat-band limit, shown in Fig. 3.3(c,d), where the same trend is observed. Contrary to the balanced case, there is no effective mirror symmetry. This implies that the two-by-two band degeneracy requires fine-tuning. We find that the exact degeneracy, similarly to the flat-band limit, requires infinite-range hopping terms in the tight-binding model. In practice, it can be achieved in very good numerical approximation by keeping hopping terms up to sufficiently far neighbours, see Sec. 3.8. The absence of effective mirror symmetry in the imbalanced Euler phases leaves unexplained the stability of the Landau level crossing at half-filling [Fig. 3.3(c,d)]. Nevertheless, by making use of the Chern basis Eq. 3.4 as the eigenbasis (permitted by the two-by-two degeneracy of the bands), we can still decompose the bands at zero magnetic fields into two decoupled imbalanced Chern insulators, *i.e.* $H = H^+ \oplus H^-$ with $C_I^{\pm} = \pm E_I$ and $C_{II}^{\pm} = \mp E_{II}$. The stability of the gaplessness of the Hofstadter spectrum, Fig. 3.3(c,d), suggests that the effect of the magnetic field introduced via the Peierls substitution preserves the decoupling between the two Chern sectors, even though there is no global symmetry of the Hamiltonian protecting the decoupling (like m_z in the balanced case).

3.6 Dispersive bands

We are now ready to address the more general situation of dispersive (non-flat) and non-degenerate Euler insulating phases [*e.g.* Fig. 3.1(a)]. Any adiabatic perturbation of Eq. 3.8 removes the degeneracy and the flatness of the bands while preserving the Euler class topology. From the Hofstadter spectra shown in Fig. 3.4, we readily find that the gaplessness at half-filling remains a feature of the nontrivial Euler insulating phases, both for the balanced Fig. 3.4(a,b) and imbalanced Fig. 3.4(c,d) phases. This is somehow surprising since the non-degenerate balanced phases do not preserve the effective m_z-symmetry (*i.e.* there is no mirror Chern number), and the Chern basis [Eq. 3.4] are not eigenvectors of the Hamiltonian anymore. We

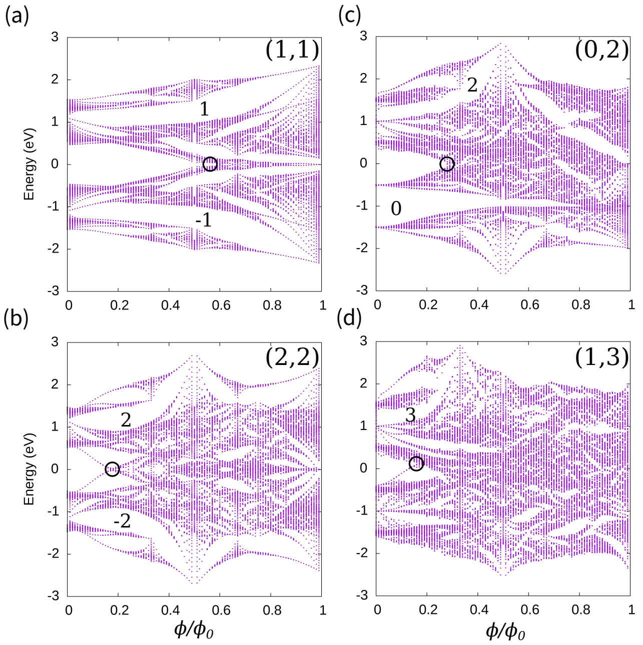

Figure 3.4 – Hofstadter butterfly spectra calculated for the Euler insulating phases away from the flat-band and degenerate limit for Euler classes (a) (1,1), (b) (2,2), (c) (0,2) and (d) (1,3). While the effective m_z-symmetry is broken, the balanced phases all satisfy the hidden symmetry (see text). The magnetic subgap Chern numbers are bounded from below by the Euler classes.

hence would conclude that, in principle, the crossing of the Landau level branches in the gap at half-filling is not protected, as was reported in Ref. (Herzog-Arbeitman *et al.*, 2020) for the $E_I = E_{II} = 1$ case. We give below an explanation for Landau-level crossings in the phases with nonzero Euler classes at zero-field.

We first resolve the apparent contradiction, *i.e.* the observed Landau-level crossings without symmetry protection, in the case of the balanced phases. By systematically probing all perturbations of the Euler insulating phases allowed by $C_{2z}\mathcal{T}$ symmetry, we find that only the term h_{yy} added to $\widetilde{H}_{\text{bal}}[\mathbf{n}]$ [Eq. 3.13] controls the gapping of the Hofstadter spectrum, see Fig. 3.5(a,b) obtained with a constant term $h_{yy} = \delta > 0$ added adiabatically. (See Sec. 3.11, for a detailed discussion of all the symmetry-allowed perturbations.) Since there is no global symmetry that can account for the vanishing or non-vanishing of this term, we call the condition $h_{yy} = 0$ a *hidden symmetry* of the balanced Euler insulating phases described by Eq. 3.13. We note that under a change of orbital basis of the Bloch Hamiltonian, the term that controls the hidden symmetry must be changed accordingly. We emphasize that all the balanced Euler phases at zero flux shown in Fig. 3.4(a,b) satisfy the hidden symmetry, *i.e.* all the terms h_{ij} in Eq. 3.7 are non-zero except h_{yy}.

The imbalanced phases on the contrary are mainly unaffected by $C_{2z}\mathcal{T}$-preserving perturbations, exhibiting a robust gapless Hofstadter spectrum, as one can see in the results Fig. 3.5(d-f)

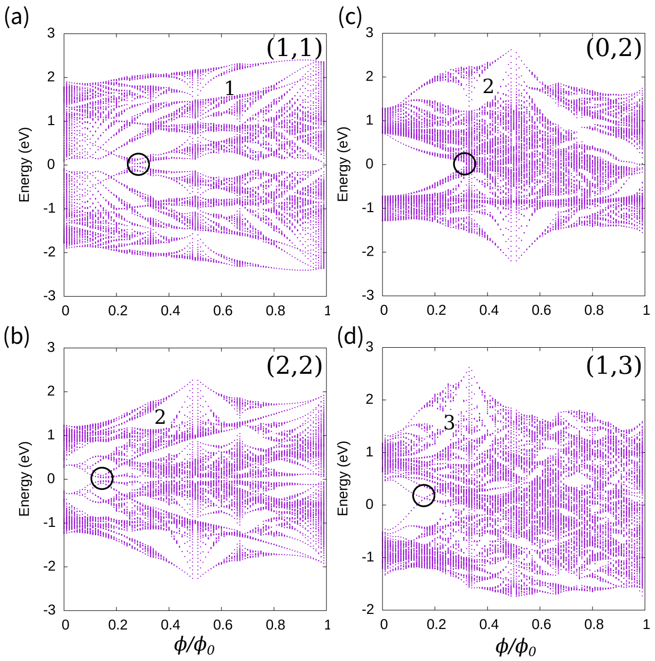

Figure 3.5 – Effect of breaking the hidden symmetry on the Hofstadter butterfly spectra for balanced (a) (1,1), (b) (2,2) and imbalanced (c) (0,2), (d) (1,3) phases. The imbalanced phases remain gapless. The magnetic subgap Chern numbers are still bounded from below by the Euler classes.

obtained for $h_{yy} \neq 0$. This can be understood by noting that the flat degenerate imbalanced Bloch Hamiltonian, Eq. 3.8 with $q, q' \neq 0$, already has all the nine independent terms h_{ij} in Eq. 3.7 nonzero and without relations between them, such that a further perturbation in h_{yy} does not lead to a qualitative change of the spectrum.

3.6.1 Magnetic sub-gaps

When the nodal points, located at quarter fillings $\nu = 1/4, 3/4$, are well separated in energy from the rest of the bands, we can easily identify the Landau levels originating from the nodes at a small magnetic flux. We find that the number of stable nodal points contained in each two-band subspace gives a lower bound for the Chern numbers of the magnetic sub-gaps above and below these Landau levels, *i.e.* $2|E_\alpha| \leq |C_{\nu=(2[\alpha]-1)/4}|$ with $[\alpha]$ defined by $[I] = 1$ and $[II] = 2$. Indeed, the Chern numbers of the magnetic sub-gaps can be increased by adding unstable nodes, such as e.g. in graphene, while the Euler class dictates the minimal number of nodes to be $2|E_\alpha|$ in each two-band subspace.

3.7 Discussion

We briefly discuss the difference between the Landau levels of Euler insulators with the Landau levels of mirror Chern insulators and time-reversal symmetric topological insulators (*i.e.* the Kane-Mele $\mathbb{Z}_2$ quantum spin Hall phases). First of all, despite the existence of a mirror (m_z) Chern number in the (flat) two-by-two degenerate Euler phases, the Euler insulators, in general, are different from mirror Chern insulators by their fragility. That is, while the mirror Chern topology is stable, the $\mathbb{Z}$ Euler topology of two-band subspaces is reduced to the $\mathbb{Z}_2$ second Stiefel-Whitney class topology under the addition of trivial bands (Po *et al.*, 2018a, Bouhon *et al.*, 2019, Ahn *et al.*, 2019a, Lian *et al.*, 2020a). Furthermore, the $\mathbb{Z}_2$ Stiefel-Whitney insulators, which have no topological edge states, are also distinct from the Kane-Mele $\mathbb{Z}_2$ phases, with topological helical edge states. In the context of the Hofstadter spectrum, time-reversal symmetry is broken by the magnetic field and, if no other symmetry is present, the $\mathbb{Z}_2$ Kane-Mele phases exhibit a gapped Hofsdtater spectrum (Herzog-Arbeitman *et al.*, 2020).

We now discuss the potential candidates for observing the manifestations of Euler topology in the Hofstadter spectrum. Since the Landau levels rely on the effect of the magnetic field, our findings can be more naturally realized in electronic systems than in charge-neutral systems, such as optical lattices (Ünal *et al.*, 2020) or acoustic metamaterials (Jiang *et al.*, 2021). In that sense, the family of materials with moiré superlattices would be of interest. Indeed, moiré superlattices in twisted heterostructures provide the possibility to realize and tune the fragile topology, while the large supercell facilitates the measurement of the Hofstadter butterfly that requires a very high magnetic flux per unit cell. We for instance propose the $M+N$ twisted multilayer graphene built by stacking the M-layer and N-layer graphene multilayers with a twist as a platform for realizing Euler insulators with arbitrary topological charge, since in such superlattices the flat bands can carry ($M-N$) Chern numbers (Zhang *et al.*, 2020a, Liu *et al.*, 2019c).

To conclude, we have studied the response of $C_2\mathcal{T}$ symmetric fragile topological insulators to external magnetic fields with tight-binding models hosting a variety of balanced and imbalanced Euler insulating phases. We have shown that the Hofstadter energy spectrum is affected qualitatively by the topological Euler class, especially in the flat-band limit. Our results also provide an insight for the study of topological flat-band systems with non-trivial quantum metrics, such as the topologically bounded superfluid weight found in twisted multilayered systems (Xie *et al.*, 2020) or the divergence found in the Landau levels of anomalous flat bands (Rhim *et al.*, 2020), generalizing to the very rich, yet mainly unexplored, landscape of higher Euler class phases.

During the investigation of exact flat-band models of Euler insulators, we noticed the signatures of Euler class in the edge spectra. Such discovery leads to the work on the bulk-boundary correspondence of Euler insulators, in Chapter. 4.

3.8 The modelling of Euler insulating phases

3.8.1 The geometric approach

We here briefly review the construction of the homotopy representative Hamiltonian for the four-band Euler insulating phases at half-filling following Ref. (Bouhon *et al.*, 2020b, Bouhon, 2020).

The spectral decomposition of the 4×4 real symmetric Hamiltonian $\widetilde{H}$, *i.e.* $\widetilde{H} u_n = \epsilon_n u_n$ with the eigenvalue ϵ_n and the eigenvector $u_n \in \mathbb{R}^4$ for $n = 1,\dots,4$, gives $\widetilde{H} = R \cdot D \cdot R^T$ with $R = (u_1\ u_2\ u_3\ u_4) \in \mathsf{SO}(4)$ the matrix of real eigenvectors and $D = \mathrm{diag}(\epsilon_1, \epsilon_2, \epsilon_3, \epsilon_4)$ the matrix of energy eigenvalues. In the following we set $\epsilon_1 = \epsilon_2 = -\epsilon$ and $\epsilon_3 = \epsilon_4 = \epsilon > 0$.

From the spectral decomposition and the degeneracy of the energy levels, we readily have that $\widetilde{H}$ is invariant under any gauge transformation $R \to RG$ with $G = G_v \oplus G_c$ and $G_v, G_c \in \mathsf{O}(2)$, such that $\det G = \det(G_v) \det(G_c) = 1$. Defining the corresponding left coset $[R] = \{RG | G \in \mathsf{S}[\mathsf{O}(2) \times \mathsf{O}_2]\}$, we thus find that the Hamiltonian is an element of the real *unoriented* Grassmannian as $[R] \in \mathsf{SO}(4)/\mathsf{S}[\mathsf{O}(2) \times \mathsf{O}(2)] = \mathrm{Gr}_{2,4}^{\mathbb{R}}$.

We are here excluding non-orientable phases characterized by π-Berry phases along the two non-contractible loops of the Brillouin zone. While the Hamiltonian defines an *orientable* vector bundle (see Sec. 3.8.2 below) (Bouhon *et al.*, 2020b), it is convenient to first seek an element of the real *oriented* Grassmannian $\widetilde{\mathrm{Gr}}_{2,4}^{\mathbb{R}} = \mathsf{SO}(4)/[\mathsf{SO}(2) \times \mathsf{SO}(2)]$ to construct the Hamiltonian. This allows us to take advantage of the diffeomorphism $\widetilde{\mathrm{Gr}}_{2,4}^{\mathbb{R}} \cong \mathbb{S}^2 \times \mathbb{S}^2$. Starting from the explicit parametrization of R as a generic element of $\mathsf{SO}(4)$, the reduction to the oriented Grassmannian is then carried out through the Plücker embedding permitting the representation of the Grassmannian as a 4-dimensional manifold subspace of a 6-dimensional vector space (the second exterior power of $\mathbb{R}^4$), *i.e.*

$$\iota : \widetilde{\mathrm{Gr}}_{2,4}^{\mathbb{R}} \hookrightarrow \bigwedge\nolimits^2(\mathbb{R}^4) : [R] \mapsto (\mathbf{n}_+, \mathbf{n}_-) \in \mathbb{S}_+^2 \times \mathbb{S}_-^2, \tag{3.16}$$

where

$$\mathbf{n}_\pm(\phi_\pm, \theta_\pm) = (\cos\phi_\pm \sin\theta_\pm, \sin\phi_\pm \sin\theta_\pm, \cos\theta_\pm), \tag{3.17}$$

are the unit vectors on the two unit spheres $\mathbb{S}_\pm^2$ living in two perpendicular 3-dimensional vector subspaces of $\bigwedge^2(\mathbb{R}^4)$. Since the second arrow in Eq. 3.16 is a bijection, we write the representative of each coset $[R]$ as $R(\mathbf{n}_+, \mathbf{n}_-)$, and the Euler Hamiltonian is readily given by

$$\widetilde{H}_E[\mathbf{n}_+, \mathbf{n}_-] = R(\mathbf{n}_+, \mathbf{n}_-) \cdot \begin{pmatrix} -\epsilon \mathbb{1} & \\ & \epsilon \mathbb{1} \end{pmatrix} \cdot R(\mathbf{n}_+, \mathbf{n}_-)^T. \tag{3.18}$$

See the Mathematica code of Ref. (Bouhon, 2020) for the explicit expression of $R(\mathbf{n}_+, \mathbf{n}_-)$ as a function of the four spherical angles $(\phi_+, \theta_+, \phi_-, \theta_-)$. Defining

$$\begin{aligned} \mathbf{n} &= \mathbf{n}_+(\phi_+, \theta_+), \\ \mathbf{n}' &= \mathbf{n}_-(\phi_- + \pi/2, \theta_- + \pi/2), \end{aligned} \tag{3.19}$$

and writing the components $\mathbf{n}^{(\prime)} = (n_1^{(\prime)}, n_2^{(\prime)}, n_3^{(\prime)})$, the Euler Hamiltonian is then (Bouhon *et al.*, 2020b, Bouhon, 2020)

$$\begin{aligned} \widetilde{H}_E[\mathbf{n}, \mathbf{n}'] = {} & n_1'(-n_1\Gamma_{zz} + n_2\Gamma_{zx} + n_3\Gamma_{x0}) \\ & - n_2'(+n_1\Gamma_{xz} - n_2\Gamma_{xx} + n_3\Gamma_{z0}) \\ & + n_3'(+n_1\Gamma_{0x} + n_2\Gamma_{0z} - n_3\Gamma_{yy}) \quad , \end{aligned} \tag{3.20}$$

with $\Gamma_{ij} = \sigma_i \otimes \sigma_j$ and the Pauli matrices $\{\sigma_i\}_{i=x,y,z}$, and with $\sigma_0 = \mathbb{1}$.

Homotopy classification

Considering the unit vector $\mathbf{n}$ as a mapping from a base sphere $\mathbb{S}^2_0$ to a target sphere $\mathbb{S}^2$, *i.e.* $\mathbf{n} = \mathbf{n}(\phi(\phi_0, \theta_0), \theta(\phi_0, \theta_0))$, we define the skyrmion number

$$W[\mathbf{n}] = \frac{1}{4\pi} \int_{\mathbb{S}^2_0} d\phi_0 d\theta_0 \, \mathbf{n} \cdot (\partial_{\phi_0}\mathbf{n} \times \partial_{\theta_0}\mathbf{n}) \in \mathbb{Z}, \tag{3.21}$$

that counts the number of times $\mathbf{n}$ wraps the target sphere $\mathbb{S}^2$ as we cover the base sphere $\mathbb{S}^2_0$ one time. By setting

$$\begin{aligned} \mathbf{n}_q &= (\cos(q\phi_0)\sin\theta_0, \sin(q\phi_0)\sin\theta_0, \cos\theta_0), \\ \mathbf{n}'_{q'} &= (\cos(q'\phi_0)\sin\theta_0, \sin(q'\phi_0)\sin\theta_0, \cos\theta_0), \end{aligned} \tag{3.22}$$

we readily obtain

$$W[\mathbf{n}_q] = q, \text{ and } W[\mathbf{n}'_{q'}] = q', \tag{3.23}$$

in terms of which the homotopy classification of $\widetilde{H}[\mathbf{n}_q, \mathbf{n}'_{q'}]$ in Eq. 3.20 is defined, since

$$\begin{aligned} \pi_2[\widetilde{\mathrm{Gr}}^{\mathbb{R}}_{2,4}] &= \pi_2[\mathbb{S}^2 \times \mathbb{S}^2] = \pi_2[\mathbb{S}^2] \oplus \pi_2[\mathbb{S}^2] \\ &= \mathbb{Z} \oplus \mathbb{Z} \ni (q, q'). \end{aligned} \tag{3.24}$$

3.8.2 Topology of the Bloch Hamiltonian

So far, we have not specified the parameter base space of the Hamiltonian. Considering a two-dimensional crystalline system, we aim at a Bloch Hamiltonian $\widetilde{H}(\mathbf{k})$ parametrized by a momentum vector $\mathbf{k} = (k_1, k_2)$ inside the Brillouin zone $[-\pi, \pi)^2 \cong \mathbb{T}^2$.

Preceding the previous construction by a projection of the Brillouin zone onto the base sphere

$\mathbb{S}_0$, *i.e.*

$$\mathbb{T}^2 \to \mathbb{S}^2_0 \to \mathbb{S}^2 \times \mathbb{S}^{2\prime} : \mathbf{k} \mapsto \mathbf{n}_0(\mathbf{k}) \mapsto (\mathbf{n}_q(\mathbf{k}), \mathbf{n}'_{q'}(\mathbf{k})), \tag{3.25}$$

we obtain an explicit parametrization of the Hamiltonian Eq. 3.20 as a Bloch Hamiltonian for all the homotopy classes, *i.e.*

$$\widetilde{H}_E[\mathbf{n}, \mathbf{n}'] \to \widetilde{H}_E[\mathbf{n}_q(\mathbf{k}), \mathbf{n}'_{q'}(\mathbf{k})]. \tag{3.26}$$

Writing the Euler classes (see Sec. 3.2 and 3.3) of the occupied and unoccupied bands E_I and E_{II}, respectively, we obtain the homotopy classification of the two-dimensional *orientable* (excluding π-Berry phases) four-band Euler insulating phases through

$$E_I = q - q',\ E_{II} = q + q'. \tag{3.27}$$

Importantly, the homotopy classification $\pi_2[\mathsf{Gr}^{\mathbb{R}}_{2,4}] = \pi_2[\widetilde{\mathsf{Gr}}^{\mathbb{R}}_{2,4}] = \pi_2[\mathbb{S}^2 \times \mathbb{S}^2] = \mathbb{Z} \oplus \mathbb{Z}$, assumes the constraint of a fixed base point (by definition of the homotopy groups). However, Bloch Hamiltonians do not fix a base point, which allows the nontrivial action of the generator of the first homotopy group on the second homotopy group (Bouhon *et al.*, 2020b). Writing $\pi_1[\mathsf{Gr}^{\mathbb{R}}_{2,4}] = \mathbb{Z}_2 = \{[x], [\ell]\}$, where $[x]$ is the class of loops that can be shrunk to a point and the generator $[\ell]$ is the class of loops that cannot be shrunk to a point, the action of $[\ell]$ on the second homotopy group is represented by the deformation of a reference point of $\mathsf{Gr}^{\mathbb{R}}_{2,4}$ over a nontrivial loop in $\mathsf{Gr}^{\mathbb{R}}_{2,4}$. This induces the flip of both Euler classes, *i.e.*

$$(E_I, E_{II}) \xrightarrow{[\ell]} (-E_I, -E_{II}), \tag{3.28}$$

leading to a reduction of the classification (Bouhon *et al.*, 2020b)

$$(q, q') \in \mathbb{Z}^2 \longrightarrow (E_I, E_{II}) \in \left\{(a, b) \in \mathbb{Z}^2 | (a, b) \sim (-a, -b)\right\}, \tag{3.29}$$

(this captures the distinction between the topology of *oriented* and *orientable* spaces). Moreover, it can be shown that the homotopy classification of the balanced phases ($|E_I| = |E_{II}|$) is further reduced due to the existence of an adiabatic transformation between the phases $(E_I, E_{II}) = (q, q)$ and $(-q, q)$ (Bouhon and Slager, 2022).

We finally note the sum rule

$$E_I + E_{II} = 0 \bmod 2, \tag{3.30}$$

which guarantees the cancellation of the second Stiefel-Whitney class over all the bands, *i.e.* $w_{2,I} + w_{2,II} = 0 \bmod 2$.

Balanced and imbalanced phases

The above homotopy classification allows us to distinguish two types of phases, the balanced phases with $|E_I| = |E_{II}|$, and the imbalanced phases with $|E_I| \neq |E_{II}|$. The balanced phases are characterized by having one zero skyrmion number, *i.e.* either $q = 0$ or $q' = 0$, while the imbalanced phases are characterized by having two nonzero skyrmion numbers, *i.e.* $|q|, |q'| > 0$.

In Sec. 3.9 and 3.10, we rederive in detail the general form and the topology of the Bloch Hamiltonian for the balanced phases with degenerate bands by starting from a system with spinful basal mirror symmetry. Indeed, we prove in the Sec. 3.10.1 that a balanced Euler insulating phase has degenerate bands if and only if it has spinful basal mirror symmetry.

3.8.3 Tight-binding Hamiltonian

Once the homotopy representative Hamiltonian has been parametrized in terms of the points of the Brillouin zone, as in $\widetilde{H}_E[\mathbf{n}_q(\mathbf{k}), \mathbf{n}'_{q'}(\mathbf{k})]$, we get a tight-binding Bloch Hamiltonian by expanding each term as a Fourier series, *i.e.*

$$\begin{aligned}\left(\widetilde{H}_E[\mathbf{n}_q(\mathbf{k}), \mathbf{n}'_{q'}(\mathbf{k})]\right)_{ab} = \sum_{l_x, l_y \in \mathbb{Z}} \Big[& a^{(ab)}_{(l_x, l_y)} \cos\big(l_x k_x + l_y k_y\big) \\ & + b^{(ab)}_{(l_x, l_y)} \sin\big(l_x k_x + l_y k_y\big)\Big] .\end{aligned} \tag{3.31}$$

In practise, we only need to keep a finite number K of terms, such that $-K \leq l_x, l_y \leq K$, since the hopping parameters $\left\{a^{(ab)}_{(l_x,l_y)}, b^{(ab)}_{(l_x,l_y)}\right\}$ decrease rapidly with the distance $\sqrt{l_x^2 + l_y^2}$.

The explicit tight-binding models used in this work have been retrieved from Ref. (Bouhon, 2020) which provides a Mathematica notebook that generates four-band (and three-band) tight-binding models for arbitrary fixed Euler classes.

Flat-band limit

In our context, perfect flat bands would require to keep all hopping terms up to infinitely distant neighbors (*i.e.* $-\infty \leq l_{x,y} \leq \infty$ in Eq. 3.31). However, we obtain a very good numerical approximation of the flat bands by keeping hopping terms up to $K \approx 12$, see *e.g.* Fig. 3.6(a) and (b).

3.9 From complex to real basis

Usually, the tight-binding models of physical systems with $C_2\mathcal{T}$-symmetry are not given in their real form. In order to fix ideas, let us start from the following Bloch-Löwdin orbital basis, composed of two s-orbitals located at the center of the unit cell, each taken with the two

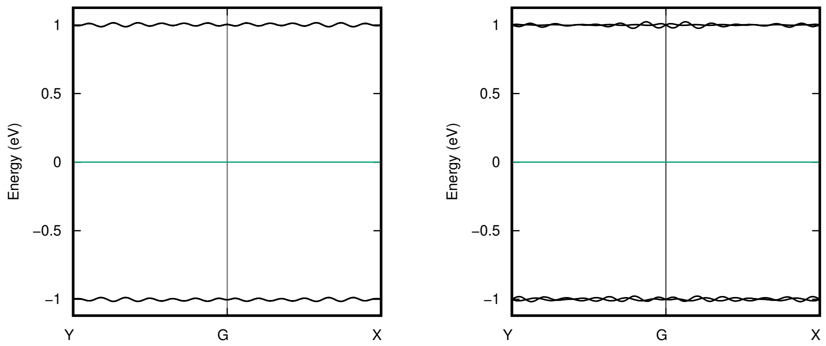

Figure 3.6 – Band structures in the approximate flat-band limit for (a) the balanced phase $(E_I, E_{II}) = (2,2)$, and (b) the imbalanced phase $(E_I, E_I) = (1,3)$, obtained for $K = 12$ in Eq. 3.31.

spin-1/2 components,

$$
\begin{aligned}
|\varphi,\mathbf{k}\rangle &= \big(|\varphi_{1,\uparrow},\mathbf{k}\rangle\;|\varphi_{2,\uparrow},\mathbf{k}\rangle\;|\varphi_{1,\downarrow},\mathbf{k}\rangle\;|\varphi_{2,\downarrow},\mathbf{k}\rangle\big)\,,\\
&= \sum_{\mathbf{R}} \mathrm{e}^{\mathrm{i}\mathbf{k}\cdot\mathbf{R}}\big(|w_{1,\uparrow},\mathbf{R}\rangle\;|w_{2,\uparrow},\mathbf{R}\rangle\;|w_{1,\downarrow},\mathbf{R}\rangle\;|w_{2,\downarrow},\mathbf{R}\rangle\big)\,,
\end{aligned}
\tag{3.32}
$$

where $\mathbf{R}$ runs over all the Bravais vectors of the lattice, and $\langle\mathbf{r}|w_\alpha,\mathbf{R}\rangle = w_\alpha(\mathbf{r}-\mathbf{R})$ is the Wannier function of the orbital α localized at the lattice site $\mathbf{R}$. The Bloch Hamiltonian then reads,

$$
\mathscr{H} = \sum_{\mathbf{k}} |\varphi,\mathbf{k}\rangle H(\mathbf{k}) \langle\varphi,\mathbf{k}|, \tag{3.33}
$$

with

$$
\begin{aligned}
H(\mathbf{k}) &= \begin{pmatrix} H_{\uparrow\uparrow}(\mathbf{k}) & H_{\uparrow\downarrow}(\mathbf{k}) \\ H^{\dagger}_{\uparrow\downarrow}(\mathbf{k}) & H_{\downarrow\downarrow}(\mathbf{k}) \end{pmatrix},\\
&= \begin{pmatrix}
H_{1\uparrow,1\uparrow}(\mathbf{k}) & H_{1\uparrow,2\uparrow}(\mathbf{k}) & H_{1\uparrow,1\downarrow}(\mathbf{k}) & H_{1\uparrow,2\downarrow}(\mathbf{k}) \\
H^{*}_{1\uparrow,2\uparrow}(\mathbf{k}) & H_{2\uparrow,2\uparrow}(\mathbf{k}) & H_{2\uparrow,1\downarrow}(\mathbf{k}) & H_{2\uparrow,2\downarrow}(\mathbf{k}) \\
H^{*}_{1\uparrow,1\downarrow}(\mathbf{k}) & H^{*}_{2\uparrow,1\downarrow}(\mathbf{k}) & H_{1\downarrow,1\downarrow}(\mathbf{k}) & H_{1\downarrow,2\downarrow}(\mathbf{k}) \\
H^{*}_{1\uparrow,2\downarrow}(\mathbf{k}) & H^{*}_{2\uparrow,2\downarrow}(\mathbf{k}) & H^{*}_{1\downarrow,2\downarrow}(\mathbf{k}) & H_{2\downarrow,2\downarrow}(\mathbf{k})
\end{pmatrix},
\end{aligned}
\tag{3.34}
$$

where we have imposed hermiticity.

Let us list the action on the Bloch orbital basis of a few symmetries that we use below,

$$\begin{aligned}
{}^{C_{2z}}|\varphi,\mathbf{k}\rangle &= |\varphi,C_{2z}\mathbf{k}\rangle\,(-\mathrm{i}\sigma_z\otimes\mathbb{1})\,,\\
{}^{I}|\varphi,\mathbf{k}\rangle &= |\varphi,-\mathbf{k}\rangle\,(\mathbb{1}\otimes\mathbb{1})\,,\\
{}^{m_z}|\varphi,\mathbf{k}\rangle &= |\varphi,m_z\mathbf{k}\rangle\,(-\mathrm{i}\sigma_z\otimes\mathbb{1})\,,\\
{}^{\mathcal{T}}|\varphi,\mathbf{k}\rangle &= |\varphi,-\mathbf{k}\rangle\left(-\mathrm{i}\sigma_y\otimes\mathbb{1}\right)\mathcal{K}\,,\\
{}^{C_{2z}\mathcal{T}}|\varphi,\mathbf{k}\rangle &= |\varphi,m_z\mathbf{k}\rangle\,(\mathrm{i}\sigma_x\otimes\mathbb{1})\,\mathcal{K}\,,\\
{}^{I\mathcal{T}}|\varphi,\mathbf{k}\rangle &= |\varphi,\mathbf{k}\rangle\left(-\mathrm{i}\sigma_y\otimes\mathbb{1}\right)\mathcal{K}\,,
\end{aligned} \tag{3.35}$$

where C_{2z} is the π rotation about the $\hat{z}$ axis that is perpendicular to the basal plane containing the two-dimensional system, I is inversion, $m_z = C_{2z}I = IC_{2z}$ is the basal mirror, $\mathcal{T}$ is time reversal, and $\mathcal{K}$ is complex conjugation.

We now consider a system that is symmetric under $C_{2z}\mathcal{T}$ only, *i.e.* it must satisfy the constraint

$$(\sigma_x\otimes\mathbb{1})\,H^*(m_z\mathbf{k})\,(\sigma_x\otimes\mathbb{1}) = H(\mathbf{k}). \tag{3.36}$$

In 2D systems, the momenta belong to the m_z-invariant Brillouin zone, *i.e.* $m_z\mathbf{k} = \mathbf{k}$. As a consequence the blocks $H_{\sigma\sigma'}(\mathbf{k})$ that compose $H(\mathbf{k})$ must be of the form

$$\begin{aligned}
H_{\uparrow\uparrow} &= H_1\sigma_x + H_2\sigma_y + H_3\sigma_z + H_4\mathbb{1},\\
H_{\downarrow\downarrow} &= H_1\sigma_x - H_2\sigma_y + H_3\sigma_z + H_4\mathbb{1},\\
H_{\uparrow\downarrow} &= \begin{pmatrix} H_5+\mathrm{i}H_6 & H_7+\mathrm{i}H_8\\ H_7+\mathrm{i}H_8 & H_9+\mathrm{i}H_{10}\end{pmatrix},
\end{aligned} \tag{3.37}$$

where

$$\begin{array}{lcllcl}
H_1 &=& \mathrm{Re}\,H_{1\uparrow,2\uparrow}, & H_6 &=& \mathrm{Im}\,H_{1\uparrow,1\downarrow},\\
H_2 &=& -\,\mathrm{Im}\,H_{1\uparrow,2\uparrow}, & H_7 &=& \mathrm{Re}\,H_{1\uparrow,2\downarrow},\\
H_3 &=& (H_{1\uparrow,1\uparrow}-H_{2\uparrow,2\uparrow})/2, & H_8 &=& \mathrm{Im}\,H_{1\uparrow,2\downarrow},\\
H_4 &=& (H_{1\uparrow,1\uparrow}+H_{2\uparrow,2\uparrow})/2, & H_9 &=& \mathrm{Re}\,H_{2\uparrow,2\downarrow},\\
H_5 &=& \mathrm{Re}\,H_{1\uparrow,1\downarrow}, & H_{10} &=& \mathrm{Im}\,H_{2\uparrow,2\downarrow},
\end{array} \tag{3.38}$$

From $[C_{2z}\mathcal{T}]^2 = +1$ follows that there exists a basis in which $C_{2z}\mathcal{T}$ is represented by $\mathcal{K}$ (Bouhon *et al.*, 2020a). This basis is here given by

$$\begin{aligned}
|\widetilde{\varphi},\mathbf{k}\rangle &= |\varphi,\mathbf{k}\rangle\cdot V^\dagger,\\
V &= \sqrt{\sigma_x\otimes\mathbb{1}}\cdot\frac{1}{2}\begin{pmatrix} -1 & \mathrm{i} & 1 & -\mathrm{i}\\ \mathrm{i} & -1 & \mathrm{i} & -1\\ -\mathrm{i} & 1 & \mathrm{i} & -1\\ -1 & \mathrm{i} & -1 & \mathrm{i}\end{pmatrix},
\end{aligned} \tag{3.39}$$

for which

$$\begin{aligned} {}^{C_{2z}\mathcal{T}}|\widetilde{\varphi},\mathbf{k}\rangle &= {}^{C_{2z}\mathcal{T}}|\varphi,\mathbf{k}\rangle \cdot V^{\dagger}, \\ &= |\varphi,\mathbf{k}\rangle \cdot (\mathrm{i}\sigma_x \otimes \mathbb{1})\, V^{T}\mathcal{K}, \\ &= |\widetilde{\varphi},\mathbf{k}\rangle \cdot V\, (\mathrm{i}\sigma_x \otimes \mathbb{1})\, V^{T}\mathcal{K}, \\ &= |\widetilde{\varphi},\mathbf{k}\rangle\mathcal{K}. \end{aligned} \tag{3.40}$$

Rotating the Hamiltonian in the new basis, we define

$$\widetilde{H}(\mathbf{k}) = V \cdot H(\mathbf{k}) \cdot V^{\dagger}, \tag{3.41}$$

that now must satisfy $\widetilde{H}^{*}(\mathbf{k}) = \widetilde{H}(\mathbf{k})$ as a consequence of $C_{2z}\mathcal{T}$ symmetry, *i.e.* $\widetilde{H}(\mathbf{k})$ is real and symmetric.

In the “real” basis, the Hamiltonian thus has the generic form

$$\widetilde{H} = \begin{pmatrix} h_{11} & h_{12} & h_{13} & h_{14} \\ h_{12} & h_{22} & h_{23} & h_{24} \\ h_{13} & h_{23} & h_{33} & h_{34} \\ h_{14} & h_{24} & h_{34} & h_{44} \end{pmatrix}, \tag{3.42}$$

where all elements h_{ij} are real and given by

$$\begin{array}{rcl} h_{11} & = & H_3 + H_4 - H_5, \\ h_{22} & = & H_3 + H_4 + H_5, \\ h_{33} & = & -H_3 + H_4 - H_9, \\ h_{44} & = & -H_3 + H_4 + H_9, \\ h_{12} & = & -H_6, \\ h_{13} & = & -H_1 + H_7, \\ h_{14} & = & H_2 - H_8, \\ h_{23} & = & H_2 + H_8, \\ h_{24} & = & H_1 + H_7, \\ h_{34} & = & H_{10}. \end{array} \tag{3.43}$$

3.10 Mirror Chern number and Euler class

Let us assume that the system satisfies the basal mirror symmetry m_z as well. Then, it must also have $-m_z C_{2z}\mathcal{T} = -C_{2z}^{2} I\mathcal{T} = I\mathcal{T}$ symmetry. The system thus has the symmetries of the magnetic point group $2'/m = \{E, C_{2z}\mathcal{T}, m_z, I\mathcal{T}\}$. It readily follows that the off-diagonal blocks $H_{\uparrow\downarrow} = H_{\downarrow\uparrow}$ must vanish, *i.e.* $H_5 = H_6 = H_7 = H_8 = H_9 = H_{10} = 0$. The m_z-invariant Hamiltonian in the spinor basis then reads

$$H = H_{\uparrow\uparrow} \oplus H_{\downarrow\downarrow}. \tag{3.44}$$

Since ${}^{I\mathcal{T}}\mathcal{H} = \mathcal{H}$ with $[I\mathcal{T}]^2 = -1$, the bands must be twofold-degenerate at all momenta, namely the bands are Kramers degenerate. The eigenvalues are indeed readily found to be

$\{E_o, E_o, E_u, E_u\}$, with

$$\begin{aligned} &E_o = H_4 - \epsilon,\ E_u = H_4 + \epsilon, \\ &\epsilon = \sqrt{H_1^2 + H_2^2 + H_3^2}. \end{aligned} \tag{3.45}$$

We note that H_4 can be chosen arbitrarily without affecting the symmetry and the topology, we thus set $H_4 = 0$ without loss of generality. The eigenvectors are

$$\begin{aligned} v_o^{(\uparrow)} &= \begin{pmatrix} \sqrt{1-r^2} \\ -r\,\mathrm{e}^{\mathrm{i}\rho} \\ 0 \\ 0 \end{pmatrix}, v_u^{(\uparrow)} = \begin{pmatrix} r \\ \sqrt{1-r^2}\,\mathrm{e}^{\mathrm{i}\rho} \\ 0 \\ 0 \end{pmatrix}, \\ v_o^{(\downarrow)} &= \begin{pmatrix} 0 \\ 0 \\ \sqrt{1-r^2} \\ -r\,\mathrm{e}^{-\mathrm{i}\rho} \end{pmatrix}, v_u^{(\downarrow)} = \begin{pmatrix} 0 \\ 0 \\ r \\ \sqrt{1-r^2}\,\mathrm{e}^{-\mathrm{i}\rho} \end{pmatrix}, \end{aligned} \tag{3.46}$$

with

$$\rho = \mathrm{Arg}\{H_1 + iH_2\}, \quad r^2 = \frac{\epsilon + H_3}{2\epsilon}. \tag{3.47}$$

The topology can now be directly assessed from a single spin sector, say from $H_{\uparrow\uparrow}$. Imposing the condition of a band gap, *i.e.* $\epsilon > 0$, we define the unit vector

$$\mathbf{n}_\uparrow = \frac{1}{\epsilon}(H_1, H_2, H_3), \tag{3.48}$$

in terms of which we obtain the skyrmion number $W[\mathbf{n}_\uparrow]$ Eq. 3.21. Characterizing the $H_{\downarrow\downarrow}$ with the unit vector

$$\mathbf{n}_\downarrow = \frac{1}{\epsilon}(H_1, -H_2, H_3), \tag{3.49}$$

we have

$$W[\mathbf{n}_\downarrow] = -W[\mathbf{n}_\uparrow]. \tag{3.50}$$

It can be checked that $W[\mathbf{n}_\uparrow]$ directly gives the Chern number computed through the surface integral of the Berry curvature for the occupied eigenvector in the $\uparrow$-spin sector, *i.e.* defining

$$\begin{aligned} F[v_o^{(\uparrow)}] = -\mathrm{i}\Big[&(\partial_{k_1} v_o^{(\uparrow)})^\dagger \cdot (\partial_{k_2} v_o^{(\uparrow)}) \\ &-(\partial_{k_2} v_o^{(\uparrow)})^\dagger \cdot (\partial_{k_1} v_0^{(\uparrow)})\Big], \end{aligned} \tag{3.51}$$

we have

$$C^{(\uparrow)} = \frac{1}{2\pi}\int d^2\mathbf{k}\, F[v_o^{(\uparrow)}] = W[\mathbf{n}_\uparrow], \tag{3.52}$$

and similarly

$$C^{(\downarrow)} = \frac{1}{2\pi}\int d^2\mathbf{k}\, F[v_o^{(\downarrow)}] = W[\mathbf{n}_\downarrow] = -C^{(\uparrow)}. \tag{3.53}$$

Furthermore, since the m_z operator is diagonal in the orbital-spinor basis (see Eq. 3.35), we readily find the Chern number in the (−i)-mirror eigenvalue sector, *i.e.*

$$C^{(-\mathrm{i})} = C^{(\uparrow)} = W[\mathbf{n}_\uparrow], \tag{3.54}$$

called the mirror Chern number. Similarly, the mirror Chern number of the other spin (mirror) sector is

$$C^{(\mathrm{i})} = C^{(\downarrow)} = W[\mathbf{n}_\downarrow] = -W[\mathbf{n}_\uparrow]. \tag{3.55}$$

Moving to the real basis, we now show that there is a one-to-one correspondence between the mirror Chern number of one occupied mirror-polarized band and the signed Euler class of the occupied two-band subspace. First, let us write the m_z-invariant Hamiltonian in its real symmetric form,

$$\begin{aligned}\widetilde{H} &= \begin{pmatrix} H_3 & 0 & -H_1 & H_2 \\ 0 & H_3 & H_2 & H_1 \\ -H_1 & H_2 & -H_3 & 0 \\ H_2 & H_1 & 0 & -H_3 \end{pmatrix}, \\ &= -H_1(\sigma_x \otimes \sigma_z) + H_2(\sigma_x \otimes \sigma_x) + H_3(\sigma_z \otimes \mathbb{1}).\end{aligned} \tag{3.56}$$

Assuming again the gap condition, *i.e.* $\epsilon^2 = H_1^2 + H_2^2 + H_3^2 > 0$, without loss of generality we can deform the Hamiltonian as $H_i \to n_{\uparrow,i}$ for $i = 1,2,3$.

We now derive the direct relation between the mirror Chern number and the Euler class of the system via the Plücker embedding. First, we parametrize the flattened Hamiltonian Eq. 3.56 through

$$\begin{aligned} H_1/\epsilon &= n_{\uparrow,1} = \cos\phi \sin\theta, \\ H_2/\epsilon &= n_{\uparrow,2} = \sin\phi \sin\theta, \\ H_3/\epsilon &= n_{\uparrow,3} = \cos\theta. \end{aligned} \tag{3.57}$$

The eigenvalues are then $\{-1,-1,1,1\}$, and the two real eigenvectors of the occupied bands are given by

$$\begin{aligned} u_1(\phi,\theta) &= \sqrt{\cos(\theta/2)^2} \begin{pmatrix} \sin\phi\tan(\theta/2) \\ \cos\phi\tan(\theta/2) \\ 0 \\ -1 \end{pmatrix}, \\ u_2(\phi,\theta) &= \sqrt{\cos(\theta/2)^2} \begin{pmatrix} -\cos\phi\tan(\theta/2) \\ \sin\phi\tan(\theta/2) \\ -1 \\ 0 \end{pmatrix}. \end{aligned} \tag{3.58}$$

Then, the wedge product of the two occupied bands (Plücker embedding (Bouhon *et al.*, 2020b)) gives

$$\begin{pmatrix} u_1^3 u_2^2 - u_1^2 u_2^3 \\ u_1^3 u_2^1 - u_1^1 u_2^3 \\ u_1^1 u_2^2 - u_1^2 u_2^1 \\ u_1^4 u_2^1 - u_1^1 u_2^4 \\ u_1^2 u_2^4 - u_1^4 u_2^2 \\ u_1^3 u_2^4 - u_1^4 u_2^3 \end{pmatrix} \cdot \begin{pmatrix} \mathbb{1}_3 & \mathbb{1}_3 \\ \mathbb{1}_3 & -\mathbb{1}_3 \end{pmatrix} = \begin{pmatrix} \cos\phi\sin\theta \\ \sin\phi\sin\theta \\ -\cos\theta \\ 0 \\ 0 \\ 1 \end{pmatrix} \tag{3.59}$$

$$= \left(n_{1,\uparrow}, n_{2,\uparrow}, -n_{3,\uparrow}, 0, 0, 1\right)^T .$$

The Euler class is defined as the winding of the wedge product. The above relation thus explicitly shows that the Euler class of the two occupied bands is readily given by the (oriented) number of times $\mathbf{n}_\uparrow(\phi(k_x,k_y),\theta(k_x,k_y))$ wraps the sphere when (k_x,k_y) covers the Brillouin zone one time (Bouhon *et al.*, 2020b). The proof is completed by noting that the Hamiltonian Eq. 3.56, after flattening the eigenvalues, is defined in terms of Eq. 3.20 by

$$\widetilde{H}[H_i \to n_{\uparrow,i}] = \widetilde{H}_E[(n_{\uparrow,1}, n_{\uparrow,2}, -n_{\uparrow,3}), (0,1,0)]. \tag{3.60}$$

The Euler class of the system are then determined from the Skyrmion numbers

$$\begin{aligned} q &= W[(n_{\uparrow,1}, n_{\uparrow,2}, -n_{\uparrow,3})] = -W[\mathbf{n}_\uparrow], \\ q' &= 0, \end{aligned} \tag{3.61}$$

via Eq. 3.27, to be $(E_I, E_{II}) = (q,q)$. Then with Eq. 3.54, we obtain

$$E_I = E_{II} = -C^{(-\mathrm{i})} \in \mathbb{Z}. \tag{3.62}$$

A few comments are needed here. In general (*i.e.* without mirror symmetry), the sign of the Euler class is not uniquely defined because, as noted above, Hamiltonians only define *orientable* vector bundles (instead of *oriented* vector bundles) as a consequence of the gauge freedom $u_i \to \pm u_i$ for every eigenvector, which allows flipping the sign of the wedge product between the two occupied eigenvectors, *i.e.* $u_1 \wedge u_2 \to -u_1 \wedge u_2$. This has the consequence that there exist adiabatic transformations of the Hamiltonian that flip the sign of the pair of Euler classes, leading to the topological equivalence $(E_I, E_{II}) \sim (-E_I, -E_{II})$ (Bouhon *et al.*, 2020b). Under the constraint of the basal mirror symmetry m_z though, one can associate a signed winding number to a fixed mirror eigenvalue sector.

Let us write the representation of m_z in the basis of real eigenvectors, *i.e.*

$$\begin{pmatrix} u_1^T \\ u_2^T \end{pmatrix} \cdot \widetilde{U}_{m_z} \cdot (u_1 \; u_2) = \begin{pmatrix} 0 & 1 \\ -1 & 0 \end{pmatrix}, \tag{3.63}$$

where

$$\widetilde{U}_{m_z} = V^\dagger \cdot (-\mathrm{i}\sigma_z \otimes \mathbb{1}) \cdot V = \sigma_z \otimes \mathrm{i}\sigma_y \tag{3.64}$$

is the representation of m_z in the "real" Bloch orbital basis Eq. 3.39. The eigenbasis of m_z is thus given through the complexification (see the Chern basis in Sec. 3.2)

$$\begin{aligned} v_+ &= (u_1 + \mathrm{i} u_2)\sqrt{2}, \\ v_- &= (u_1 - \mathrm{i} u_2)/\sqrt{2}, \end{aligned} \tag{3.65}$$

i.e.

$$\begin{pmatrix} v_+^\dagger \\ v_-^\dagger \end{pmatrix} \cdot \widetilde{U}_{m_z} \cdot (v_+ \; v_-) = \begin{pmatrix} -\mathrm{i} & 0 \\ 0 & \mathrm{i} \end{pmatrix} = -\mathrm{i}\sigma_z, \tag{3.66}$$

which is now diagonal, such that $v_\pm$ are eigenvectors of m_z with the eigenvalues $\mp\mathrm{i}$. (Note that we actually recover the action of m_z on the spinor basis given in Eq. 3.35.) It is now transparent from Eq. 3.66 that the relative sign between u_1 and u_2, and thus the sign of the Euler class (fixed by the wedge product $u_1 \wedge u_2$), is fixed by the mirror symmetry, since the gauge transformation $u_1 \wedge u_2 \to -u_1 \wedge u_2$ implies $v_\pm \to v_\mp$ which is forbidden under the constraint of a fixed mirror-eigenvalue sector. Note that the gauge transformation $(u_1, u_2) \to (-u_1, -u_2)$ is allowed since it doesn't change the fixed mirror-eigenvalue sector, nor does it change the signed Euler class.

We emphasise that $\{v_1, v_2\}$ are still eigenvectors of the Hamiltonian since the energy eigenvalues for u_1 and u_2 are degenerate. Furthermore, we readily recover the $(-\mathrm{i})$- and (i)-mirror Chern numbers as the Chern numbers of v_1 and v_2, respectively. It is now apparent that the winding associated to a nontrivial Euler class in Eq. 3.59, directly implies the winding associated to the mirror Chern numbers, according to Eq. 3.54. We conclude that by imposing that $u_1 + \mathrm{i}u_2$ has the mirror eigenvalue $-\mathrm{i}$, there is a one-to-one correspondence between the Euler class Eq. 3.59 and the mirror Chern number Eq. 3.54, leading to Eq. 3.62.

3.10.1 All degenerate balanced phases are mirror-symmetric

Importantly, the above reasoning for balanced Euler insulating phases can be reversed. Namely, for every (orientable) balanced ($E_I = E_{II}$) topological phase with only the $C_{2z}\mathscr{T}$ symmetry, whenever we impose the two-by-two degeneracy of the bands, there must be an effective basal mirror symmetry m_z (spinful with $m_z^2 = -1$), leading to the effective $I\mathscr{T}$ symmetry with $[I\mathscr{T}]^2 = -1$. In other words, the degeneracy of the bands is always associated with a symmetry of the Hamiltonian and no fine-tuning is needed.

We prove this by going back to the general geometric form from which all our tight-binding Hamiltonian are derived, Eq. 3.20. First of all, all Hamiltonian belonging to $\mathrm{Gr}_{2,4}^{\mathbb{R}}$ can be adiabatically mapped to a twofold-degenerate Hamiltonian. By construction the representative of each (orientable) homotopy class $\widetilde{H}[\mathbf{n}, \mathbf{n}']$ is twofold degenerate. Without loss of generality, the balanced phases are obtained by fixing $\mathbf{n}'$ to be non-winding, *i.e.* $q' = W[\mathbf{n}'] = 0$. Note that we can alternatively fix $\mathbf{n}$ to a constant and let $\mathbf{n}'$ wind instead, *i.e.* the transformation $(q, q' = 0) \to (0, q' = q)$, which induces the flip of one Euler class. That is from Eq. 3.27

$$(E_I, E_{II}) \longrightarrow (E_I', E_{II}') = (-E_I, E_{II}). \tag{3.67}$$

Since we do not observe any qualitative difference in the Hofstadter spectrum between the phases (E_I, E_{II}) and $\pm(-E_I, E_{II})$, we have shown results for $E_I, E_{II} \geq 0$ only.

Let us fix $\mathbf{n} = (H_1, H_2, -H_3)/\epsilon$ and $\mathbf{n}' = \bar{\mathbf{n}} = (0,1,0)$ in Eq. 3.20, which leads to the Hamiltonian Eq. 3.56. We find that it is mirror symmetric with

$$\widetilde{U}_{m_z} \cdot \widetilde{H}[\mathbf{n},\bar{\mathbf{n}}] \cdot \widetilde{U}_{m_z}^T = \widetilde{H}[\mathbf{n},\bar{\mathbf{n}}], \tag{3.68}$$

where $\widetilde{U}_{m_z}$ is defined in Eq. 3.64. Comparing $\widetilde{H}[\mathbf{n},\mathbf{n}']$ with two different fixed unit vectors $\mathbf{n}'$, *i.e.* in one case $\mathbf{n}' = \bar{\mathbf{n}}$ and in the other case $\mathbf{n}' = \mathbf{n}_1 \neq \bar{\mathbf{n}}$, we find

$$\widetilde{H}[\mathbf{n},\bar{\mathbf{n}}] = \Delta R[\mathbf{n},\bar{\mathbf{n}},\mathbf{n}_1] \cdot \widetilde{H}[\mathbf{n},\mathbf{n}_1] \cdot \Delta R[\mathbf{n},\bar{\mathbf{n}},\mathbf{n}_1]^T, \tag{3.69}$$

with

$$\Delta R[\mathbf{n},\bar{\mathbf{n}},\mathbf{n}_1] = R[\mathbf{n},\bar{\mathbf{n}}] \cdot R[\mathbf{n},\mathbf{n}_1]^T. \tag{3.70}$$

Substituting Eq. 3.69 in Eq. 3.68, we then obtain

$$\Delta\widetilde{U}_{m_z}(\mathbf{n}_1) \cdot \widetilde{H}[\mathbf{n},\mathbf{n}_1] \cdot \Delta\widetilde{U}_{m_z}(\mathbf{n}_1)^T = \widetilde{H}[\mathbf{n},\mathbf{n}_1], \tag{3.71}$$

with

$$\Delta\widetilde{U}_{m_z}(\mathbf{n}_1) = \Delta R[\mathbf{n},\bar{\mathbf{n}},\mathbf{n}_1]^T \cdot \widetilde{U}_{m_z} \cdot \Delta R[\mathbf{n},\bar{\mathbf{n}},\mathbf{n}_1], \tag{3.72}$$

i.e. the deformed Hamiltonian $\widetilde{H}[\mathbf{n},\bar{\mathbf{n}}] \to \widetilde{H}[\mathbf{n},\mathbf{n}_1]$ is still mirror symmetric, with a constant mirror operator $\Delta\widetilde{U}_{m_z}(\mathbf{n}_1)$.

Interestingly, we can consider more general adiabatic transformations for which $\mathbf{n}'$ is non-constant but still non-winding, *i.e.* $\mathbf{n}' = \mathbf{n}'(\mathbf{k})$ with $W[\mathbf{n}'(\mathbf{k})] = 0$. In that case, the "mirror" symmetry operator is non-constant, with a nontrivial action of the "mirror" symmetry on the momentum. We will explore such phases elsewhere.

Since our homotopy representative Hamiltonian of the balanced Euler insulating phases covers all the balanced homotopy classes (with $q' = 0$ and $q \in \mathbb{Z}$), we conclude with the following statement: *Every (two-dimensional, four-band at half-filling, orientable) balanced Euler insulating phase is (spinful) mirror-symmetric with respect to the basal plane if and only if the energy eigenvalues are twofold-degenerate.*

3.10.2 Degenerate imbalanced phases

Contrary to the balanced case, the imbalanced Euler insulating phases ($|E_I| \neq |E_{II}|$) with twofold-degenerate energy eigenvalues are never compatible with an effective mirror symmetry m_z, and thus there is no Kramers degeneracy. As a consequence, the degeneracy of the bands for these phases always requires fine-tuning.

Let us prove this. The imbalanced condition imposes that $q, q' \neq 0$, *i.e.* the two-unit vectors

$\mathbf{n}$ and $\mathbf{n}'$ both wind. We simply define the imbalanced Hamiltonian from the balanced one through Eq. 3.69, where we substitute the constant unit vector $\mathbf{n}_1$ to the winding one $\mathbf{n}'$. As a consequence, the degenerate imbalanced Hamiltonian satisfies Eq. 3.71 but now with a mirror symmetry operator $\Delta\widetilde{U}_{m_z}(\mathbf{n}')$ in Eq. 3.72 that winds. Therefore, the condition Eq. 3.71 cannot be interpreted as the symmetry of one fixed homotopy class. Since the degeneracy of the bands in one imbalanced homotopy class is never associated with a global symmetry of the Hamiltonian, it is accidental and can only be realized through fine-tuning.

It can be verified with the Mathematica notebook of Ref. (Bouhon, 2020) that the degeneracy of the bands of imbalanced phases is never exact whenever we truncate the Fourier expansion of Eq. 3.31. However, since the hopping parameters decay rapidly, similarly to the flat-band limit, we obtain degenerate bands in a good numerical approximation, see *e.g.* Fig. 3.6(b) showing the band structure of the phase $(E_I, E_{II}) = (1,3)$ obtained for $K = 12$ where both degeneracy and flatness have been imposed.

3.11 Hidden symmetry of the dispersive balanced phases and comparison with the QHS model

The non-degenerate phases break the mirror symmetry m_z. The constraint of the $C_{2z}\mathcal{T}$ symmetry alone allows all the terms of the real symmetric Hamiltonian in Eq. 3.42 to be nonzero. Form the systematic probe of all allowed (adiabatic) perturbations of the model $\widetilde{H}_{\text{bal}}[\mathbf{n}] = \widetilde{H}[\mathbf{n},(0,1,0)]$ given by Eq. 3.20 (see also Sec. 3.3), we have found that the gapping of the Hofstadter spectrum at half-filling only happens when $h_{14} \neq h_{23}$. Setting $h_{23} = h + \delta$ and $h_{14} = h - \delta$, a general (real symmetric) balanced Hamiltonian then takes the form

$$\widetilde{H}_{\text{bal}} = \widetilde{H}_{\text{bal}}[\delta = 0] + \delta(\sigma_y \otimes \sigma_y), \tag{3.73}$$

with $\delta = (h_{23} - h_{14})/2$.

We call the condition $\delta = 0$ a hidden symmetry of the balanced Hamiltonian at finite flux. In other words, every tight-binding Hamiltonian that is of the form $\widetilde{H}_{\text{bal}}[\delta = 0]$ satisfies the hidden symmetry and exhibits a gapless Hofstadter spectrum. On the contrary, any model with $|\delta| > 0$ has a gapped Hofstadter spectrum.

Comparison with the QSH model

In Ref. (Herzog-Arbeitman *et al.*, 2020) the authors have considered the BHZ model of the Quantum Spin Hall phase (QSH) and its generalization when only the $C_{2z}\mathcal{T}$ symmetry is preserved and restricting to balanced phases, which they call H'''_{QSH}. For exhaustiveness, we give here the mapping from H'''_{QSH} (which is not in its real form) to our models in Eq. 3.42.

We first write H'''_{QSH} in its generic form, *i.e.*

$$H'''_{QSH} = a_0(\mathbb{1}\otimes\mathbb{1}) + a_1(\mathbb{1}\otimes\sigma_z) + a_2(\sigma_z\otimes\sigma_x) + \tag{3.74}$$

$$a_3(\sigma_z\otimes\sigma_x) + a_4(\sigma_y\otimes\sigma_z) + a_5(\sigma_x\otimes\mathbb{1}) + a'_5(\sigma_y\otimes\mathbb{1}) + \tag{3.75}$$

$$a_6(\sigma_x\otimes\sigma_y) + a'_6(\sigma_y\otimes\sigma_y) + a''_6(\sigma_x\otimes\sigma_z), \tag{3.76}$$

where we have added the term $a_4(\sigma_y\otimes\sigma_z)$ which is allowed by $C_{2z}\mathcal{T}$ but not present in the model of Ref. (Herzog-Arbeitman *et al.*, 2020). (We note that we are not concerned here with the specific expressions of the terms of H'''_{QSH} given in Ref. (Herzog-Arbeitman *et al.*, 2020) which realizes the phase $E_I = E_{II} = 1$.)

We now perform a change of basis that brings H'''_{QSH} in its real form in order to compare it with our models. We define

$$\widetilde{H}'''_{QSH} = P\cdot V\cdot H'''_{QSH}\cdot V^\dagger\cdot P, \tag{3.77}$$

that is real and symmetric, with

$$V = \sqrt{\sigma_x\otimes\sigma_z}, \quad P = \begin{pmatrix} 1 & 0 & 0 & 0\\ 0 & 0 & 1 & 0\\ 0 & 1 & 0 & 0\\ 0 & 0 & 0 & 1\end{pmatrix}. \tag{3.78}$$

Writing it explicitly, we have

$$\widetilde{H}'''_{QSH} = \begin{pmatrix} h_{11} & h_{12} & h_{13} & h_{14}\\ h_{12} & h_{22} & h_{23} & h_{24}\\ h_{13} & h_{23} & h_{33} & h_{34}\\ h_{14} & h_{24} & h_{34} & h_{44}\end{pmatrix}, \tag{3.79}$$

with

$$\begin{aligned}
h_{11} &= a_0 + a_1 + a_4 + a'_5\\
h_{22} &= a_0 + a_1 - a_4 - a'_5\\
h_{33} &= a_0 - a_1 + a_4 - a'_5\\
h_{44} &= a_0 - a_1 - a_4 + a'_5\\
h_{12} &= a_5 + a''_6\\
h_{13} &= a_2 - a_6\\
h_{14} &= -a_3 - a'_6\\
h_{23} &= -a_3 + a'_6,\\
h_{24} &= -a_2 - a_6,\\
h_{34} &= a_5 - a''_6.
\end{aligned} \tag{3.80}$$

In agreement with our finding of the hidden symmetry, we have verified that only the nonzero term $a'_6(\sigma_y \otimes \sigma_y)$ of H'''_{QSH} leads to the gapping of the Hofstadter spectrum. We indeed have

$$a'_6 = \frac{h_{23} - h_{14}}{2} = \delta, \tag{3.81}$$

which is the term responsible for the hidden symmetry discussed above.

4 Bulk-boundary correspondence of imbalanced topological Euler insulators

Topological materials feature nontrivial boundary modes, which originated from bulk topology. Characteristics of two-dimensional systems with $C_2\mathcal{T}$ symmetry fall into the Euler classes, while its boundary signature is still being investigated. Euler insulators differ from other topological insulators in their qualities. In particular, the Euler numbers of occupied and empty bands do not have to be equal, thus allowing the scenario of imbalanced Euler insulators. Edge state crossing indexes in flat-band Euler insulators are reported in this Chapter. The edge mode features a series of touching points within the limit of exact dispersionless bulk bands. The algebraic order of the dispersion branches forming the edge nodal points sums up to the bulk Euler number, according to a comprehensive inspection of the edge states. Such a summing rule provides bulk-boundary correspondence of an Euler insulator, as well as the observable to identify balanced and imbalanced Euler insulators.

The motivation of this Chapter is to explore edge signatures for the Euler class topology and provide a direct comparison against the edge states of Chern insulators.

The Chapter is adapted from:
Y.Guan, A.Bouhon, O.Yazyev
Edge signatures of imbalanced Euler insulators;

My contribution includes: performing the edge state calculations, concluding the relationship between algebraic orders and the Euler numbers and providing the Wilson loop theory for edge states.

4.1 Introduction

Bulk-boundary correspondence (BBC) has been the hallmark of topological phases in solids (Hatsugai, 1993, Thouless, 1998, Fidkowski *et al.*, 2011). Such a correspondence provides a prominent probe of bulk topology, and the topologically protected states give the possibility to design robust surface modes (Hatsugai, 1993, Xu *et al.*, 2021, Chiu *et al.*, 2018). Since the discovery of edge states in Chern insulators and quantum spin Hall insulators, a series of studies has expanded the scope of bulk-boundary correspondence to broader ranges of topological insulators (Qi and Zhang, 2011, Hasan and Kane, 2010, Takahashi *et al.*, 2020, Hwang *et al.*, 2019, Trifunovic and Brouwer, 2019, Rhim *et al.*, 2018).

While the connection between the edge spectrum and the bulk topology is established for various types of insulators (Alexandradinata *et al.*, 2016, Fidkowski *et al.*, 2011), inferring edge states from solely bulk invariants remains problematic. There are two dimensions to the difficulty of such a situation. First, the present theories rely on the condition that the edge preserves all bulk symmetries (Alexandradinata *et al.*, 2016), which can be violated in reality. Moreover, the correspondence faces challenges in fragile topological insulators found recently, where the bulk topology might be trivialized by adding trivial bands into the occupied subspace. (Song *et al.*, 2020a, Po *et al.*, 2018a, Song *et al.*, 2020b, Bouhon *et al.*, 2019, 2020b). The concept of fragile topological insulators rises from the discrepancy between the stable classification (Schnyder *et al.*, 2008, Kitaev, 2009, Chiu *et al.*, 2016) and symmetry indicators (Bradlyn *et al.*, 2019, 2017). The notion of fragile topology then brings the study on topological details of subbands (Bouhon *et al.*, 2020b). Such fragile indicators are sensitive to the number of bands, which is different from the previous stable phases. Among the intriguing classes of fragile topological insulators, the crystalline fragile phases have been reported to exhibit twisted BBC (Song *et al.*, 2020b). Such a scenario is verified by taking adiabatic pumps while preserving the symmetries (Song *et al.*, 2020b, Peri *et al.*, 2020). However, the BBC for broader classes of fragile topological insulators has not been fully established.

Typically, the fragile topology appearing in $\mathscr{PT}$ or $C_2\mathscr{T}$ symmetric systems goes beyond solely symmetry indicators (Ahn *et al.*, 2019a, 2018, Bouhon *et al.*, 2020a, Wu *et al.*, 2019, Ahn *et al.*, 2019b, Ahn and Yang, 2019). These systems are characterized by geometrical invariants called Euler numbers. Such fragile characteristics also feature a special subclass of the "imbalanced" Euler class, where the Euler numbers of occupied and empty bands are different (Bouhon and Slager, 2022). The imbalanced topological charges are usually absent in conventional classifications.

Euler-class insulators are also related to rich kinds of physical phenomena. Their manifestation on observables includes the non-Abelian braiding of nodal points (Bouhon *et al.*, 2020a), the linking structure in quench dynamics (Ünal *et al.*, 2020) and nontrivial orbital magnetic moments. The underlying geometry of the eigenstates in Euler bands also mediates the interaction between electrons, such as the electron pairing in superconducting twisted bilayer graphene (TBG) (Xie *et al.*, 2020, Peotta and Törmä, 2015, Bauer *et al.*, 2022). Moreover, recent findings in twisted double bilayer graphene show imbalanced Wilson loop windings in the flat bands (Crosse *et al.*, 2020), which leads to different orbital magnetic moments in subbands (Wu *et al.*, 2021). Such an imbalanced topological number suggests that the imbalanced scenario would emerge in such twisted multilayers, making it interesting to investigate the features of imbalanced Euler phases.

In this Chapter, we report the heuristic bulk-boundary correspondence of flat-band Euler insulators. Our finding covers both the balanced and imbalanced Euler phases. The balanced Euler insulators relate to mirror-Chern insulators in the dispersionless limit, while the imbalanced Euler insulators do not map to such counterparts. In both cases, the edge states exhibit a series of nodal points near the Fermi level. In the balanced case, the number of nodes equals the Euler number. While in the imbalanced phase, the algebraic order of the nodes sums up to the higher Euler number.

4.2 Flat-band Euler insulators

In two-dimensional systems with $C_2\mathcal{T}$ symmetry, there exists a global gauge where the Hamiltonian is real-symmetric. Such a real Hamiltonian gives the real vector bundle of the eigenstates, which is characterized by Euler numbers $E \in \mathbb{Z}$ if the number of bands is 2 [1]. Such $\mathbb{Z}$-topological number is fragile since the topology degenerates to $\mathbb{Z}_2$ Stiefel-Whitney class in higher-rank bundles (Ahn *et al.*, 2019a,b, Ahn and Yang, 2019). We focus on the 3-band and 4-band models of Euler insulators. As the minimal model carrying the Euler topology, 3-band models give a series of Euler numbers $E = 2N$ (Bouhon *et al.*, 2020b). On the other hand, 4-band models contain two 2-band subspaces, each giving an $\mathbb{Z}$ Euler number. The two Euler numbers form the $\mathbb{Z} \oplus \mathbb{Z}$ characterization of the 4-band system. Denoting the Euler number of occupied (empty) bands as $E^+(E^-)$, the class of general 4-band Hamiltonian is written as (E^+, E^-). Different from other characterizations, the total Euler number of the 4-band subspace is not necessarily zero. $E^- + E^+ = 0 \mod 2$ is sufficient to guarantee the orientability. Subsequently, a subclass of imbalanced Euler insulators emerges in 4-band systems, where $E^+ \neq E^-$. Such an imbalanced phase goes beyond conventional classes, and it is important to interpret its bulk-edge correspondence.

The edge spectrum of Euler insulators within the flat-band limit is shown in the followings. This limit serves as a baseline for edge spectrum studies because numerous internal symmetries are retained. The balanced case with $E^+ = E^-$, for example, essentially carries the chiral symmetry as well as an emergent $\mathcal{M}_z$ symmetry if the bands degenerate. Flat-band Euler insulators exhibit gapless edge states, of which the algebraic indexes are determined by the bulk Euler numbers.

A special case of 4-band Euler insulators is when $E^+ = E^-$, and each of the 2-band subspaces is doubly degenerated. In this case, the 2 Euler bands can be rotated into a Chern basis:

$$\begin{aligned} v_+^\alpha &= (u_a^\alpha + \mathrm{i} u_b^\alpha)/\sqrt{2}, \\ v_-^\alpha &= (u_a^\alpha - \mathrm{i} u_b^\alpha)/\sqrt{2}, \end{aligned} \tag{4.1}$$

which are also eigenstates of $\hat{H}$ due to the degeneracy. The Berry curvature on the Chern basis $F[v_+^\alpha] = (\partial_{k_1} v_-^\alpha)^T \cdot (\partial_{k_2} v_+^\alpha) - (\partial_{k_2} v_-^\alpha)^T \cdot (\partial_{k_1} v_+^\alpha)$ equals to the Euler number $\mathrm{Eu}_\alpha = F[v_+^\alpha]$ of the original bands. Furthermore, the degenerated Euler insulator has an emergent $\mathcal{M}_z$ symmetry,

---

[1] Here we only consider orientable bundles.

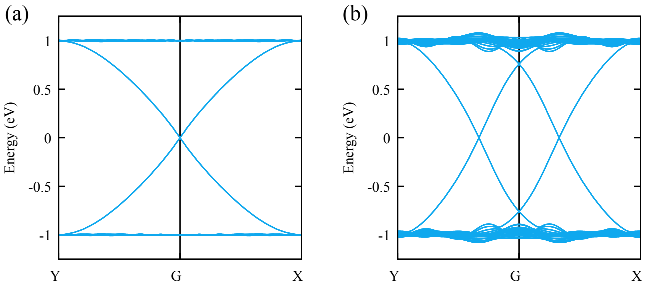

Figure 4.1 – Edge states of balanced Euler insulators and flat (degenerated) subbands. The system has emergent $\mathcal{M}_z$ symmetry, and the mirror Chern number coincides with $|E|$. (a) $E = 1$ (b) $E = 2$. From the results of $\mathcal{M}_z$ insulators, n edge states are present in $C_{mz} = n = |E|$ phase.

and the Chern basis is also an eigenbasis of the m_z operator. Under the $\mathcal{M}_z$ symmetry, each two-band subspace carries a mirror-Chern number

$$E_{-} = E_{+} = -C^{(-\mathrm{i})} = C^{(\mathrm{i})} \in \mathbb{Z}, \tag{4.2}$$

of which the absolute values coincide with the Euler number. The edge states of mirror-Chern systems have been thoroughly investigated (Kane and Mele, 2005a). In Fig. 4.1, we show two typical examples of edge states. For $C_{mz} = n$ insulators, there exist n pairings of topological edge states due to the $\mathcal{M}_z$ symmetry. The $m_z = \pm 1$ bands contribute to the two different chiralities of the edge states.

4.2.1 Imbalanced Euler insulators

The 4-band systems with $C_2\mathcal{T}$ symmetry are characterized by SO(4)/SO(2)×SO(2)=$\mathbb{Z} \oplus \mathbb{Z}$. A special property of the 4-band case is that the Euler numbers of the two subbands are not necessarily the same: only $E^{+} + E^{-} = 0 \mod 2$ is required to cancel the total second Stiefel-Whitney class. Subsequently, the "imbalanced" Euler phases emerge in 4-band systems, which is absent for other topological characterizations. Such imbalanced phases raise the question of edge states, typically, whether both $E^{+}, and E^{-}$ affect the edge spectrum.

We investigate the edge states of such imbalanced phases. Note that the topological bands with exact flatness require infinite hoppings in tight-binding (TB) models, the models are truncated in our calculation which leads to a small broadening of the bands. Fig. 4.2 shows the edge states of imbalanced Euler phases within the flat-band limit. The bands are calculated with a ribbon geometry, such that states on the two edges are twofold degenerate. Unlike in Chern or mirror-Chern insulators, the total number of edge states stays the same in the imbalanced case while Euler numbers are changed. Besides the number of edge states, the different Euler phases lead to a series of edge state crossings. In Fig. 4.2(a), the 1-3 Euler insulator has 3 linear crossing points, while the 1-5 phase leads to 5 crossings. Further calculations show that the

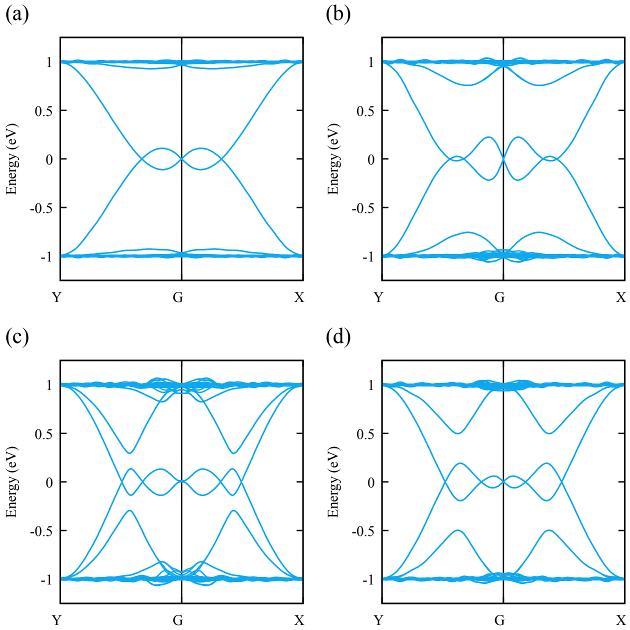

Figure 4.2 – Edge states of flat 4-band models with imbalanced Euler numbers: (a) $E^- = 1, E^+ = 3$, (b) $E^- = 5, E^+ = 1$, (c) $E^- = 2, E^+ = 6$ and (d) $E^- = 3, E^+ = 5$.

sum of crossing indexes equals the higher one between the Euler numbers:

$$\sum p_i = \max\{|E^+|, |E^-|\}, \tag{4.3}$$

denoting p_i as the order of the ith crossing point, eg: p=1 for linear crossing and p=2 for quadratic crossing. As an example, the edge states of 2-6 Euler numbers (see Fig. 4.2(c)) have 2 linear crossings and 2 quadratic crossings, leading to $\sum p_i = 2 + 2 \times 2 = 6$.

A remarkable feature of the imbalanced flat bands is that the edge index $\sum p_i$ is not only determined by the topology of occupied states, as in other types of topological classes. If the system carries $E^+ > E^-$, the crossing of edge bands gives the Euler number of the *unoccupied* 2-band subspace. The reflection of the conduction band Euler number in the edge index then reveals a fundamental difference from the usual topological classification. Moreover, with the Euler numbers, it is possible to extract the dispersion of edge states, not only the number of edge modes.

4.3 Theory

We establish the theory of edge states by a continuum deformation from bulk polarization to the edge Hamiltonian Coh and Vanderbilt (2009), Fidkowski *et al.* (2011). Such construction is adapted from the proof of Wannier centre-edge state correspondence Alexandradinata *et al.*

(2016), Fidkowski *et al.* (2011). The starting point is a spectrally flat Hamiltonian:

$$H_f = P^+ - P^-, \tag{4.4}$$

where $P^\pm$ indicates the projection operator to the occupied (−) or empty (+) bands:

$$P^\pm(k) = \sum_\pm |u_k^\pm\rangle\langle u_k^\pm|. \tag{4.5}$$

The flat-band Hamiltonian H_f evolves to the edge Hamiltonian if connected to a negative chemical potential $V(y)$: [2]

$$H_e = P^+V^+(y)P^+ - P^-V^-(y)P^-. \tag{4.6}$$

Such a connection is chosen as the open boundary conditions on the y-direction. The deformation of H_f naturally behaves as an interpolation between the bulk polarization $\phi_y(k_x) = P(k_x)\hat{y}P(k_x)$ and the edge Hamiltonian H_e [3]. Therefore, we manage to construct an edge Hamiltonian with ϕ_y. The polarization $P\hat{y}P$ is equivalent to the Wannier charge centre (WCC) winding since:

$$\mathscr{W}_y^\pm(k_x) = \exp\big(iP\hat{y}P\big) = \exp\left[\int_{k_y}\langle u_k|\partial_{k_y}|u_k\rangle\right]. \tag{4.7}$$

($\mathscr{W}_y^\pm = e^{i\phi_y^\pm}$), which is contained in eq7 Given that $H_e(k_x)$ is with the same form as the polarization $\phi_y(k_x)$, it is possible to construct H_e based on the Wilson loop winding.

We start with an assumption about the shape of effective 2-band TB models (for the two bands which cross at the Fermi level) with hopping range N:

$$H_e(k_x) = \sum_{n=-N}^{N}(\sigma_x t_x^n + \sigma_y t_y^n + \sigma_z t_z^n)e^{ik_x\cdot r_n}. \tag{4.8}$$

For simplicity, we first assume that the edge Hamiltonian is real-symmetric, as required by the $C_2\mathscr{T}$ symmetry. Since gapless states are expected, the real-symmetric Hamiltonian H_e^{RS} contains only σ_x terms (adding σ_z terms will open an energy gap)

$$H_e^{RS}(k_x) = \sum_{n=0}^{N} 2t_x^n\sigma_x\cos(k_x r_n) = \sum_{n=-N}^{N} t_x^n\sigma_x e^{ik_x r_n}. \tag{4.9}$$

The algebraic order of Eq. 4.9 naturally depends on $N : \sum p_i = N$. Following the polarization operator $P\hat{y}P$, and regarding the WCC sheet of Euler bands as a pair of winding, N is the same as the winding number of the Wilson loop. To see this, we use a construction of deformation on the Wilson loop preserving only the winding number $f(\mathscr{W})$:

---

[2] $V(y)$ serves as an interpolating parameter to bridge the Wilson loop with edge states, of which the explicit form is not required.

[3] While the interpolation acts as $H_e = V(\phi_y, k_x)\phi_y(k_x)$, the perturbative behavior near the nodal points $\phi_y = 0$ is determined by ϕ_y: $H_e' = V'\phi_y + V\phi_y' \approx V\phi_y'$.

$$f(\mathscr{W}^{\pm}) = e^{-i\sum\int dk\phi_y^{-1}\partial_k\phi_y} + e^{+i\sum\int dk\phi_y^{-1}\partial_k\phi_y}, \tag{4.10}$$

the WCC sheet with winding $N^{\pm}$ is continuously deformable into: $\sum_n \sigma_x[\exp(ik_x \cdot n/2) + \exp(-ik_x \cdot n/2)]$ which contain minimal number of terms. Replacing the parameters produces a Hamiltonian H_X of variable X:

$$H_X^{\pm} = \sigma_x(e^{-iN^{\pm}k_x/2} + e^{+iN^{\pm}k_x/2}) = \sigma_x(X^{N^{\pm}} + X^{-N^{\pm}}), \tag{4.11}$$

Equation. 4.11 expands H_e to an algebraic function of a general complex number X. This automatically gives the algebraic order on the whole complex plane. The difference of algebraic order $\pm N$ indicates $2N$ zero points on the plane, which are symmetric to the real axis, i.e. $H(a+bi) = 0 \rightarrow H(a-bi) = 0$ [4]. In the flat-band limit, our results show that all the $2N$ roots reside on the unit circle $X = \exp(i\theta)$. Moreover, summing up the contribution of conduct bands and valance bands involves the Euler numbers of both subspaces: $H = \sigma_x[X^{N^+} + X^{-N^+} + \gamma(X^{N^-} + X^{-N^-})]$. It is obvious that the order of these roots sums to $\max\{N^+, N^-\}$ regardless of the degeneracy.

The discussions above apply well to the flat-band Euler insulators. Note that Eq. 4.11 gives the number of zero points on the complex plane, the roots might escape from the unit circle and thus gap some of the nodes. The flat-band limit is considered a special case to establish the theories. In general Euler bands, which may be dispersive and break various symmetries, the edge states are not predictable by the theory in sec.III. It is thus important to inspect the bulk perturbations and their effect on the edge spectrum.

Going further than the flat-band case, we construct models that remove the degeneracy or band flatness. The flat-band Hamiltonian, or equivalently its projector expression, has several emergent symmetries such as exact band degeneracy and particle-hole symmetry which are to be broken. In Fig. 4.3, we present the edge states in non-flat band systems, both with the imbalanced 4-band model where E^+=3 ,E^-=1, and in the 3-band model with E=2. Different from the flat-band cases, the edge nodal points are gapped in both cases. Such a phenomenon is concluded as a consequence of the chiral symmetry breaking. Instead of the previous perturbative expression near the nodes $H_i = \sigma_x(X^N + X^{-N})$, the perturbed nodes are approximated by:

$$H_i^{\delta} = \sigma_x(X^N + X^{-N}) + \delta\sigma_z. \tag{4.12}$$

Such a form of approximation suggests that the algebraic order is still traceable in the presence of a small symmetry breaking. To fully portray the nodal points on the edge spectrum, we extend the domain of X from the conventional BZ $X = e^{ik_x}$ to the entire complex plane. Such a variation can be interpreted as a gain or loss term on the couplings, which is seen in the

---

[4] Alternatively, one can consider the set $\cos(k_x \cdot n/2)$ while using the replacing $X \rightarrow e^{ik_x/2}$. The resulting polynomial is then also integer-ordered, while the actual momentum terms lie on the plane as X^2.

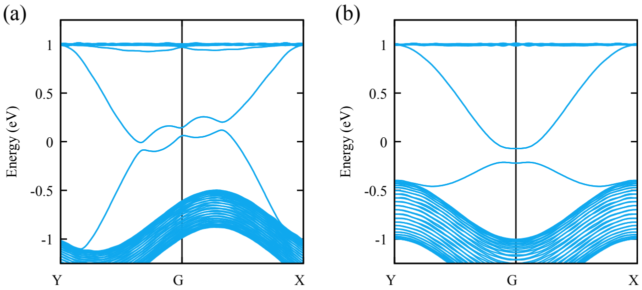

Figure 4.3 – Open-boundary band structures of (a) 4-band model with $(E^+, E^-) = (1,3)$, (b) 3-band model with E=2. The band flatness and emergent E to $-E$ symmetry are broken. Subsequently, the edge states are now gapped.

studies on non-Hermitian systems (Yao and Wang, 2018, Zhang *et al.*, 2020b). We track the zero points of a model Hamiltonian:

$$H(k,\delta) = [X^3 + X^{-3} + \gamma(X^1 + X^{-1})]\sigma_x + \delta\sigma_z. \tag{4.13}$$

Typical layouts of zeros are presented in Fig. 4.4. The subplots Fig. 4.4(a)→(b)→(d) depicts the effects of γ. At $\gamma = 0.2$ three nodes in linear order are expected, while (b) exhibits the critical case where an order-3 node emerges. When γ is further increased, the zeros start to escape from the BZ. Such escaping of zeros is also triggered by δ terms which represent the perturbative symmetry-breaking, see Fig. 4.4(a-c). By extending the momentum to the complex plane, the relation between bulk Euler number and edge algebraic order becomes exact. In addition to tracing the nodes by Eq. 4.12, one would expect such correspondence to be observed in a tunable non-Hermitian setup.

4.4 Conclusions

In this Chapter, we address the edge state features of the flat-band Euler insulators. In the limit of flat bands, the bulk spectrum is equivalent to the sum of projectors, giving a series of crossing points on the edge bands. These crossing points serve as probes of the Euler number. In particular, the algebraic index of the crossing points can give the invariant in imbalanced Euler insulators. The index reflects the higher Euler number between occupied and empty bands. Its capability goes beyond traditional observables which can only probe the topological invariant in the occupied bands, making it possible to gain information on unoccupied bands as well. Such observations from Euler insulators build the correspondence to not only the number of edge states but also their shapes. Furthermore, since the Euler number is highly related to reciprocal node braiding, it is worth investigating the form of edge Hamiltonian Eq. 4.11, in comparison to knot polynomials. Going to the dispersive bands, the edge nodal points are broken by the violation of spectral symmetry. However, the corresponding projector spectrum would still behave the same, and the signature of the algebraic indexes is visible in the shape of edge states.

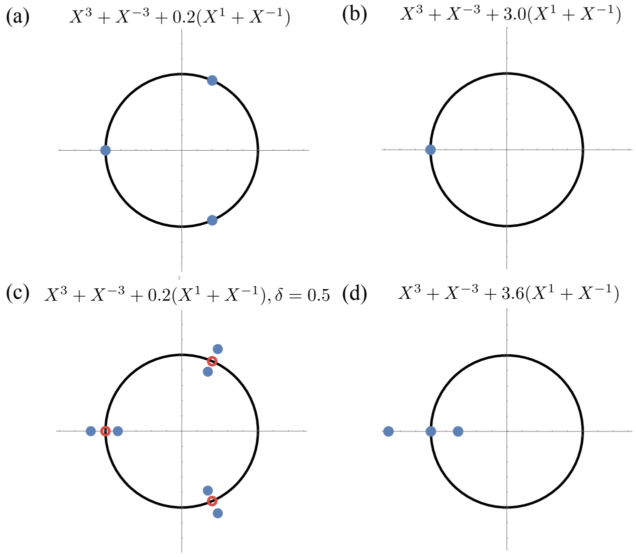

Figure 4.4 – Evolution of zeros by tuning the parameters in model Hamiltonian $H = [X^3 + X^{-3} + \gamma(X^1 + X^{-1})]\sigma_x + \delta\sigma_z$. (a) $\gamma = 0.2, \delta = 0$ provide 3 different zeros reside on the BZ. (b) $\gamma = 3.0, \delta = 0$ indicates a critical case that the zeros merge to an order-3 node. (c) $\gamma = 0.2, \delta = 1.5$ and (d) $\gamma = 3.6, \delta = 0$ show two ways of zeros escaping from the conventional BZ by δ and γ terms.

Investigating the correspondence of the *dispersion* of edge states to the bulk topological invariant, our work opens a new perspective of bulk-edge correspondence. Besides revealing the edge states, it also provides insight into emergent special properties originating from band flatness.

Part II

Topological effects in twisted multilayer graphene

5 Re-entrant magic-angle phenomena in twisted bilayer graphene

In this Chapter we address the re-entrance of magic-angle phenomena (band flatness and quantum-geometric transport) in twisted bilayer graphene (TBG) subjected to strong magnetic fluxes $\pm\Phi_0$, $\pm 2\Phi_0$, $\pm 3\Phi_0$... ($\Phi_0 = h/e$ is the flux quantum per moiré cell). The moiré translation invariance is restored at the integer fluxes, for which we calculate the TBG band structure using accurate atomistic models with lattice relaxations. Similarly to the zero-flux physics outside the magic angle condition, the reported effect breaks down rapidly with the twist. We conclude that the magic-angle physics re-emerges in high magnetic fields, witnessed by the appearance of flat electronic bands *distinct* from Landau levels, and manifesting non-trivial quantum geometry. We further discuss the possible flat-band quantum geometric contribution to the superfluid weight in strong magnetic fields (28 T at 1.08° twist), according to Peotta-Törmä mechanism (Peotta and Törmä, 2015).

In this chapter, we show the study of Fubini-Sturdy metric of TBG, under different levels of external magnetic field. The main results include the high-field band structure and topology of TBG, while we further provide a comparison of the quantum metric to the Berry curvature. The chapter is adapted from:

Yifei Guan , Oleg V. Yazyev, Alexander Kruchkov
Re-entrant magic-angle phenomena in twisted bilayer graphene in integer magnetic fluxes, Phys. Rev. B 106, L121115 (2022)

My contribution to this work includes developing the high-field calculation workflow, and the methods of computing the map of the Fubini-Sturdy metrics.

5.1 Introduction

In 2D systems, the electronic spectrum in a magnetic field develops a fractal structure ("Hofstadter butterfly") (Hofstadter, 1976), which lowers the effective dimensionality, and contributes to suppressing superconductivity (long-range order is generically destroyed in dimensions

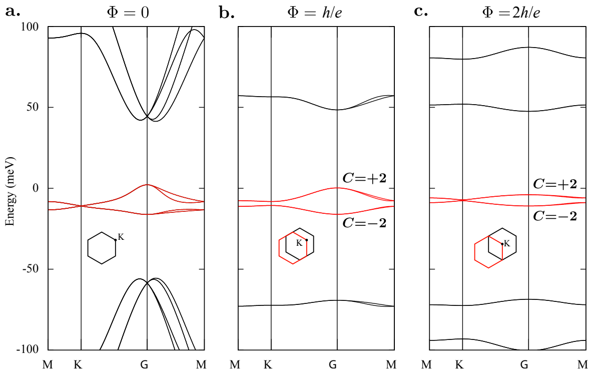

Figure 5.1 – Electronic band structure of magic-angle twisted bilayer graphene in integer magnetic flux: (a) zero flux ($\Phi = 0$); (b) flux one ($\Phi = h/e$); (c) flux two ($\Phi = 2h/e$). All band structures are calculated with tight binding model including lattice relaxations effects. In these fluxes, the lower (two out four) flat bands acquire Chern number $C = -2$.

lower than D=2). The observation of Hofstadter physics requires strong magnetic fluxes ($\sim h/e$), which became experimentally accessible only with the advent of moiré superlattices (Dean *et al.*, 2013, Hunt *et al.*, 2013, Ponomarenko *et al.*, 2013). In those experiments (Dean *et al.*, 2013, Hunt *et al.*, 2013, Ponomarenko *et al.*, 2013), the magnetic fields of nearly 30 T were employed in the system of graphene monolayer twisted on hexagonal boron nitride (hBN), resulting into effective fluxes of $\Phi = B/A \sim \Phi_0$ (A is the moiré cell area, $\Phi_0{=}h/e$ =4 Wb is magnetic flux quantum). Furthermore, the twisted graphene multilayers provide a natural platform to test the interplay between the Hofstadter physics and strong correlations (Cao *et al.*, 2018a, Hao *et al.*, 2021, Park *et al.*, 2021b,c, Zhang *et al.*, 2021). In twisted bilayer graphene, the smaller is the twist θ, the larger is the effective magnetic flux ($\Phi \propto 1/\theta^2$) at the fixed field $\mathbf{B}$: for TBG at the magic angle 1.08° the magnetic flux, quantum corresponds to $B_0 \approx 28$ T, which is reachable in the modern laboratories (Hahn *et al.*, 2019).

The magic-angle graphene heterostructures—two or more graphene sheets twisted to the angle $\sim 1°$, at which a very narrow band emerges in the electronic spectrum—have re-attracted significant attention due to re-entrant superconductivity in strong magnetic fields and reported Pauli limit violation (Cao *et al.*, 2021, Chaudhary *et al.*, 2021, Shaffer *et al.*, 2021). The re-entrant correlated (Chern) insulator phases were reported at strong magnetic fluxes (Das *et al.*, 2022, Herzog-Arbeitman *et al.*, 2021), close to the unit magnetic flux quantum $\Phi_0 = h/e$ per moiré unit cell (see also Ref. (Sheffer and Stern, 2021)). Naturally, one would expect Landau-level-like wave functions to be dominant at $B \approx 28$ T, and both topology and quantum geometry of the Bloch states to be the same as at the zero field. In particular, at zero field, the continuum model of TBG maps the magic angle flat band on the (lowest) Landau level wavefunctions, where the effective nonhomogeneous magnetic field originates from moiré interlayer potentials (Tarnopolsky *et al.*, 2019). Our main surprise is that after inserting the physical flux $\Phi_0{=}h/e$, from the atomistic perspective this mapping is no longer valid: The magnetic magic-angle flat bands are *distinct* from the Landau levels.

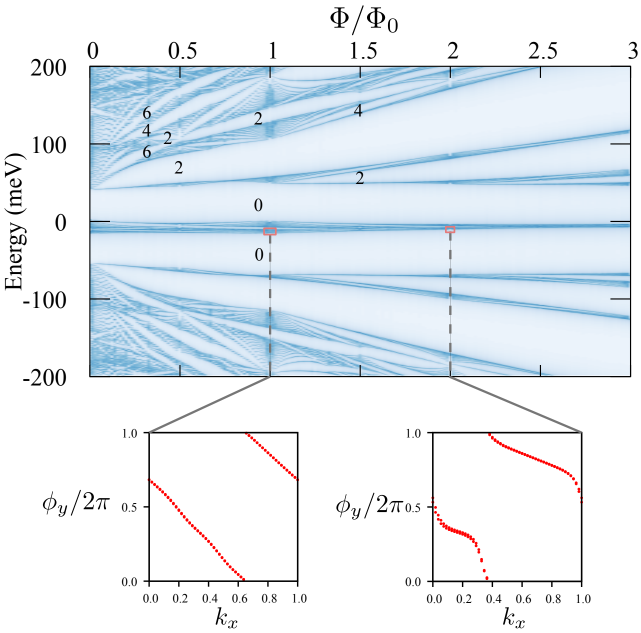

Figure 5.2 – Hofstader spectrum of magic-angle bilayer graphene in magnetic flux (in units h/e). The digits in gaps indicate the in-gap Chern numbers, calculated through the edge modes counting. Additionally, the insets below show Wannier charge center (WCC) winding at fluxes h/e and $2h/e$, calculated at the half filling of the flat bands (2 of 4 subbands are occupied). The WCC winding is nontrivial, revealing $|C|$=2 at half filling in the integer flux.

In this Chapter we report that the nontrivial quantum geometry, electronic band flatness, and conditions for unconventional quantum transport are re-established at integer magnetic flux (in units of h/e) through the moiré unit cell. Similarly to the zero-flux case, the Fermi velocity and the bandwidth drop dramatically at the magic angle, to reappear as a dispersive band both below and above the magic angle. Importantly, the flat bands in finite flux expose nonzero Chern numbers $|C|$=2 (defined at half-filling, see Fig. 5.1) and non-trivial quantum geometry, which follows the quantum-geometric flatness criterion (Kruchkov, 2022a)

$$\mathrm{Tr}\mathscr{G}_{ij}(\mathbf{k}) \simeq |\mathscr{F}_{xy}(\mathbf{k})|. \tag{5.1}$$

We show numerically with atomistic calculations that in the realistic TBG, the ideal flat band condition Eq. 5.1 is satisfied in the magnetic moiré Brillouin zone (mmBZ) regions where the band flatness is pronounced in terms of vanishing Fermi velocity (e.g. around the K points of mmBZ). Here $\mathscr{G}_{ij}$ and $\mathscr{F}_{xy}(\mathbf{k})$ are the real and imaginary parts of the quantum-geometric tensor $\mathfrak{G}_{ij}$ (see further), determining the quantum distance between electronic states in the (projected) Hilbert space (Provost and Vallee, 1980).

5.2 Approach

Instead of using the continuum models, in this Chapter we investigate the effect of strong magnetic fluxes with the help of the accurate atomistic model including TBG lattice relaxation effects at the magic angle, and compare the observed results with the established knowledge of the zero-flux TBG case. More details of the tight-binding Hamiltonian are provided in Sec. 2.3. The key observation is that the magnetic translation operators commute at every integer flux $\Phi = N\Phi_0$, namely

$$\hat{T}_{\mathbf{a}_1}\hat{T}_{\mathbf{a}_2} = e^{i2\pi\Phi/\Phi_0}\hat{T}_{\mathbf{a}_2}\hat{T}_{\mathbf{a}_1}, \;\rightarrow\; [\hat{T}_{\mathbf{a}_1}, \hat{T}_{\mathbf{a}_2}]_{\Phi=N\Phi_0} = 0.$$

Thus the moiré unit cell is restored, and the system flows towards the electronic band structure defined on the mmBZ, which in the integer flux has the same periodicity as the moiré Brillouin zone (mBZ) in zero magnetic flux. But instead of dispersionless Landau levels, we recover the set of dispersive bands, with its band structure depending crucially on the twist angle (Fig. 5.3).

5.3 Re-entrant magic angle spectra at integer magnetic flux

We start from considering the electronic band structure at an integer magnetic flux $\Phi = Nh/e$. Such a flux provides the $2\pi N$ circulation of magnetic vector potential, and hence reconstructs the moiré Brillouin zone (mBZ→mmBZ); magnetic translation operators commute at integer flux $[\hat{T}_{\mathbf{a}_1}, \hat{T}_{\mathbf{a}_2}] = 0$. This allows us to re-introduce momentum as a good quantum number and compute the electronic band structure starting from the tight binding model (Gargiulo and Yazyev, 2018, Nam and Koshino, 2017) for magic-angle twisted bilayer graphene with atomic relaxations, modified with Peierls substitution,

$$t_{ij} \rightarrow t_{ij} e^{-i\frac{e}{\hbar}\int_{\mathbf{r}_j}^{\mathbf{r}_i}\mathbf{A}(\mathbf{r}')d\mathbf{r}'}. \tag{5.2}$$

Compared to the widely-used continuum models (Bistritzer and MacDonald, 2011b, Tarnopolsky *et al.*, 2019, Lopes Dos Santos *et al.*, 2007), the accurate tight binding model has an important advantage of addressing the magic-angle physics under realistic conditions of atomic lattice relaxations, proved to be indispensable in the experiments due to domain formation (Carr *et al.*, 2018). Worth noting, the finite magnetic flux shifts the effective Brillouin zone (see Fig. 5.1), thus re-defining the positions of high-symmetry points. Otherwise, the original moiré Brillouin zone and the reconstructed magnetic moiré Brillouin zone have the same orientation and periodicity, which is the main technical condition to observe the magic angle phenomena.

We report that the characteristic flat band, the hallmark of the magic-angle graphene, reappears in *every* integer magnetic flux, $\pm\Phi_0$, $\pm 2\Phi_0$, $\pm 3\Phi_0$... Figure. 5.1 provides the electronic band spectrum at $\Phi = 0, \Phi_0, 2\Phi_0$. The first observation is that the flat band reappears exactly at the magic angle, while the higher bands are dispersive (see Fig. 5.3). We argue below that

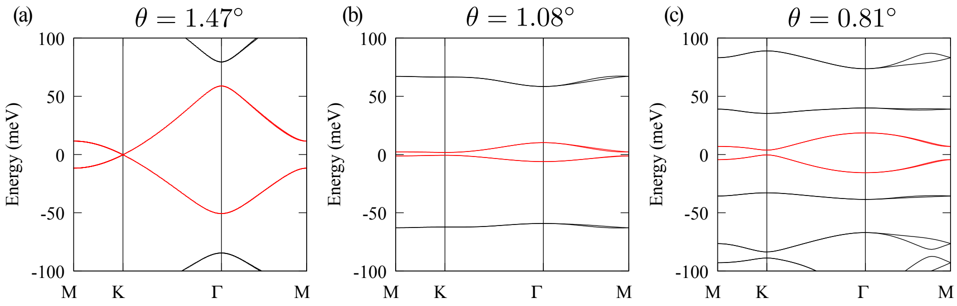

Figure 5.3 – Magic angle signature in integer magnetic flux $\Phi = h/e$ at different twists. (a) Above the magic angle, $\theta = 1.47°$. (b) At the magic angle, $\theta = 1.08°$. (c) Below the magic angle, $\theta = 0.81°$. We observe the similar behavior as the zero-flux TBG tuned outside of the magic angle (Bistritzer and MacDonald, 2011b, Tarnopolsky *et al.*, 2019).

the magic-angle flat bands (MAFBs) in the integer flux *are not* a consequence of Landau level (LL) flattening [1] since: **(i)** It has $|C|$=2 at half-filling; **(ii)** It demonstrates quantum geometry incompatible with LL physics (Fig. 5.3); and **(iii)** It becomes dispersive outside the magic angle. Worth noting, the strong magnetic fields restore the asymptotic particle-hole symmetry of the low energy states, which was moderately broken in the zero flux.

5.4 Magnetic spectrum distinct from Landau levels

We further address the properties of the electronic band spectrum versus magnetic field. For this, the characteristic quantity to calculate is the Hofstadter diagram, which traces the energy of electronic states allowed in quantized magnetic field, as a function of magnetic flux through the unit cell (Fig. 5.2). We observe that the flat bands at the integer flux are not stemming from Landau level Hofstadter physics, but rather from the magic angle physics of the TBG. To show that they are fundamentally different from the LLs, we calculate the Chern number through Wilson loop computation in the form of Wannier charge center winding, see Fig. 5.2. We find that the flat bands at integer Φ have Chern numbers $|C| = 2$ incompatible with Chern numbers of Landau levels on the lattice ($|C| = 1$). Furthermore, we fix magnetic flux to h/e, and investigate the change in electronic band spectrum versus the *change in twist angle*. While the spectrum is strongly dispersive outside of the magic angle (the bandwidth is approximately 100 meV at 1.47° twist, at the magic angle 1.08° the bandwidth is just 15 meV, *comparable* to the magic angle bandwidth in zero flux (see also Fig. 5.1). We conclude that the magic angle physics is in its essence restored.

---

[1] We remark that Ref. (Herzog-Arbeitman *et al.*, 2021) comes to the similar conclusions for the gapless case when all the bands are occupied. The gap opening at the Dirac point occurs in case of C_2 or C_{3z} symmetry breaking, which leads to appearance of the Chern numbers C=±2 at half filling

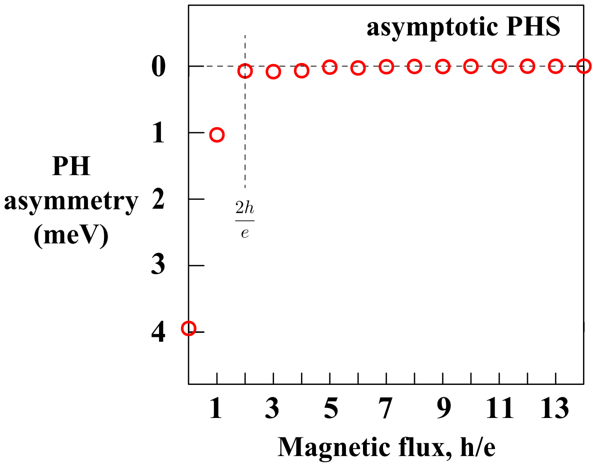

Figure 5.4 – Asymptotic particle-hole symmetry (PHS) in strong magnetic flux is emergent for $\Phi \geq 2h/e$. The low-energy PH asymmetry of the flat bands is determined as a maximum energy difference between the conductance and valence bands at neutrality, in meV. The PH asymmetry is maximal in zero flux ($\Phi = 0$) resulting in nearly 4 meV. The PHS violation is however strongly suppressed with applied magnetic field, resulting to 1 meV at $\Phi = h/e$, and just 0.07 meV at $\Phi = 2h/e$. The suppression of PH asymmetry roughly follows $\sim \exp[-\Phi/\Phi_*]$, with $\Phi_* \approx 0.7h/e$.

5.5 Emergent particle-hole symmetry

We now focus on the low-energy numerical analysis of the flat bands. The main observations under strong magnetic fields is that the low-energy electronic spectrum, featuring flat bands, acquires asymptotic particle-hole symmetry (Fig. 5.4) To quantify the particle-hole asymmetry (PHA), we track the maximum difference in the flat band energies between the occupied and free bands at neutrality, and investigate it versus magnetic field (Fig. 5.4). We observe that while PHS is generically violated in zero flux (PHA = 4 meV), in strong magnetic fields this symmetry reemerges in its asymptotic form above $\Phi \geq 2h/e$ (Fig. 5.4). Approximately, the suppression of PH asymmetry is observed as $\sim \exp[-\Phi/\Phi_*]$, with $\Phi_* \approx 0.7h/e$ (corresponding to ≈ 20 T). This could be qualitatively understood in terms local tight binding hoppings, which due to strong magnetic fields are oscillating rapidly in space; the system thus performs self-averaging which re-defines effective hopping parameters. In realistic TBG systems at $B = 0$, with sublattice hoppings and lattice relaxations, the Chern number in zero flux vanishes since the particle-hole symmetry (PHS) is violated on the atomistic level, chiral symmetry (CS) is broken explicitly, and time reversal (TRS) is present. At integer fluxes, we have asymptotic PHS, broken TRS, broken CS, and while strictly speaking the system belongs to class A topological insulator, its dynamics flows towards class C, characterized by $2Z$ (even-valued) topological invariants in 2D systems (Altland and Zirnbauer, 1997). This gives a plausible explanation of promotion of the $|C|$=2 Chern numbers in the flat bands at integer flux $|\Phi| \geq \Phi_0$, once the two of four subbands are slightly gapped out (Fig. 5.1). We observe that the magic-angle TBG at zero flux $\Phi = 0$ and integer flux $\Phi = h/e$ belong to different topological classes, which should be taken into account for understanding recent TBG experiments.

5.6 Non-trivial quantum geometric properties

We report that the magic-angle flat band in integer magnetic flux has non-trivial quantum geometry (Fig. 5.5), distinct from Landau levels. The quantum geometry is defined for the Bloch states in the projective Hilbert space; it can be separated into real (diagonal) part which is Fubini-Study metrics, and imaginary (off-diagonal) part, with its components being Berry curvature (Provost and Vallee, 1980). Numerically, we compute quantum-geometric tensor for flat bands in TBG by using its spectral representation (Kruchkov, 2022b)

$$\mathfrak{G}_{ij}(\mathbf{k}) = \sum_{n,m} \frac{\langle u_{n\mathbf{k}}|\frac{\partial \mathscr{H}_{\mathbf{k}}}{\partial k_i}|u_{m\mathbf{k}}\rangle_0 \langle u_{m\mathbf{k}}|\frac{\partial \mathscr{H}_{\mathbf{k}}}{\partial k_i}|u_{n\mathbf{k}}\rangle_0}{(\varepsilon_{n\mathbf{k}} - \varepsilon_{m\mathbf{k}})^2}. \tag{5.3}$$

We further introduce $\mathscr{G}_{ij}$=Re$\mathfrak{G}_{ij}$, $\mathscr{F}_{ij}$=-2 Im$\mathfrak{G}_{ij}$. One can find a basis in which $\mathscr{G}_{ij}$ is diagonal and $\mathscr{F}_{ij}$ is off-diagonal. The plots for $\mathscr{G}_{xx}, \mathscr{G}_{yy}$ (Fubini-Study metrics) calculated at half-filling are presented in Fig. 5.5. We observe that the re-entrant flat band has nontrivial quantum geometry within the mmBZ, as manifested in Figs. 5.5(a,b,c), which is not compatible with a Landau level quantum geometry (the LL quantum geometry is constant in the whole Brillouin zone).

For comparison, we plot the Berry curvature $\mathscr{F}_{xy}$ together with trace of Fubini-Study's $\mathscr{G}_{ij}$ in Fig. 5.3d. We observe that the flat band closely follows the quantum-geometric condition for ideal flat bands (Kruchkov, 2022a) Tr$\mathscr{G}_{ij}$=$\mathscr{F}_{xy}$. It is certainly interesting that this condition is satisfied almost exactly in the regions of mmBZ, where the band flatness is pronounced in terms of vanishing Fermi velocity (around the K points of mmBZ). The deviation to this quantum-geometric bound Tr$\mathscr{G}_{ij}(\mathbf{k})$=$\mathscr{F}_{xy}(\mathbf{k})$ are observed in the regions of mmBZ with finite dispersion and significant $v_{\mathbf{k}}$=$\partial\varepsilon_{\mathbf{k}}/\partial\mathbf{k}$ caused by broken CS of the tight-binding calculations. The criterion Tr$\mathscr{G}_{ij}(\mathbf{k}) = \mathscr{F}_{xy}(\mathbf{k})$, tests the closeness of a realistic flat band in TBG to flat band idealization through holomorphic/meromorphic representation of the flat band wave functions (Kruchkov, 2022a). However, since total $|C| = 2$, the relevant toy model for TBG in integer flux cannot be represented by solely a holomorphic representation of the quasi-LLL TBG (found in Ref. (Tarnopolsky *et al.*, 2019)); one needs to take meromorphic flat band contributions into account (Popov and Milekhin, 2021). Since the Berry curvature $\mathscr{F}_{xy}(\mathbf{k})$, calculated within the mmBZ (Fig. 5.3), reveals a non-homogeneous structure, it is not consistent with the homogeneous Berry curvature of the generic Landau levels (LLs are "Berry flat"). For scale comparison, we sketch the Berry-flat lowest Landau level distribution on the same plot (Fig. 5.3a) as the dashed grey line. The non-homogeneous quantum geometry of TBG can exceed this bound by nearly an order in magnitude. Finally, we check numerically that the TBG Berry flux $\mathscr{F}_{xy}$ in mmBZ (red line in Fig. 5.5a) sums up to $|C|$=2.0 ± 0.07 at the half-filling (see also Figs. 5.1, 5.2).

5.7 Quantum-geometric transport

As was first introduced by Peotta and Törmä (Peotta and Törmä, 2015), the nontrivial quantum-geometric tensor $\mathfrak{G}_{ij}$ leads to the the finite superfluid current $J_i{=}-D_{ij}A_j$ even in the limit of perfectly flat band (here D_{ij} is the superfluid weight). This argument is now understood to apply directly to TBG in zero flux, where the $\mathrm{Tr}\mathscr{G}_{ij}$ is nonzero due to nontrivial topology of the flat bands. [2]. It was reported with different methods (Xie *et al.*, 2020, Hu *et al.*, 2019, Julku *et al.*, 2020) that the quantum geometric tensor (QGT) contribution to the superfluid weight D_S in TBG is if not dominant, than at least commensurate with the conventional contributions, thus leading to the BTK transition temperature estimate $T_{\mathrm{BKT}} \sim \sum_{\mathbf{k}} \mathrm{Tr}\mathscr{G}_{ij}$. The QGT contribution holds for different symmetries of the order parameter, and the argument is valid beyond the mean field (Wang *et al.*, 2020). The essential physics is captured by Bogoliubov-de-Gennes Hamiltonian (Sigrist and Ueda, 1991)

$$\mathscr{H}_{\mathrm{BdG}} = \begin{pmatrix} H_{\mathbf{k}} & \Delta_{\mathbf{k}} \\ -\Delta^*_{-\mathbf{k}} & -H^*_{-\mathbf{k}} \end{pmatrix}. \tag{5.4}$$

Without loss of generality, we consider superconducting order $\Delta_{\mathbf{k}} = \Delta$. The superfluid weight is then calculated within Kubo formalism through the current-current correlators. We explicitly calculate $\mathscr{G}_{ij}$ numerically (Fig. 5.4) with consequent mmBZ integration at half-filling (for two of four flat bands occupied, we have $\mathrm{Tr}\mathscr{G}_{ij} \approx 2.8$), to obtain at the superfluid weight maximum positioned at the middle of the composite flat band with $|C| = 2$,

$$D_{xx} = \frac{2e^2}{\hbar^2}\Delta \sum_{\mathbf{k}} \mathrm{Tr}\mathscr{G}_{ij}(\mathbf{k}) \approx (5.6 \pm 0.1)\frac{e^2}{\hbar^2}\Delta. \tag{5.5}$$

Symmetry $D_{xx}{=}D_{yy}$ is assumed. Here we took into account factor $\sqrt{\nu(1-\nu)}$ (in notations of Ref. (Peotta and Törmä, 2015)), where ν is the filling factor of the composite flat band (indexed by $C = -2$ in Fig. 5.1).

We can further make estimates for the BKT transition temperature (Berezinskii, 1971, Kosterlitz and Thouless, 1973, Nelson and Kosterlitz, 1977), indicating the disappearing of the phase coherence of superconducting order from expression $\pi\hbar^2 D(T_*)/8e^2 T_* = 1$. The order-of-magnitude estimate gives $T_* \sim \hbar^2 D(0)/e^2 \sim \Delta$. The remaining question is of course, what is the value of Δ, which should be found self-consistently by solving Gorkov equations in magnetic field, or through indirect experimental data—and it is beyond the scope of this work. For a rough estimate, even $\Delta \sim 0.1$ meV will give a physically relevant $T_* \sim 1$ K.

---

[2] We remark that the flat band in (5.5) is not required to expose nonzero Chern numbers, but it does need to feature Wannier-obstructed electronic orbitals (and hence, nontrivial quantum geometry (Marzari and Vanderbilt, 1997)). Hence, the superfluid weight (5.5) originates from the interband transitions, finite due to the Wannier orbitals overlap of the bare states. The presence of nonzero Chern number (e.g. C=2 in our case) automatically satisfies this criterion

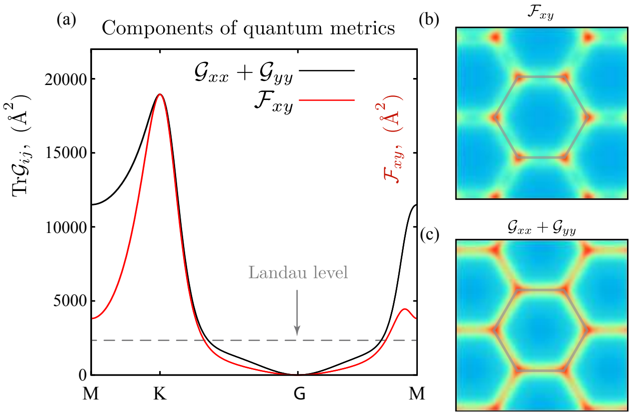

Figure 5.5 – Nontrivial quantum metrics in integer magnetic flux $\Phi=h/e$, calculated at half-filling (two of four flat bands are occupied). (a) Comparison between the trace of Fubini-Study tensor $\mathrm{Tr}\mathscr{G}_{ij}$ and Berry curvature $\mathscr{F}_{xy}$, which probes how close the band flatness is to the perfect flatness through closeness to $\mathrm{Tr}\mathscr{G}_{ij}(\mathbf{k})=|\mathscr{F}_{xy}(\mathbf{k})|$. For scale comparison, the dashed grey line at 2320 Å^2=$\mathrm{Tr}\mathscr{G}_{ij}(\mathbf{k})=\mathscr{F}_{xy}(\mathbf{k})$ indicates the Berry-flat distribution, associated with the lowest Landau level (LLL). All quantities are normalized to the moiré BZ area $A_{\mathrm{mBZ}}=8\pi^2/\sqrt{3}a_M^2$=2.74$\cdot$10^{-3} Å^{-2} (hence $\int_{\mathrm{mBZ}}\frac{d\mathbf{k}}{2\pi}\mathscr{F}_{xy}^{\mathrm{LLL}}=1$). (b-c) Map of the quantum geometric tensor $\mathfrak{G}_{ij}(\mathbf{k})$ for flat bands in TBG: (b) shows the map of $\mathscr{F}_{xy}=-2\mathrm{Im}\mathfrak{G}_{xy}$, while (c) gives $\mathrm{Tr}\mathscr{G}_{ij}$.

5.8 Conclusions

We conclude that there is a re-entrant magic angle physics in twisted bilayer graphene at every integer magnetic flux quanta $\pm\Phi_0$, $\pm2\Phi_0$, $\pm3\Phi_0$, *etc.*, through the moiré cell. To date, the practical importance represents the first magnetic quantum $\pm\Phi_0$, which at twist angle 1.08° corresponds to experimentally-achievable fields of 28 Tesla. We confirm with accurate atomistic calculations, incorporating lattice relaxation effects, that at such fields the magic-angle phenomena re-emerge. This, in particular, could be seen through the re-emergence of very flat bands at the magic angle distinct from Landau levels, while beyond the magic angle this physics breaks down, similar to the zero-flux case (Bistritzer and MacDonald, 2011b, Tarnopolsky *et al.*, 2019). These flat bands at half filling carry nontrivial Chern numbers ($|C|$=2) and nontrivial quantum geometry (Fubini-Study metrics), and are fundamentally different from conventional Landau levels. We conjecture that, similar to TBG in the zero flux, there is a nonvanishing contribution to the superfluid weight coming from the re-entrant quantum geometric properties, and in the flat topological bands this contribution is significant. Due to the strong quantum geometry of the TBG flat bands in integer flux ($\sum_{\mathrm{BZ}}\mathrm{Tr}\mathscr{G}_{ij}\approx3$), the estimated BKT temperature is in order of the gap $T_*\approx\Delta$, which gives values significantly elevated with regard to the conventional superconductivity in geometrically-trivial dispersive bands. The behaviour of superfluid order parameter beyond the conventional magnetic thresholds (i.e. towards the integer magnetic flux) is a subject for further research.

6 Unconventional Flat Chern Bands and 2e Charges in Skyrmionic Moiré Superlattices

The interplay of topological characteristics in real space and reciprocal space can lead to the emergence of unconventional topological phases. In this Chapter, we implement a novel mechanism for generating higher-Chern flat bands on the basis of twisted bilayer graphene (TBG) coupled to topological magnetic structures in the form of the skyrmion lattice. In particular, we discover a scenario for generating $|C| = 2$ dispersionless electronic bands when the skyrmion periodicity and the moiré periodicity are matched. Following the Wilczek argument, the statistics of the charge-carrying excitations in this case is *bosonic*, characterized by electronic charge $Q = 2e$, that is *even* in units of electron charge e. The required skyrmion coupling strength triggering the topological phase transition is realistic, with its threshold estimated as low as 4 meV. The Hofstadter butterfly spectrum of this phase is different resulting in an unexpected quantum Hall conductance sequence $\pm\frac{2e^2}{h}$, $\pm\frac{4e^2}{h}$, ... for TBG with skyrmion order.

This Chapter discusses the effect of spin Skyrmions on the topology of TBG. It is adapted from the paper:
Yifei Guan, Oleg V. Yazyev, Alexander Kruchkov
Unconventional Flat Chern Bands and 2e Charges in Skyrmionic Moiré Superlattices
Nano Lett. 2023, 23, 10, 4209–4215 (2023)

My contribution to the work includes: building the tight-binding models for TBG with skyrmion spin texture, performing the calculations of the topological phase diagram and Wannier diagrams.

6.1 Introduction

The interplay between the real- and momentum-space topologies is a new direction in exploring interacting topological phases of matter. Generically, the band topology was introduced in condensed matter physics through the quantum-Hall-like arguments (Thouless *et al.*, 1982, Haldane, 1988), which are typically insensitive to the real-space defects. Nevertheless, it later became clear in the context of quantum Hall ferromagnetism that the coexistence of real-space topology (skyrmions) and momentum-space topology (Chern numbers) is possible for the flat bands (Sondhi *et al.*, 1993, Fertig *et al.*, 1994). More broadly, the question can be formulated in the form: Can the real space topology influence the change in the momentum space topology? The answer is positive; (Lux *et al.*, 2021) and we provide a concrete example of a realistic system.

The skyrmions have been called upon to explain possible pairing mechanisms in twisted bilayer graphene (TBG) and similar heterostructures (Khalaf *et al.*, 2021, Chatterjee *et al.*, 2020), see also Refs. (Zhang and Senthil, 2019, Abanov and Wiegmann, 2001, Grover and Senthil, 2008). In particular, the skyrmion-based theories are able to address not only the problem of possible mechanism for unconventional superconductivity in TBG (Cao *et al.*, 2018a), but also provide reasonable explanation (Chatterjee *et al.*, 2020) for nonmonotonic magnetoresistance observed in experiments (Sharpe *et al.*, 2019, Serlin *et al.*, 2020). Thus, the coexistence of the skyrmion order and the moiré potentials, to one or another extent, seems feasible. Since this is a consistent theoretical mechanism, we ask the following question: What is the effect of the skyrmion order on the TBG flat bands themselves?

The topological flat bands can induce a non-collinear magnetic order, such as skyrmions (Fertig *et al.*, 1997). In general, however, the skyrmion excitations are neither bosonic, nor fermionic, and reshape themselves continuously between the two opposite quantum statistics (Wilczek and Zee, 1983). It can be shown that excess *electric charge* density $\rho(\mathbf{r})$, polarized by the presence of a skyrmion $\mathbf{S}(\mathbf{r})$ on a flat Chern band is given by (Sondhi *et al.*, 1993, Abanov and Wiegmann, 2001, Hsu and Chakravarty, 2013)

$$\rho(\mathbf{r}) = Ce\frac{\mathbf{S}\cdot(\partial_x\mathbf{S}\times\partial_y\mathbf{S})}{4\pi}, \tag{6.1}$$

where C is the Chern number of the underlying electronic band. Upon integration over the unit cell one obtains

$$Q = C\mathscr{W}e, \tag{6.2}$$

where $\mathscr{W}$ is the skyrmion winding number (an integer). Thus, skyrmions polarize a discrete electric charge when the underlying flat band is topological.

The collective effect of the real-space and momentum-space topologies in mechanism (6.2) plays an important role. Indeed, the effective magnetic field, assigned to the skyrmion $B(\mathbf{r}) \propto \mathbf{S}\cdot(\partial_x\mathbf{S}\times\partial_y\mathbf{S})$ in (6.1) is essentially the Berry field (Nagaosa and Tokura, 2013). In momentum space, the gluing mechanism (6.2) can be rewritten as

$$\rho(\mathbf{q}) = e\sum_{\mathbf{k}} c^{\dagger}_{\mathbf{k}+\mathbf{q}}c_{\mathbf{k}} = \mathscr{W}\frac{F_{xy}}{2\pi}, \tag{6.3}$$

where F_{xy} is the Berry curvature associated with the Chern band, $C = \frac{1}{2\pi}\int_{\mathrm{BZ}} F_{xy}dk_x dk_y$. Thus,

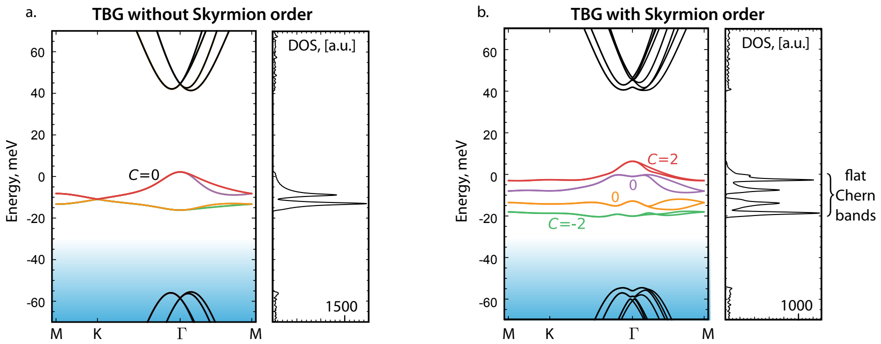

Figure 6.1 – Unconventional Chern flat bands of $|C| = 2$ in twisted bilayer graphene matched with the skyrmion lattice. (a) Band structure and density of states (DOS) of magic-angle TBG without skyrmion order. The associated Chern number is zero. (b) The inclusion skyrmion order ($m_0 = 4$ meV, $\mu = 8$ meV) results in flat Chern bands with $|C| = 2$.

according to Eq. (6.3), it is possible to have an unconventional electronic pairing mechanism induced by the skyrmion order when electrons are moving in the Chern band. This has been recently pointed out in the models of skyrmionic superconductivity in TBG (Khalaf *et al.*, 2021, Chatterjee *et al.*, 2020), where unconventional pairing mechanism is resulting from the skyrmions in the pseudospin space built upon reshuffling intrinsic $C = +1$ and $C = -1$ sectors (Khalaf *et al.*, 2021). However, a different situation is possible if the moiré system develops a flat band of a *higher* Chern number. Namely, in the $C = 2N$ case, the electric charge polarized by the skyrmion is

$$Q = 2N\mathscr{W} e, \tag{6.4}$$

that is *bosonic*. In other words, in case of $|C| = 2$ electron pairs are preformed independently of mechanism developed in Ref. (Khalaf *et al.*, 2021). In this work, we show that the flat bands in TBG acquire even Chern numbers $|C| = 2$ when electrons are firmly coupled to the underlying skyrmion lattice.

6.2 Underlying skyrmion lattice

The calculations below are independent of a particular origin of the skyrmion lattice (SkL), and can be applied to both (i) the case of proximity to a substrate hosting skyrmion lattice, or (ii) the case of spontaneous formation of skyrmion lattice in the moiré system. In the former scenario (i), the periodicity of SkL $\lambda_{\text{SkL}} = J/2D$ dictated by the interplay of Heisenberg (J) and Dzyaloshinskii-Moriya (D) interactions can be engineered (Tokura and Kanazawa, 2020) to match the periodicity of the moiré superlattice of TBG ($a_{\text{M}} = 12.9$ nm at the magic angle $\theta = 1.08°$). The later scenario (ii), represented by the SkL forming as a result of instability associated with the flat band, is supported by recent theoretical calculations (Wu and Sarma, 2020, Bömerich *et al.*, 2020). At $\nu = 3/4$ filling of the conduction band, TBG has been reported to exhibit giant spontaneous magnetism, resulting from internal Berry fields of the band

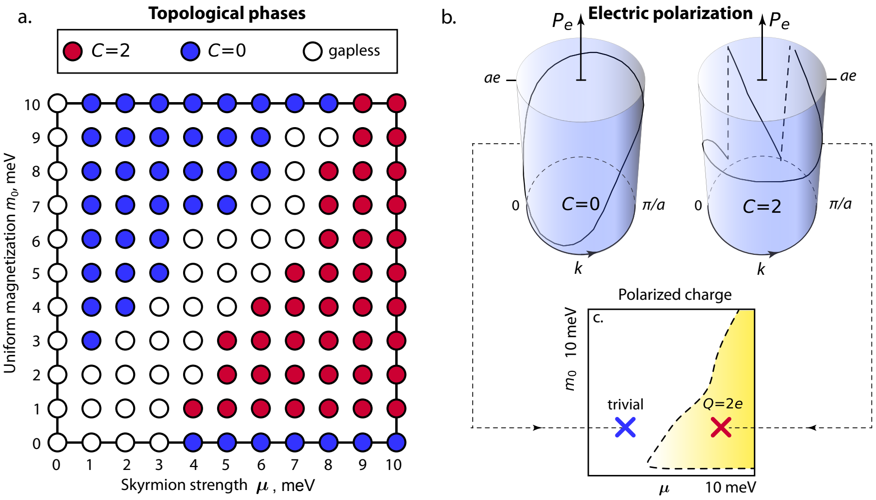

Figure 6.2 – (a)Phase diagram of flat Chern band phases in twisted bilayer graphene with the skyrmion order. We see that at the low skyrmion field the topologically–trivial phases are energetically preferred. However, at higher skyrmion fields, the phase diagram shows a remarkable new phase of $C = 2$ flat composite bands. (b) The calculated electric polarization of the different TBG phases with skyrmion lattice, see Eq. (6.10). The numerical parameters used: $\mu = 8$ meV, $m_0 = 4$ mev ($C = 2$ cylinder) and $\mu = 2$ meV, $m_0 = 4$ mev ($C = 0$ cylinder). (c) Sketched phase volume depicting the polarized charge 2e (in units of Fig. 6.2a).

structure, that is orbital in nature (Sharpe *et al.*, 2019, Serlin *et al.*, 2020). It is interesting that the TBG flat band can be viewed as a Landau level in non-homogeneous magnetic field (Tarnopolsky *et al.*, 2019, Popov and Milekhin, 2021, San-Jose *et al.*, 2012), and this real-space Berry field has strong inhomogeneities of the same periodicity as the patern moiré potential (Ledwith *et al.*, 2020). Thus, the resulting SkL instability, if allowed by the mechanism of Ref. (Wu and Sarma, 2020), will naturally inherit the same periodicity as the pristine TBG moiré superlattice. In what follows below, we consider the skyrmion lattice matched with the periodicity of TBG, but similar principles can be applied to other moiré heterostructures.

6.3 Band structure and unconventional Chern flat bands

We start by addressing the effect of skyrmion order on the band structure of TBG. We demonstrate that the skyrmion lattice, when being *commensurate* with the moiré periodicity a_{M} at the first magic angle, changes the electronic response of the system beyond recognition. We define the underlying SkL as (Nagaosa and Tokura, 2013, Mühlbauer *et al.*, 2009)

$$\mathbf{m}(\mathbf{r}) = \mathbf{m}_0 + \mu \sum_{j=1}^{3} (\mathbf{S}_{\mathbf{b}_j} e^{i\mathbf{b}_j \cdot \mathbf{r}} + \mathbf{S}_{-\mathbf{b}_j} e^{-i\mathbf{b}_j \cdot \mathbf{r}}), \tag{6.5}$$

where m_0 is the uniform magnetization component, μ the SkL strength and reciprocal vectors $\mathbf{b}_1 = \mathbf{q}_2 - \mathbf{q}_1$, $\mathbf{b}_2 = \mathbf{q}_3 - \mathbf{q}_1$, $\mathbf{b}_3 = \mathbf{q}_3 - \mathbf{q}_2$ are the same for the SkL and the moiré superlattice (here $\mathbf{q}_1 = k_\theta(0,-1)$, $\mathbf{q}_{2,3} = k_\theta(\pm\sqrt{3}/2, 1/2)$, with moiré wave number $k_\theta = 2k_D \sin\frac{\theta}{2}$, k_D being Dirac momentum of the monolayer graphene and θ being the twist angle). For the considered ranges of parameters $m_0, \mu = 0..10$ meV, the effective local magnetic fields are sufficient to modify the band structure (Fig. 6.1) and promote unconventional Chern phases (Fig. 6.2).

We focus our attention on the effect of the underlying skyrmion order (6.5) on the electronic band structure of TBG at the magic angle $\theta = 1.08°$. We have first confirmed this effect within the continuum model, and then performed the tight-binding model calculations for spinful electrons on a magic-angle TBG configuration that takes into account lattice relaxation effects. To the main approximation, the hopping amplitudes are barely affected by the real-space magnetic order. Hence on the tight-binding level the effect of local magnetization enters the Hamiltonian as on-site exchange field terms on each atom. In the basis $(\psi_i^\uparrow, \psi_i^\downarrow)$ the exchange field reads as $H_\mathrm{S} = \boldsymbol{\sigma}\cdot\mathbf{m}(\mathbf{r}_i)$, where $\boldsymbol{\sigma} = (\sigma_x, \sigma_y, \sigma_z)$ are the conventional 2×2 Pauli matrices. At atomic position $\mathbf{r}$, the on-site Hamiltonian term from the skyrmion order is

$$H_\mathrm{os}(\mathbf{r}) = \begin{pmatrix} 1 & 0 \\ 0 & 1 \end{pmatrix} V(\mathbf{r}) + \begin{pmatrix} 0 & 1 \\ 1 & 0 \end{pmatrix} \mu_x(\mathbf{r}) + \begin{pmatrix} 0 & -i \\ i & 0 \end{pmatrix} \mu_y(\mathbf{r}) + \begin{pmatrix} 1 & 0 \\ 0 & -1 \end{pmatrix} [\mu_z(\mathbf{r}) + m_0], \tag{6.6}$$

where we distinguish between the uniform magnetization ($m_0 = \langle \mathbf{m}(\mathbf{r}) \rangle$) and the skyrmion order itself $\boldsymbol{\mu} = \mathbf{m}(\mathbf{r}) - \mathbf{m}_0$. The overall real-space magnetic phase is approximated by

$$\mathbf{m}(\mathbf{r}) = \mathbf{m}_0 + \mu \sum_{j=1} (\mathbf{S}_{\mathbf{q}_j} e^{i\mathbf{q}_j\cdot\mathbf{r}} + \mathbf{S}_{-\mathbf{q}_j} e^{-i\mathbf{q}_j\cdot\mathbf{r}}), \tag{6.7}$$

where for the skyrmion lattice it is sufficient to cut the Fourier terms by the first triade $\mathbf{q}_1 + \mathbf{q}_2 + \mathbf{q}_3 = 0$, with $|\mathbf{q}_i|$ commensurate with moiré periodicity. Adding such on-site terms on each orbital, the full spinful Hamiltonian with the underlying skyrmion order reads

$$H = H_\mathrm{hop} + H_\mathrm{os} = \sum_{i\neq j} t_{ij}\sigma_0 + \sum_i \sigma_0 V_i \tag{6.8}$$

$$+ \sum_i \sigma_x \mu_x(r_i) + \sigma_y \mu_y(r_i) + \sigma_z[\mu_z(r_i) + m_0]. \tag{6.9}$$

Since the atomic relaxation has an effect on the interlayer coupling in AA and AB stacking region, and has dramatic effects on band flatness in TBG, we build the tight-binding hamiltonian based on the relaxed atomic structures. The atomic structure relaxation is done with classical potential on the LAMMPS package (Plimpton, 1995). Further details of the Slater-Koster models are provided in Sec. 2.3.

Figure. 6.1a compares the electronic band structure of TBG without the skyrmion order with that (Fig. 6.1b) for a representative case characterized by $m_0 = 4$ meV and $\mu = 8$ meV. Importantly, these parameters result in the $Q = 2e$ phase as shown in phase diagram in Fig. 6.2a. In absence of SkL ($m_0 = 0$ meV, $\mu = 0$ meV) magic-angle TBG has 8 flat bands near the Fermi level isolated from remote bands (Fig. 6.1a). At the K point of mini Brillouin zone, the flatband manifold has degenerate Dirac-like band crossing with renormalized Fermi velocity, while the degeneracy at the Γ point due to the spin and valley degrees of freedom. Introducing the uniform magnetization ($m_0 \neq 0$) lifts the spin degeneracy splitting the flat band manifold into 2 groups, while leaving intact the degeneracy at the Dirac points. In the presence of skyrmion order ($\mu \neq 0$), the spin-orbit terms couple the spin with the bands opening gaps at points K and K' and contributing to the hybridization of flat bands at the Γ point (Fig. 6.1b). In this case, the 8 flat bands decompose into 4 doubly degenerate sub-bands, which remain significantly flat. Employing the band flatness criterion of Bistritzer and MacDonald (Bistritzer and MacDonald, 2011b) (renormalized Fermi velocity v_F the at the K point), we observe that these bands become very flat in the K, K' valleys ($v_F = 3.3 \times 10^4$ m/s without SkL vs. $v_F = 2 \times 10^2$ m/s with SkL). For comparison, the overall bandwidths in TBG with SkL are significantly lower than in the pristine TBG case (5.3 mev, 13 meV in pristine TBG and 2.7 meV, 5 meV, 8.5 meV, 9.3 meV in TBG with SkL, given in ascending bandwidth order). Importantly, the density of states (DOS) remains significant upon adding SkL term (Fig. 6.1), thus enabling strong correlations. To quantify the the band flatness further, we investigate the band flatness criterion in terms of wave functions (Kruchkov, 2021). We thus confirm that upon adding the SkL term, the flat bands remain well-defined with clear real-space localization resulting into significant electronic density of states (Fig. 6.1b), with two of the resulting flat Chern bands having the high Chern number $|C| = 2$. Thus, non-collinear spin texture of skyrmion lattice coupled to charge-carrier in twisted bilayer graphene modifies its original band structure, but preserves the flatness in the atomistic model with lattice relaxations We now proceed to the effect on band topology.

6.4 Skyrmion-induced band topology and the phase diagram

The pristine TBG has band structure with hidden Chern numbers $C = \pm 1$ per valley that sum up to zero Chern number in total. Thus, in absence of skyrmion lattice or explicit symmetry breaking, TBG is not expected to demonstrate Chern indices of the composite flat bands (i.e. $m_0 = \mu = 0$ meV in phase diagram shown in Fig. 6.2a is topologically trivial). In what follows below, we discuss the half-filling of the conduction and valence bands ($\nu = 3/4$ and $\nu = 1/4$ fillings of the 8 moiré flat bands, respectively), motivated by the experimentally relevant filling $\nu = 3/4$ (see e.g. Ref. (Sharpe *et al.*, 2019)). The formalism of hybrid Wannier functions (HWFs) (Soluyanov and Vanderbilt, 2011) is employed to calculate the positions of the Wannier charge centers (WCC). This formalism gives us advantage of both addressing the Chern numbers as the winding of WCC on the cylinder (see Fig. 6.2b), and linking the nontrivial winding to electric polarization: The sum of all Wannier charge centers $\langle W_n^h | \mathbf{r} | W_n^h \rangle$ is gauge-invariant (mod lattice constant), and relates to the electric polarization of the system (Coh and Vanderbilt, 2009, King-Smith and Vanderbilt, 1993, Resta, 1993)

$$P_e = e \sum_n \langle W_n^{(h)} | \mathbf{r} | W_n^{(h)} \rangle. \tag{6.10}$$

Upon including the skyrmion order the $C = 2$ phase exhibits $\Delta P_e = 2ea$, witnessed through the polarized charge $2e$. For definiteness, in Fig. 6.2a and the text below, the phase diagram

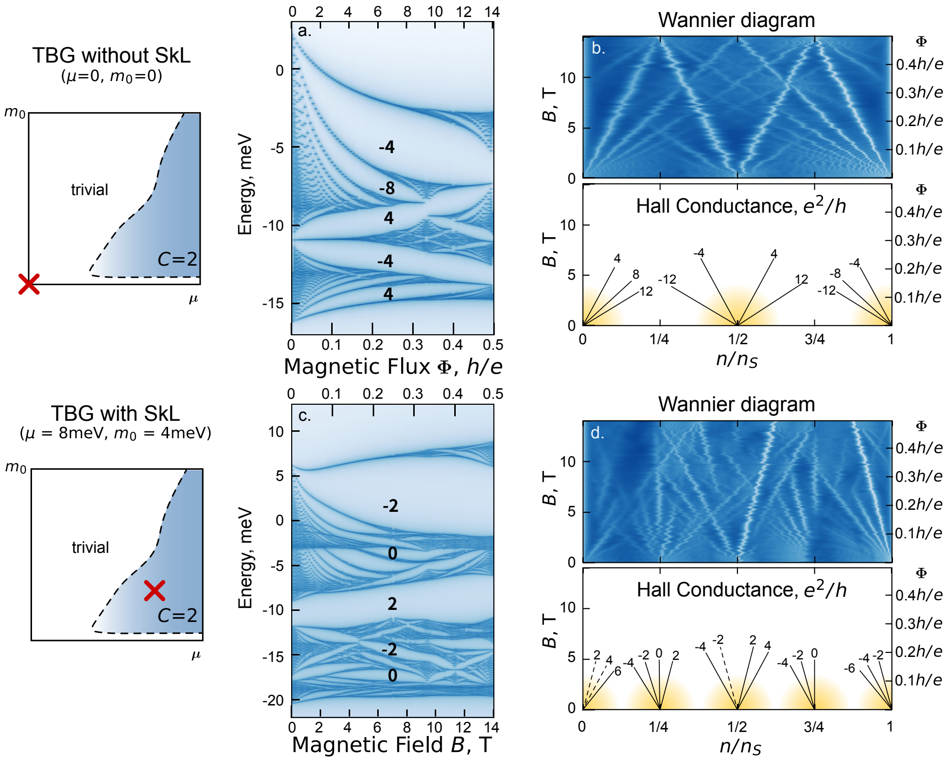

Figure 6.3 – Hofstadter and Wannier diagrams of TBG without and with the skyrmion order. (a) Hofstadter and (b) Wannier diagrams of twisted bilayer graphene without the skyrmion order. (c) Hofstadter and (d) Wannier diagrams of twisted bilayer graphene with the skyrmion order. We clearly see a different pattern of gaps and Chern numbers, attributed to the magnetic-field responds of a flat Chern band (see main text). All calculations are performed with the tight-binding model accounting for atomic relaxations of TBG. Here $n_S = 8$ (total bands) and $\Phi_0 = h/e$.

traces the total Chern number at $\nu = 3/4$, that is of the lowest three composite flat bands, which is the same in absolute value as the Chern number of the upper composite flat band, in the range from 0 to 10 meV for both the uniform component m_0 and the skyrmion strength μ. This range is dictated by the typical bandwidth scale in the system. Larger values of m_0 (over 20 meV) drives the flat bands to overlap with remote bands and destroys the separation condition of the flat bands, while μ does not induce the overlap explicitly.

The phase diagram in Figure 6.2a can be divided into three parts: two topologically-trivial phases (gapped $C = 0$ phase and gapless phase denoted "gapless" for which the Chern numbers cannot defined). Below the critical value $\mu \approx 4$ meV, the system remains in one of the trivial phases. Upon increasing the skyrmion strength above $\mu = 4$ meV, the new topological phase with $C = 2$ emerges. This phase, however is possible if only both μ and m_0 are finite: As shown in Fig. 6.2a, the WCC winding is zero when $m_0 = 0$. One can find a tiny band gap near the Γ point at $m_0 = 0$, in which the Chern number is zero. However, a weak ferromagnetic component $m_0 \ll \mu$ is sufficient to drive the system into the $C = 2$ phase, provided the skyrmion strength with $\mu > 4$ meV. On the other hand, the ferromagnetic component m_0 does not contribute to the finite Chern number itself, since in the region $\mu < 4$ meV the total Chern number is always zero (or undefined as a consequence of gaplessness). We highlight that the skyrmion strength of 4 meV is a realistic value, comparably smaller than the bandwidth itself, and a small uniform magnetization turns the system into a higher-Chern topological phase.

6.5 Hofstadter spectra

Another qualitative difference of the system with skyrmionic order can be traced in the response to the magnetic field. In this connection, the established apparatus involves the Hofstadter butterfly spectrum, which depicts the evolution of Landau levels in the system versus magnetic flux (Hofstadter, 1976). The Hofstadter butterfly spectra, together with the Wannier diagrams (Wannier, 1978), provide a comprehensive and sensitive map of the Chern numbers, and is directly linked to the observable quantum Hall conductance sequences (Dean *et al.*, 2013, Hunt *et al.*, 2013, Ponomarenko *et al.*, 2013). In Figure 6.3, we show the difference between the magnetic field response of magic-angle TBG with and without the skyrmion order. For the skyrmion-free TBG, the Landau levels at small magnetic fluxes are clearly recognizable, and their field-dependence in the limit of low field is consistent with the behavior of Dirac electrons scaling as $\sqrt{B}$ (Fig. 6.3a). In this limit, the Hofstadter spectrum is energetically bound to the bandwidth of the original flat band, which is expected for the trivial phase (Herzog-Arbeitman *et al.*, 2020). Upon increasing the magnetic flux, a moderate broadening of the Landau levels is observed, while sufficiently large gaps separate low-index Landau levels.

The situation changes dramatically upon including the skyrmion order (Fig. 6.3c; for $m_0 = 4$ meV and $\mu = 8$ meV). First of all, the low-field behavior is no longer recognizable as a simple $\sqrt{B}$ behavior since the Dirac physics is no longer relevant in this case. Instead, the behavior is qualitatively consistent with universal response of a Chern band to magnetic fields (Herzog-Arbeitman *et al.*, 2020). A different pattern of pronounced gaps emerges upon increasing the flux. The broadening and hybridization between sub-bands is promoted, leading to a more complex butterfly structure. We observe that the Hofstadter spectrum of the flat band is not bounded by the bandwidth of the original flat band, and can hybridize with other bands, which in turn trivializes the band topology leading to $C = 0$ gaps. Importantly, the particle-hole asymmetry is pronounced, which results in the particle-hole asymmetric Wannier diagrams and asymmetric Hall response. Since the TBG with SkL host a Chern band characterized by $C = 2$, we observe a different pattern of in-gap Chern numbers, as indicated in Fig. 6.3c. In order to draw the quantitative difference between these two cases, we proceed to the analysis of the Wannier diagrams.

Table 6.1 – Summary of quantum Hall conductance sequences at neutrality.

TBG (C_3 symmetric)	$\pm4\frac{e^2}{h}$, $\pm12\frac{e^2}{h}$, ...
TBG+SkL ($C=0$ phase)	$\pm4\frac{e^2}{h}$, $\pm8\frac{e^2}{h}$, ...
TBG+SkL ($C=2$ phase)	$\pm2\frac{e^2}{h}$, $\pm4\frac{e^2}{h}$, ...
TBG experiments	$\pm2\frac{e^2}{h}$, $\pm4\frac{e^2}{h}$, ... + further sample-dependent.

6.6 Hall conductance sequences

The Wannier diagram (Wannier, 1978) is obtained from the Hofstadter butterfly spectrum by presenting the statistical weight of the states below a given gap versus the magnetic flux. Each line in the Wannier diagram depicts a gap in the Hofstadter butterfly spectrum, while its slope characterizes the in-gap Chern numbers ($dn/dB = Ce/h$). In Figs. 6.3b,d we plot the Wannier diagrams that correspond to the respective Hofstadter spectra shown in Figs. 6.3a,c. To facilitate the analysis, we overlay the lines that trace the minimal intensities in the Wannier diagrams (Fig. 6.3c,d). We find that for pristine TBG with the preserved C_3 symmetry, the relevant Hall conductance sequence is $\pm4\frac{e^2}{h}$, $\pm12\frac{e^2}{h}$, ..., that is in increments of 8 conductance quanta (Zhang, 2019). On contrary, the presence of skyrmion order changes the Hall sequence dramatically. For the TBG with SkL in the $C=2$ phase, the Hall conductance "fingerprint" (Fig. 6.3) at neutrality reads

$$G_{\mathrm{TBG}}^{\mathrm{SkL}} = \pm\frac{2e^2}{h},\ \pm\frac{4e^2}{h},... \tag{6.11}$$

One might be tempted to interpret these results as a trivial lifting of the spin degeneracy by the uniform component m_0 of the skyrmion phase. However, we observe that by changing the skyrmion parameters to $m_0 = 4$ meV and $\mu = 2$ meV, for which the system is in the $C=0$ phase (see Fig. 6.2a), a different Hall sequence $\pm4\frac{e^2}{h}, -8\frac{e^2}{h}$ is obtained, even though the system still has the same uniform magnetization m_0. Instead, we believe that this effect is connected to the fundamentally different Hosftadter spectrum for the trivial and Chern bands, and hence, Wannier diagrams. The obtained results are summarized in Table I. Wannier diagrams can be directly probed in experiment by performing Shubnikov–de Haas measurements on high-quality magic-angle TBG samples (Lu *et al.*, 2019). We remark that the experimentally observed QH sequences are strongly sample-dependent,[1] however the two leading contributions to the low-field Landau fans can be considered as $\pm2\frac{e^2}{h}$, $\pm4\frac{e^2}{h}$. It is certainly interesting that TBG with

---

[1] The question of the Landau fan (LF) in TBG is a hard one. The original studies (Cao *et al.*, 2018a) reported the Hall sequence, in units e^2/h: ±4, ±8, ±12 at neutrality, instead of expected ±4, ±12... (Moon and Koshino, 2012), thus puzzling theorists. The consequent experiments (Lu *et al.*, 2019) on more homogeneous samples brought even further surprise with the QH sequence ±2, ±4, ±8. Moreover, LF with ±2, ±4 was reported in Ref. (Sharpe *et al.*, 2019); LF with ±2, ±4, ±6 was reported in TBG stabilized by WSe_2; (Arora *et al.*, 2020) and LF with −2, −4 in the sample of Ref. (Pierce *et al.*, 2021). For the high-field behavior of Landau fans, we refer readers to the recent observation of correlated Chern insulators in TBG e.g. in Refs. (Pierce *et al.*, 2021, Xie *et al.*, 2021)

SkL in the $C = 2$ phase (but not the $C = 0$ phase) gives a reasonable Hall sequence, without demanding C_{3z} or C_{2z} breaking (Zhang, 2019).

6.7 Conclusion

In this Chapter, we considered the influence of the real-space skyrmionic order on the dispersion and topology of flat bands. For the particular example of magic-angle twisted bilayer graphene, we find that the commensurate skyrmionic order itself redefines both the band structure and topology of the system. Surprisingly, the real-space skyrmion order influences the electronic bands topology, giving the rise to an unexpected $C = 2$ phase. To our knowledge, this is the first realistic system which provides a robust and affirmative answer to the question of the interplay between topologies in real and reciprocal spaces (Lux *et al.*, 2021). According to the field-theoretical arguments (Sondhi *et al.*, 1993, Abanov and Wiegmann, 2001, Hsu and Chakravarty, 2013), the elementary excitations in this case are $Q = 2e$, a consequence important for the transport phenomena in twisted bilayer graphene. Experimentally, the reported effect manifests in magnetotransport observables with the leading quantum Hall sequence $\pm 2\frac{e^2}{h}$, $\pm 4\frac{e^2}{h}$. This Landau fan fingerprint resonates well with experimental reports, and arises naturally in our model as a direct consequence of the emergent skyrmion order.

7 Landau Levels as a Probe for Band Topology in Graphene Moiré Superlattices

We propose Landau levels as a probe for topological character of electronic bands in two-dimensional moiré superlattices. We consider two configurations of twisted double bilayer graphene (TDBG) that have very similar band structures, but show different valley Chern numbers of the flat bands. These differences between the AB-AB and AB-BA configurations of TDBG clearly manifest as different Landau level sequences in the Hofstadter butterfly spectra calculated using the tight-binding model. The Landau level sequences are explained from the point of view of the distribution of orbital magnetization in momentum space that is governed by the rotational C_2 and time-reversal $\mathscr{T}$ symmetries. Our results can be readily extended to other twisted graphene multilayers and h-BN/graphene heterostructures thus establishing the Hofstadter butterfly spectra as a powerful tool for detecting the non-trivial valley band topology.

This Chapter reveals the effect of band topology on the Hofstadter butterfly spectra. It is adapted from the paper:

QuanSheng Wu, Jianpeng Liu, **Yifei Guan**, and Oleg V. Yazyev
Landau Levels as a Probe for Band Topology in Graphene Moiré Superlattices
Phys. Rev. Lett. 126, 056401 (2021)

in which my contributions are: implementing the computational algorithms of Landau gauges for calculating the Hofstadter butterfly.

7.1 Introduction

The recent discovery (Cao *et al.*, 2018a,b, Lu *et al.*, 2019, Chen *et al.*, 2019, Burg *et al.*, 2019, Shen *et al.*, 2020) of correlated insulating phases, unconventional superconductivity, and quantum (Serlin *et al.*, 2020) anomalous Hall effect (Sharpe *et al.*, 2019, Liu *et al.*, 2019d, Bultinck *et al.*, 2020) in twisted bilayer graphene (TBG) and related moiré superlattices have drawn widespread attention from in theoretical and experimental physics communities. In these twisted graphene multilayers, the width of the four-band manifold around the charge neutrality point (CNP) vanishes at the so-called “magic” angle (Bistritzer and MacDonald, 2011b, Suárez Morell *et al.*, 2010). These flat bands often have non-trivial topology such as the recently proposed fragile topology (Song *et al.*, 2019b, Po *et al.*, 2019, Ahn and Yang, 2019). Although the physical mechanisms underlying the observed novel correlated phases are still under debate, the small bandwidth and the non-trivial topology of the relevant bands are certainly pointing to new, interesting physics. However, directly probing the topological properties in experiments is difficult due to their “hidden” nature: the topological properties of the two valleys intrinsic to the electronic structure of these systems would cancel each other provided that valley degeneracy is preserved.

In this Chapter, we propose Landau levels as such a probe of the topological character of electronic bands in graphene moiré superlattices. We illustrate this idea using the example of twisted double bilayer graphene (TDBG), a system constructed by twisting two AB-stacked bilayer graphene (BLG) counterparts placed on top of each other. This more complex four-layer moiré heterostructure has recently revealed several novel properties such as the gap opening at large twist angles (Haddadi *et al.*, 2020, Adak *et al.*, 2020, Rickhaus *et al.*, 2019, Choi and Choi, 2019, Culchac *et al.*, 2020, Chebrolu *et al.*, 2019) and two types of stacking configurations that have distinct topological properties (Liu *et al.*, 2019d, Chebrolu *et al.*, 2019). Moreover, the band structure and topological properties of TDBG can be controlled by applying external electrical fields (Shen *et al.*, 2020, Liu *et al.*, 2019d, Chebrolu *et al.*, 2019, Lee *et al.*, 2020, Koshino, 2019), and could lead to quantum anomalous Hall effect when correlation effects are taken into account (Liu *et al.*, 2021).

7.2 Distinct configurations of TDBG

Two distinct configurations of TDBG referred to as AB-AB and AB-BA are related to each other by rotating the BLG counterparts by 180° with respect to each other. Both belong to the D_3 symmetry group, but differ by having the C_{2x} and C_{2y} symmetries, respectively. The band structures of the AB-AB and AB-BA configurations were found to be similar (Culchac *et al.*,

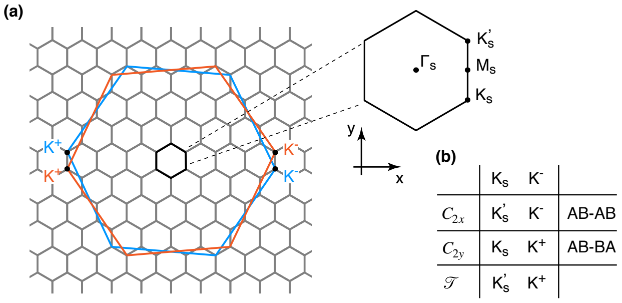

	K_s	K^-	
C_{2x}	K_s'	K^-	AB-AB
C_{2y}	K_s	K^+	AB-BA
$\mathscr{T}$	K_s'	K^+	

Figure 7.1 – (a) Brillouin zones of the two BLG components (orange and blue for top and botton bilayers, respectively) and moiré supercell (grey hexagons). (b) Change of valley momenta under rotational (C_{2x}, C_{2y}) and time-reversal ($\mathscr{T}$) symmetry operations.

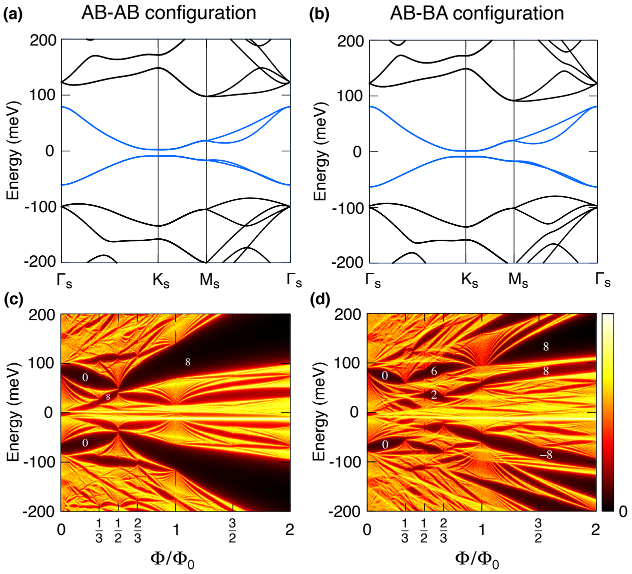

Figure 7.2 – (a,b) Band structures and (c,d) Hofstadter butterfly spectra of the AB-AB and AB-BA configurations of TDBG, respectively, characterized by twist angle $\theta = 1.89°$. The flat band manifold is shown in blue. The numbers in the HB spectra indicate the Chern numbers of the LLs gaps.

2020, Koshino, 2019), but the above-mentioned symmetry differences result in different band topologies. The C_{2x} symmetry requires the Chern number for each valley to be vanishing, while C_{2y} doesn't. The time-reversal symmetry requires the Chern numbers of the two valleys are opposite. Hence, the AB-AB configuration of TDBG has trivial valley Chern numbers, while the AB-BA configuration is topologically nontrivial. The Chern number is the integral of Berry curvature that affects the Landau level (LL) spectrum when magnetic field is applied (Chang and Niu, 2008, Sundaram and Niu, 1999). We show that the LL spectra of the AB-AB and AB-BA configurations of TDBG are dramatically different, which allows to discriminate them despite their virtually indistinguishable band structures.

7.3 Hofstadter's butterfly of TDBG and Wannier diagrams

The HB spectrum and LLs of TBG close to the magic angle have recently been investigated in several works (Lian *et al.*, 2018, Hejazi *et al.*, 2019, Zhang and Senthil, 2019). Lian *et al.* studied the HB of TBG, and found that the HB of the flat-band manifold is generically connected with the remote bands since the flat bands have non-trivial fragile topology (Lian *et al.*, 2018). Zhang *et al.* found that the degeneracy of the LLs would be lifted when the crystal symmetry is broken (Zhang and Senthil, 2019). In our work, we show that the distribution of orbital magnetization in momentum space can lift the LL degeneracy, and that the LL splittings are crucially dependent on the stacking configuration and band topology of the TDBG system.

The tight-binding (TB) Hamiltonian in presence of a magnetic field is obtained by adding phase factors ϕ_{ij} to the corresponding hopping integrals, a procedure known as the Peierls substitution (see Sec. 2.3), applied electric field and intrinsic polarization effects were not considered in the reported calculations. The phase factor ϕ_{ij} is in general not periodic modulo 2π in the usual Landau gauge $\mathbf{A} = Bx\hat{e}_y$ when $\mathbf{r}_i$ and $\mathbf{r}_j$ are not nearest neighbours. In order to cope with this problem, we adopt the periodic Landau gauge introduced by Nemec and Cuniberti (Nemec and Cuniberti, 2007) and further used by Hasegawa and Kohmoto (Hasegawa and Kohmoto, 2013) to study TBG. This periodic Landau gauge is defined as

$$\mathbf{A}(\mathbf{r}) = \frac{\Phi}{2\pi}\left((\xi_1 - \lfloor \xi_1 \rfloor)\mathbf{K_2} - \xi_2 \sum_{n=-\infty}^{\infty} \delta(\xi_1 - n + \epsilon)\mathbf{K_1}\right), \tag{7.1}$$

where (ξ_1, ξ_2) are the oblique coordinates defined by $\mathbf{r} = \xi_1\mathbf{R_1} + \xi_2\mathbf{R_2}$ with $\mathbf{R_1}, \mathbf{R_2}$ being the primitive vectors of the moiré unit cell, $\mathbf{K_1}$, $\mathbf{K_2}$ are the corresponding reciprocal lattice vectors, ϵ is a positive infinitesimal and $\lfloor x \rfloor$ is the floor function defined as largest integer not greater than x. Φ is the magnetic flux through the moiré unit cell defined as

$$\Phi = BS = \frac{p}{q}\Phi_0, \tag{7.2}$$

where S is the area of the moiré unit cell, p and q are co-prime integers. The size of magnetic supercell is q times the moiré unit cell along the $\mathbf{R}_2$ direction. The HB and LLs spectra, represented by the local density of states, are obtained by numerically solving the eigenvalue problem using the Lanczos recursion method as implemented in the WannierTools open-source software package (Wu *et al.*, 2018), and described in Sec. 2.7.

Without loss of generality, we will focus on TDBG with twist angle $\theta = 1.89°$, for which we set $q = 500$ in our calculations. As shown in Figs. 7.2a,b, the band structures of the AB-AB and AB-BA configurations are practically indistinguishable as far as the flat-band manifold is concerned. Figs. 7.2c,d show the HB spectra of these two TDBG configurations. It is evident that despite very similar band structures, the AB-AB and AB-BA configurations have very different HB spectra as well as Chern numbers associated with the LL gaps. The LLs of the flat bands are connected with the LLs originating from higher energy bands in both cases, which is observed also for smaller twist angles. Lian *et al.* (Lian *et al.*, 2018) attributed this to the nontrivial fragile topology of TBG. However, we note that no fragile topology and no valley Chern numbers characterize the AB-AB configuration of TDBG.

A convenient way for observing the HB in experiments relates to the Wannier diagrams (WDs) obtained by plotting the Hofstadter energy spectrum as integrated charge-carrier density n versus magnetic field B or magnetic flux Φ (Wannier, 1978). WDs show that all spectral gaps are constrained to linear trends in the density-field diagrams. This can be described by a simple Diophantine relation

$$n/n_s = t\Phi/\Phi_0 + s, \tag{7.3}$$

where n/n_s and Φ/Φ_0 are the normalized carrier density and magnetic flux, respectively, and

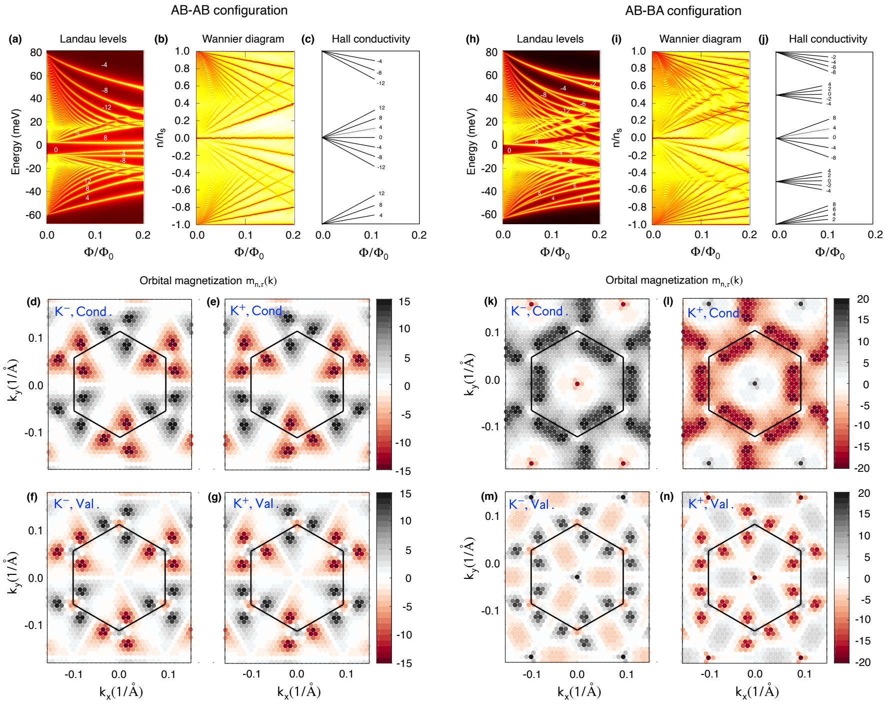

Figure 7.3 – Landau levels, Wannier diagrams, Hall conductivity and orbital magnetization plots for the flat-band manifold in the AB-AB (left) and AB-BA (right) configurations of TDBG at twist angle $\theta = 1.89°$. (a,h) The LL spectra as a function of magnetic flux per moiré unit cell. The valley Chern numbers of the LL gaps are indicated. (b,i) Normalized charge-carrier density per moiré unit cell as a function of magnetic field flux. The linear trends correspond to the gaps, hence the LL filling factors can be deduced from the slopes of these lines. (c,j) Quantized Hall conductivity of the Landau fans. Panels (d-g) and (k-n) show the orbital magnetization $m_{n,\tau}(\mathbf{k})$ in units of μ_B, where n is the band index representing conduction or valence bands and τ is the graphene valley index K^+ or K^-.

s and t are integer numbers. Here, n/n_s represents the Bloch band filling fraction. The first quantum number t is related to the Hall conductivity σ_{xy} associated with each minigap in the fractal spectrum. σ_{xy} is quantized according to the relation $\sigma_{xy} = 4te^2/h$, where factor 4 originates from the valley and spin degeneracies. The second quantum number s corresponds to the Bloch band filling index in the fractal spectrum.

In the limit of weak out-of-plane uniform fields $\mathbf{B} = (0, 0, B)$, the evolution of energy bands can be treated perturbatively as (Chang and Niu, 2008, 1996, Sundaram and Niu, 1999, Sun *et al.*, 2020)

$$\varepsilon_{n,\sigma,\tau}(\mathbf{k}, B) = \varepsilon_{n,\tau}(\mathbf{k}) + \mu_B g\sigma B + m_{n,\tau}(\mathbf{k})B, \tag{7.4}$$

where σ is the electron spin operator assuming $\pm 1/2$ values for up and down spins, respectively, and $\tau = \pm 1$ is the valley index. The valley orbital magnetization is defined as

$$m_{n,\tau}(\mathbf{k}) = -\mu_B \frac{2m_e}{\hbar^2} \mathrm{Im} \sum_{l \neq n} \frac{\langle n,\tau|\partial_{k_x}\mathscr{H}_\tau|l,\tau\rangle\langle l,\tau|\partial_{k_y}\mathscr{H}_\tau|n,\tau\rangle}{\varepsilon_{n,\tau,\mathbf{k}} - \varepsilon_{l,\tau,\mathbf{k}}}. \tag{7.5}$$

There are two contributions to the energy due to magnetic field. The first contribution originating from the Zeeman effect of electron spin is neglected throughout this work for simplicity. The second contribution is related to the orbital magnetization contribution $m_{n,\tau}(\mathbf{k})$.

The LL spectra, Wannier diagrams and the distribution of orbital magnetization in momentum space for the the flat-band manifold of the AB-AB and AB-BA configurations of TDBG at $\theta = 1.89°$ in a low-field range are presented in Fig. 7.3. In the case of Bernal (AB-stacked) BLG, the sequence of the Hall conductivity values $\sigma_{xy} = \pm 4, \pm 8, \pm 12, \ldots\ e^2/h$ (Novoselov *et al.*, 2006) with the increment of 4 e^2/h is related to the combination of the spin and (bilayer graphene) valley degeneracies. In TDBG, the moiré valley degeneracy adds to the above degeneraciers increasing the increment of the Hall conductivity sequence to 8 e^2/h. In our calculations, however, we observe the 4 e^2/h increment close to the CNP for both the AB-AB and AB-BA configurations of TDBG (Figs. 7.3c,j). This implies that one of three degeneracy flavors is lifted under applied magnetic field. Due to the neglected Zeeman effect term, either bilayer graphene valley or moiré valley degeneracies are expected to be lifted by magnetic field. In order to clarify this issue, we consider the transformations of orbital magnetization $m_{n,\tau}(\mathbf{k})$ under the C_{2x}, C_{2y} and T symmetries:

$$\begin{aligned} T: &\qquad m_n(\mathbf{k}) = -m_n(-\mathbf{k}), \\ C_{2x}: &\qquad m_n(k_x, k_y) = -m_n(k_x, -k_y), \\ C_{2y}: &\qquad m_n(k_x, k_y) = -m_n(-k_x, k_y). \end{aligned}$$

In the AB-AB configuration of TDBG, the C_{2x} symmetry operation exchanges moiré valleys K_s and K_s' while keeping the bilayer graphene valleys K^+ and K^- unchanged (Fig. 7.1). Eventually, the orbital magnetization $m_{n,\tau}(\mathbf{k})$ is the same for the two bilayer graphene valleys while it is opposite in the two moiré valleys. The orbital magnetization $m_{n,\tau}(\mathbf{k})$ of the conduction and valence bands for the two valleys, calculated using the continuum model Hamiltonian described in Ref. (Liu *et al.*, 2019d), is shown in Fig. 7.3d-g. The results are fully consistent with our symmetry analysis. The Landau levels at the CNP originate from the energy bands at the two moiré valleys K_s and K_s'. According to Eqn. (7.4), the LLs originating from moiré valleys K_s and K_s' are no longer degenerate due to their opposite orbital magnetization $m_{n,\tau}(\mathbf{k})$, while the LLs of the two bilayer graphene valleys preserve the degeneracy due to the same orbital magnetization. To support this argument, let us consider the lowest LL of the valence and conduction bands shown in Figs. 7.3a,b. The large splitting of the lowest LLs originating from the valence band contrasts with essentially no splitting for the conduction band LLs. This can be explained by the fact that $m_{n,\tau}(\mathbf{k})$ of the valence band at K_s and K_s' is about $\pm 6.5\mu_B$ while that of the conduction band is zero. To provide a rough estimate, the energy splitting at

$\Phi/\Phi_0 = 0.1$ (corresponds to $B \approx 9$ T) assuming a orbital magnetization of $6.5\mu_B$ is *ca.* 3.2 meV which is comparable to the lowest LL splitting of the valence band shown in Fig. 7.3a. Note that the orbital magnetization of the conduction band at K_s and K_s' is close to zero as shown in Figs. 7.3d,e. Eventually, the LL splitting of the conduction band close to CNP is much weaker than that of the valence band. For this reason, the splitting of the lowest LL of the conduction band at CNP is missing, which manifests in apparent absence of $\sigma_{xy} = 4\ e^2/h$ from the Hall conductivity sequence (Fig. 7.3c). The same scenario is also observed for the AB-BA configuration of TDBG discussed below. The LLs at $n/n_s = \pm 1$ originate from the Γ_s point where the orbital magnetization of the conduction and valence bands is zero due to the symmetry constrain. Eventually, as shown in Figs. 7.3a-c, the sequence of the LLs at $n/n_s = \pm 1$ is 0, ±4, ±8,... with increment of 4 originating from the combination of spin and bilayer graphene valley degeneracies.

In the AB-BA configuration of TDBG, the C_{2y} symmetry exchanges bilayer graphene valleys K^- and K^+ while keeping the moiré valleys unchanged. In this case, the orbital magnetization $m_{n,\tau}(\mathbf{k})$ shown in Figs. 7.3k-n is the same for the two moiré valleys, while it is opposite for the two bilayer graphene valleys. The latter indicates that the bilayer graphene valley degeneracy of LLs is lifted under magnetic field, as supported by Figs. 7.3h-j. The Hall conductivity sequence at CNP $n/n_s = 0$ is $\sigma_{xy} = 0, \pm 4, \pm 8, \dots\ e^2/h$, *i.e.* the same as for the AB-AB configuration. However, at $n/n_s = \pm 1$ the Hall conductivity sequence $\sigma_{xy} = 0, \pm 2, \pm 4, \dots\ e^2/h$ with increment of 2 e^2/h is different from that of the AB-AB configuration. Furthermore, another Landau fan at half-filling $n/n_s = 1/2$ can be observed, while it is absent in the case of AB-AB configuration of TDBG. This Landau fan at $n/n_s = 1/2$ appears when the degeneracy is lifted in the whole BZ.

In conclusion, through large-scale numerical calculations based on the atomistic tight-binding model and symmetry analysis, we have investigated the LL spectra of two configurations of TDBG with the same value of twist angle. It was found that the LL sequences close to the CNP of both systems are very similar although their origin is different, while the LL sequences at $n/n_s = \pm 1$ and $n/n_s = \pm 1/2$ of both systems are very different. These similarities and differences are caused by the momentum-space distribution of orbital magnetization $m_{n,\tau}(\mathbf{k})$ subject to symmetries. These considerations can be readily generalized to a broader class of moiré superlattice systems, such as other twisted graphene multilayers and h-BN/graphene heterostructures, characterized by flat bands with non-trivial valley Chern numbers. Our results thus suggest Landau levels as a versatile experimental probe for the "hidden" topological character of bands in two-dimensional moiré systems.

Part III

Quantum transport in graphene-based nanostructures

8 Electronic transport in graphene with out-of-plane disorder

Real-world samples of graphene often exhibit various types of out-of-plane disorder–ripples, wrinkles and folds–introduced at the stage of growth and transfer processes. These complex out-of-plane defects resulting from the interplay between self-adhesion of graphene and its bending rigidity inevitably lead to the scattering of charge carriers thus affecting the electronic transport properties of graphene. We address the ballistic charge-carrier transmission across the models of out-of-plane defects using tight-binding and density functional calculations while fully taking into account lattice relaxation effects. The observed transmission oscillations in commensurate graphene wrinkles are attributed to the interference between intra- and interlayer transport channels, while the incommensurate wrinkles show vanishing backscattering and retain the transport properties of flat graphene. The suppression of backscattering reveals the crucial role of lattice commensuration in the electronic transmission. Our results provide guidelines to controlling the transport properties of graphene in presence of this ubiquitous type of disorder.

This Chapter explores the influence of wrinkles and folds in the electronic transmission of graphene. The lattice matching effect in the wrinkle is extensively discussed.

This chapter is adapted from the paper:
Yifei Guan and Oleg Yazyev*
Electronic transport in graphene with out-of-plane disorder (2022)
https://arxiv.org/abs/2210.16629

My contribution includes developing the tight-binding transmission code, establishing the single atomic chain model and concluding the theory of momentum matching.

8.1 Introduction

Being the first and the most investigated two-dimensional (2D) material, graphene continues attracting attention as a platform for exploring novel physics and realizing prospective technological applications (Castro Neto *et al.*, 2009). The 2D nature of graphene gives rise to soft flexural modes that result in low-energy out-of-plane disorder otherwise absent in bulk, three-dimensional materials (Deng *et al.*, 2017, Mariani and Von Oppen, 2008, Croy, 2020, de Lima *et al.*, 2015). The interplay between bending upon in-plane compression and the interlayer adhesion results in several distinct types of out-of-plane disorder: ripples, wrinkles and folds (see Refs. (Zhu *et al.*, 2012, Deng *et al.*, 2017) and Figs. 8.1(a,b)). The out-of-plane disorder has a prominent effect on the electronic structure and transport properties of graphene (Hattab *et al.*, 2012, Xie *et al.*, 2012, Pelc *et al.*, 2015, Kang *et al.*, 2020). Finite curvature of the deformed region results in pseudo-gauge fields (Vozmediano *et al.*, 2008, Ortolani *et al.*, 2012), while the collapsed regions in wrinkles and folds provide a pathway for electronic tunnelling between layers (Zhu *et al.*, 2012, Benameur *et al.*, 2015). In addition, out-of-plane disorder locally accumulates charges and act as scattering centers (Zhu *et al.*, 2012, Guo and Guo, 2013, Pereira *et al.*, 2010, Nakajima *et al.*, 2019), subsequently having an impact on the operation of graphene-based nanoscale electronic devices (Benameur *et al.*, 2015, Katsnelson and Prokhorova, 2008, Zhang and Fahrenthold, 2020) as well as electrical characteristics of large-scale graphene samples.

Out-of-plane disorder in graphene may occur for several reasons. For instance, graphene grown using the chemical vapour decomposition (CVD) process develops wrinkles and folds as a result of the thermal contraction of substrate during the cooling stage (Deng and Berry, 2016, Wang *et al.*, 2021, Pan *et al.*, 2011). The out-of-plane disorder may also be introduced during the transfer procedure (Lanza *et al.*, 2013, Liu *et al.*, 2011). Significant efforts have then be devoted to eliminating wrinkles (Deng *et al.*, 2017, Wang *et al.*, 2021), e.g. using the substrates with matching thermal expansion coefficients (Lanza *et al.*, 2013), strain engineering (Hu *et al.*, 2021) and tailored temperature control protocols (Wang *et al.*, 2021). Experimental studies of the electronic transport in graphene with out-of-plane disorder have also been published (Zhu *et al.*, 2012, Ma *et al.*, 2020). It was proposed that controlled folding of graphene can be used for engineering charge-carrier dynamics (Fan *et al.*, 2021, Rode *et al.*, 2018, Luo *et al.*, 2022, Yang *et al.*, 2022). No question, future applications of graphene in electronics call for a detailed understanding of the effect of this ubiquitous type of disorder on the electronic transport.

In this work, we systematically investigate the electronic transport across wrinkles and folds in graphene using first-principle computations. For commensurate graphene wrinkles, in which the interlayer stacking corresponds to the energetically favorable Bernal stacking configuration, we find that the electronic transmission oscillates over wide energy ranges. The observed oscillation patterns are attributed to quantum interference between the inter- and intralayer transport channels. In incommensurate wrinkles and folds, the mismatch between the layers is found to suppresses the interlayer tunneling resulting in transmission probabilities close to the limit of flat, pristine graphene.

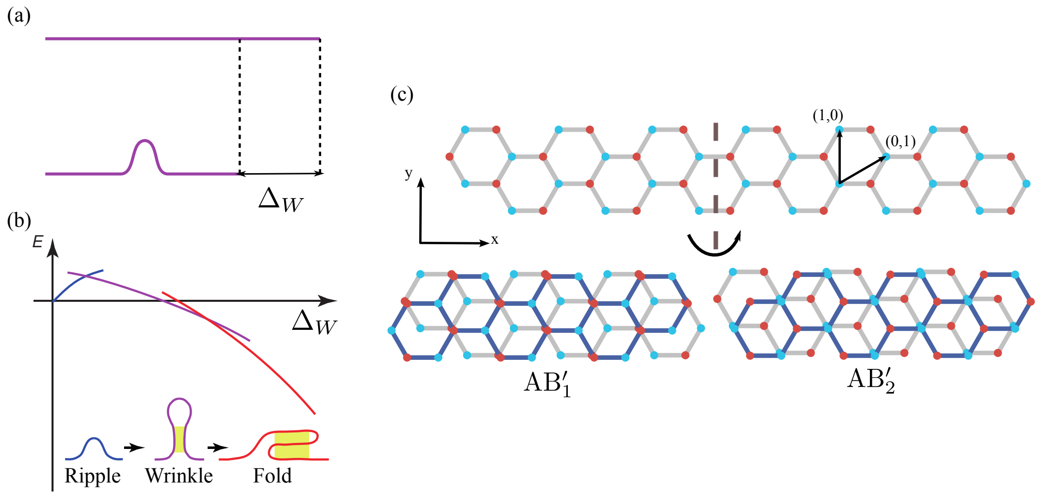

Figure 8.1 – The structure of out-of-plane disorder in graphene. (a) Definition of compressive displacement Δ_W relative to the flat, unstrained graphene. (b) Formation of the three distinct types of out-of-plane disorder upon increasing Δ_W. The curves show a schematic illustration of the dependence of energy E on Δ_W for the three deformation regimes. Yellow color exposes the collapsed regions where the interlayer coupling is enabled. (c) Illustration of the interlayer coupling between the atoms belonging to the same sublattice in commensurate zigzag wrinkles and folds.

8.2 Methodology

The atomistic models of graphene with out-of-plane disorder considered in our work are defined by a compressive displacement of length Δ_W (see Fig. 8.1(a)) forming a wrinkle or a fold along crystallographic vector $\mathbf{v} = (a, b)$. The considered configurations are thus assumed to be periodic along $\mathbf{v}$. The interplay between the bending energy and attractive interlayer interactions of graphene layers define the evolution across the three types of out-of-plane disorder realized upon increasing Δ_W as shown in Fig. 8.1(b). While ripples are formed at small Δ_W, interlayer attraction collapses such structures to wrinkles for larger values of Δ_W, and further increase of Δ_W leads to folds, in which the contact area between graphene layers is further increased. Extremities of wrinkles and folds have loop-like structures free of interlayer coupling (Zhu *et al.*, 2012). All atomistic models of wrinkles and folds considered in our work have been constructed with the help of classical force-field relaxation.

The atomic structures of models of the out-of-plane disorder in graphene were obtained by means of classical force field simulations using LAMMPS (Plimpton, 1995, LAMMPS). The classical force field includes the bond-order potential for describing covalent bonding (Los and Fasolino, 2003) as well as the modified version of the Kolmogorov–Crespi registry-dependent potential (Kolmogorov and Crespi, 2005) for describing the interlayer van der Waals interactions. The energy minimization was performed using the conjugate-gradient and fast inertial relaxation engine (FIRE) algorithms (Bitzek *et al.*, 2006).

First-principles transport calculations were performed with the TranSIESTA package (Soler *et al.*, 2002, Stokbro *et al.*, 2003). We used the double-ζ plus polarization basis set combined with the local density approximation exchange-correlation functional (Perdew and Zunger, 1981). The energy shift for constructing the localized basis was set to 275 meV, and the real-space cutoff to 250 Ry. The estimation of the direct coupling between the top and bottom layers in graphene folds was extracted from the localized basis set Hamiltonian using the sisl package (Papior, 2022).

8.3 Electronic transport across commensurate wrinkles

We first consider the special case of wrinkles defined by $\mathbf{v} = (1,0)$ and $\mathbf{v} = (1,1)$, referring to them as zigzag and armchair, respectively. The collapsed regions of such wrinkles are compatible with the energetically favorable Bernal interlayer stacking configuration (Gargiulo and Yazyev, 2018, Lipson and Stokes, 1942, Butz *et al.*, 2014, Ni and Wakabayashi, 2014), and hence referred to as commensurate in the rest of our paper. For these relaxed models, we calculated ballistic charge-carrier transmission from first principles, using the combination of density functional theory (DFT) and the non-equilibrium Green's function formalism implemented in the TranSIESTA package (Soler *et al.*, 2002, Stokbro *et al.*, 2003). The results of DFT calculations are discussed in comparison with the tight-binding (TB) approximation calculations employing the Slater-Koster formalism (Slater and Koster, 1954, Zhu *et al.*, 2012). Figures 8.2(a)-(d) present the ballistic transmission $T(E, k_{//})$ for the models of zigzag wrinkles defined by $\Delta_W = 40,\ 60,\ 120$ and 240 Å as a function of energy E and momentum parallel to the wrinkle $k_{//}$. Furthermore, each panel shows transmission $T(E)$ plotted at a specific $k_{//}{=}\pm 2\pi/(3a_0)$ ($a_0 = 2.46$ Å is the lattice constant of graphene), which corresponds to the momentum of projections of the Dirac cone band degeneracies.

There are two striking observations in the presented transmission plots. Firstly, both in DFT and TB results, we observe a pronounced electron-hole asymmetry in the charge-carrier transmission. The electron-hole asymmetry has an origin in the interlayer stacking of zigzag wrinkles. The collapsed region assumes Bernal stacking configurations AB_1' or AB_2' (Gilbert *et al.*, 2019), as illustrated in Fig. 8.1(c), in which one of the graphene sublattices couples to itself upon folding since the two layers are mirror-symmetric with respect to each other. Such a coupling breaks the sublattice symmetry and hence the electron-hole symmetry (ichi Sasaki *et al.*, 2006, Semenoff, 2012).

Secondly, ballistic transmission $T(E, k_{//})$ shows pronounced oscillations over broad energy ranges. Apart from making transmission highly energy-dependent, such oscillations also affect average conductance at a finite bias. These oscillations are clearly visible in the side panels of Figs. 8.2(a-d) that show transmission at a fixed momentum $k_{//} = 2\pi/(3a_0)$ that corresponds to the projections of the Dirac points. Further analysis shows that the energy separation Δ_E between the peaks has an approximately linear dependence on Δ_W (Fig. 8.2(e)). Such a dependence is the signature of the interference between the interlayer and intralayer transport

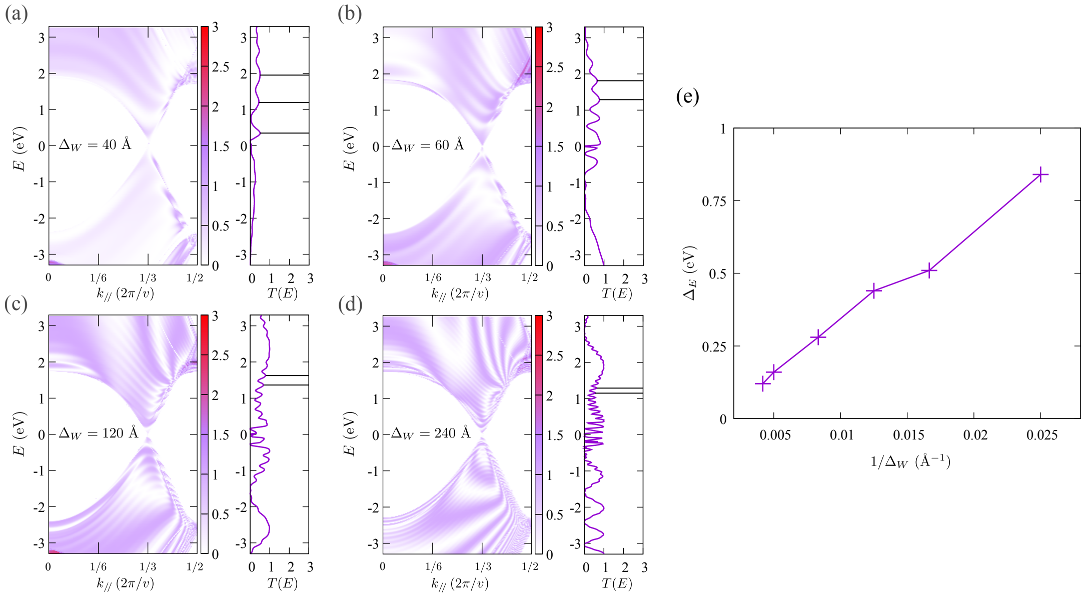

Figure 8.2 – Ballistic transmissions $T(E, k_{//})$ of zigzag wrinkle models defined by (a) $\Delta_W = 40$ Å, (b) $\Delta_W = 60$ Å, (c) $\Delta_W = 120$ Å and (d) $\Delta_W = 240$ Å calculated from first principles. The side panels show the transmission probability at $k_{//} = 2\pi/(3a_0)$ which corresponds to the projections of the Dirac points. The energy spacing Δ_E between the oscillation peaks are highlighted by lines. (e) Dependence of Δ_E on $1/\Delta_W$.

channels, as found by some of us previously in the case of electromechanical response of bilayer graphene (Benameur *et al.*, 2015). This transport phenomenon is further addressed in Section 8.4.

The second family of investigated commensurate configurations is defined by $\mathbf{v} = (1,1)$, that is wrinkles are oriented along the armchair direction. Atomic relaxation effects are more complex in such wrinkles. Unlike in the zigzag case, realizing the lowest-energy Bernal stacking is possible only at a cost of introducing shear deformation as shown in Fig. 8.3(a). Consequently, the Bernal stacking is not achieved at small values of Δ_W, and the collapsed region assumes the saddle-point (SP) stacking configuration (San-Jose *et al.*, 2014) that does not break sublattice symmetry. Figure 8.3(b) presents the evolution of shear deformation Δ_y upon the change of Δ_W with $\Delta_y = a_0/(2\sqrt{3})$ representing the pure Bernal stacking configuration. Figures 8.3(c-d) present the transmission maps for the armchair wrinkles with $\Delta_W = 40$ Å and $\Delta_W = 120$ Å. In the case of $\mathbf{v} = (1,1)$, the Dirac points are projected onto $k_{//} = 0$. Similar to the case of zigzag wrinkles, oscillations with the $\Delta_E \propto 1/\Delta_W$ period are observed in the transmission maps. The oscillation pattern is more regular than in the case of $\Delta_W = 40$ Å armchair wrinkle, which assumes the SP stacking and hence preserves electron-hole symmetry. In contrast, the $\Delta_W = 120$ Å wrinkle is significantly closer to the Bernal stacking (see Fig. 8.3(b)) and the electron-hole symmetry appears to be well visible in this case.

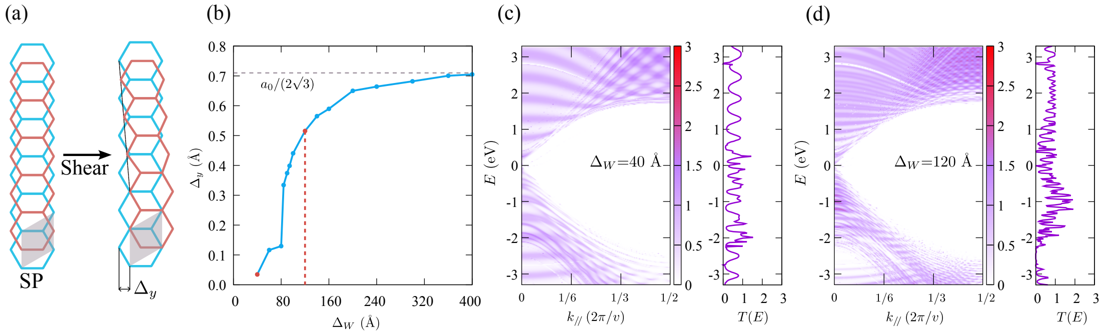

Figure 8.3 – (a) Schematic illustration of the shear deformation in armchair wrinkles. The shear is characterized by displacement Δ_y. (b) Evolution of shear deformation Δ_y versus compressive displacement Δ_W. At small values of Δ_W, shear deformation Δ_y is small, which corresponds to to the SP stacking configuration ($\Delta_y = a_0/(2\sqrt{3})$ corresponds to pure Bernal stacking. (c-d) Ballistic transmissions $T(E, k_{//})$ across armchair wrinkle models defined by (c) $\Delta_W = 40$ Å and (d) $\Delta_W = 120$ Å. The $T(E)$ cross sections are taken at $k_{//}$=0 that corresponding to the projected Dirac points.

8.4 Conductance oscillations in the atomic chain model

In order to further address the physical mechanism underlying the conductance oscillations observed in both the zigzag and armchair wrinkles, we introduce a simple one-dimensional model treated using the tight-binding approximation. The presence of interlayer conductance channels is defined by Δ_W, and also l that represents the absence of interlayer hopping in the loop-like region as shown in Fig. 8.4(a). At the same time, we observe that $k_{//}$ does not have any significant effect on the oscillation period, hence we introduce a one-dimensional chain described using the nearest-neighbor tight-binding model with an extra hopping t' that models interlayer coupling in graphene wrinkles. Schematic diagram of this model with hopping t' represented by a rainbow-like graph is shown in Fig. 8.4(b). The ratio of the newly introduced hopping t' to the nearest-neighbor hopping t is chosen to resemble that of graphene wrinkles $t'/t = 0.48$ eV/-2.7 eV (Gargiulo and Yazyev, 2018, Zhu *et al.*, 2012). Figure 8.4(c) shows transmission T as a function of energy E at a fixed Δ_W=12 in units of intersite distance, while parameter l is varied. We observe that oscillation peaks have the same positions, which indicates that l is of little effect on the oscillation period. Combined with the results of DFT calculations we conclude that the oscillations are defined by the largest path difference Δ_W. We further analyze the transmission oscillations in the atomic chain model using the non-equilibrium Green's functions (NEGF) approach (see Sec. 2.6), in which hoppings t' are treated as a perturbative correction to the transmission.

First, we define an infinite atomic chain with the Hamiltonian

$$H = t\sum_i c_i^\dagger c_{i+1} + h.c., \tag{8.1}$$

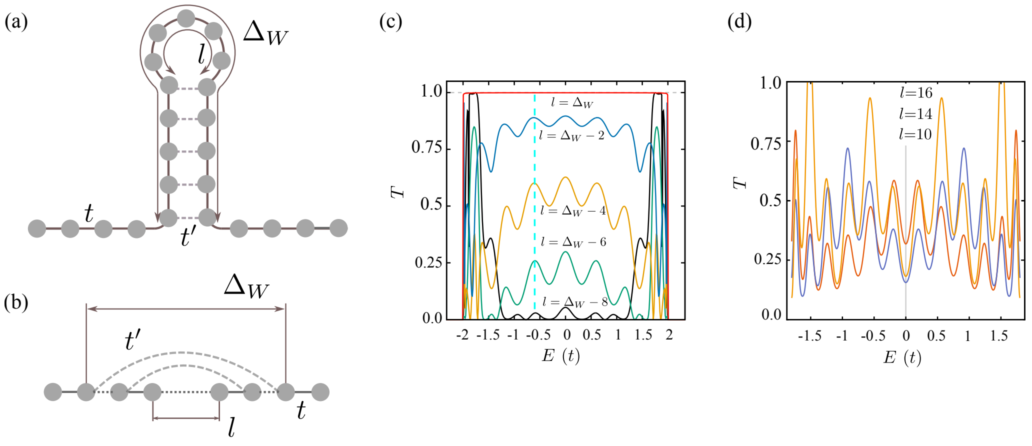

Figure 8.4 – Transmission oscillations in atomic chain model. (a) Cross-section drawing of the trivialized graphene wrinkle and (b) its unfolded representation equivalent to atomic chain with additional hoppings. (c) Transmission T as a function energy E in units of t calculated using the TB model Hamiltonian. In this plot $\Delta_W = 12$ in units of intersite distance is fixed, while different curves correspond to difference values of l. (d) First-order correction to the Green's function $\delta(E) = G_0 \Delta h G_0 / G_0$ plotted for different l and constant $\Delta_W = 20$ reveals that the period of oscillations is governed by Δ_W.

where c_i ($c_i^\dagger$) is the annihilation (creation) operator on the ith site. This Hamiltonian commutes with the translation operator, thus the energy eigenstates are also momentum eigenstates.

In the NEGF formalism (Gargiulo and Yazyev, 2014, Büttiker, 1986), the transmission is calculated as

$$T(E) = \mathrm{Tr}[\Gamma_1 G \Gamma_2 G], \tag{8.2}$$

where G is the Green's function $G(E)=[E - H - \Sigma]^{-1}$. The coupling matrices Γ_i are given by $\Gamma_i = i(\Sigma_i - \Sigma_i^\dagger)$, with Σ_i being the self-energies of the two semi-infinite leads.

Green's function G_0 describes the chain in absence of t', while adding coupling t' that models interlayer coupling in wrinkles adds an additional term Δh

$$\Delta h = t' \sum_{i=l/2}^{\Delta_W/2} c_i^\dagger c_{-i} + h.c. \tag{8.3}$$

The Green's function is then

$$\begin{aligned} G(E) &= \frac{1}{G_0^{-1} - \Delta h} \\ &= G_0 + G_0 \Delta h G_0 + G_0 (\Delta h G_0)^2 + \dots . \end{aligned} \tag{8.4}$$

Keeping only the first order of correction $G_0 \Delta h G_0$, the transmission becomes

$$\begin{aligned} T = &\mathrm{Tr}[\Gamma_1 G_0 \Gamma_2 G_0 \\ &+ \Gamma_1 G_0 \Gamma_2 (G_0 + G_0 \Delta h G_0) \\ &+ \Gamma_1 (G_0 + G_0 \Delta h G_0) \Gamma_2 G_0 \\ &+ \Gamma_1 (G_0 + G_0 \Delta h G_0) \Gamma_2 (G_0 + G_0 \Delta h G_0)]. \end{aligned} \tag{8.5}$$

The Green's function can be written as an expansion involving eigenstates $|\psi_n\rangle$ of the chain with no hoppings t'

$$G_0(E) = \sum_n \frac{1}{E + \varepsilon i - E_n} |\psi_n\rangle\langle\psi_n|, \tag{8.6}$$

and the correction term $G_0 \Delta h G_0$ becomes

$$G_0 \Delta h G_0 = \sum_m \sum_n \frac{|\psi_m\rangle\langle\psi_m|\Delta h|\psi_n\rangle\langle\psi_n|}{(E + \varepsilon i - E_m)(E + \varepsilon i - E_n)}. \tag{8.7}$$

As the simplest case, we analyze the $E_n = E_m$ correction $G_0 \Delta h G_0 = \langle\psi_n|\Delta h|\psi_m\rangle G_0$ that gives an E_i-dependent prefactor to the Green's function. We write the factor as a function $\delta(E)$ as

$$\delta(E) G_0 = G_0 \Delta h G_0. \tag{8.8}$$

The leading order of transmission correction is $\Gamma_1(G_0 + G_0 \Delta h G_0)\Gamma_2(G_0 + G_0 \Delta h G_0)]$, hence the correction to transmission contains $\delta^2 + 4\delta + 1$.

We then evaluate the correction $\delta(E)$, keeping in mind that the eigenstates of the pristine chain

$$\hat{H}|\psi(k)\rangle = 2t\cos(k)|\psi(k)\rangle, \tag{8.9}$$

are also momentum eigenstates. The correction factor δ represents the phase difference between wavefunctions:

$$\delta(E) = \sum_i \langle\psi_n(r_i)|\Delta_h|\psi_n(r_{-i})\rangle\big|_{E_n = E} \tag{8.10}$$

connected by the additional hoppings t'. It can then be approximated by a sum of sinusoidal functions

$$\delta(k) = \frac{t'}{t} \sum_{i=l/2}^{\Delta_W/2} \cos(2ik). \tag{8.11}$$

The results of the summation shown in Fig. 8.4(d) suggests that the highest-frequency component in Eq. (8.11), which corresponds to the interference path Δ_W, defines the oscillation peaks. Our first-principles results are consistent with the conclusions of this simple model.

8.5 Transport across incommensurate wrinkles

We will now discuss graphene wrinkles formed along general crystallographic directions $\mathbf{v} = (a, b)$ other than high-symmetry zigzag and armchair orientations. In these cases, the collapsed region locally forms twisted bilayer graphene with matching vectors (a, b) and (b, a). The resulting twist angle is

$$\theta = \arccos\left(\frac{a^2 + 4ab + b^2}{2(a^2 + ab + b^2)}\right), \tag{8.12}$$

while the translational vector along the wrinkle has a length of $d = \sqrt{a^2 + b^2 + ab}$.

We discuss the effect of wrinkle direction (a, b) on the transmission $T(E, k_{//})$. Translational vector (a, b) defines a one-dimensional mini Brillouin zone (mBZ) obtained by projecting the 2D Brillouin zone of graphene onto the $k_{//}$ direction in momentum space. The Dirac cones of graphene are projected onto either $k_{//} = 0$ (class Ia) or $k_{//} = 2\pi/(3|\mathbf{v}|)$ (class Ib) of the mBZ according to the classification introduced in Ref. (Yazyev and Louie, 2010). Class Ia is defined by $|a - b| \mod 3 = 0$, class Ib otherwise. The projections of the Dirac cones define the regions in the $T(E, k_{//})$ maps where transmission is allowed and limited by n conductance channels in case of n-fold degeneracy of bands at given E and $k_{//}$ in the ballistic regime.

The periodic structure of wrinkles results in consequences deeper than just the conservation of momentum $k_{//}$ upon ballistic transmission. We stress that semi-infinite graphene sheets on both sides of wrinkles of constant width have the same crystallographic orientation. The momentum conservation implies suppressed backscattering at the Dirac point, which can be observed by evaluating contribution to the transmission from the first-order correction $G_0 \Delta h G_0$. Starting with the pristine graphene and a simple interlayer containing only hopping between aligned atoms

$$\Delta h_{ij} = \begin{cases} t', & r_i^{\perp} = r_j^{\perp} \\ 0, & r_i^{\perp} \neq r_j^{\perp}, \end{cases} \tag{8.13}$$

the effective ΔG writes

$$G_0 \Delta h G_0(z) = \sum_m \sum_n \frac{\langle \psi_m | \Delta h | \psi_n \rangle}{(z - E_m)(z - E_n)} |\psi_m\rangle \langle \psi_n|, \tag{8.14}$$

which becomes most significant at $E_m = E_n = z$. Recalling the fact that $|\psi_m\rangle$ and $|\psi_n\rangle$ are eigenstates of pristine graphene, $\langle \psi_m | \Delta h | \psi_n \rangle$ gives an $\exp\bigl(2\pi i (\mathbf{k}_m - \mathbf{k}_n) \cdot \mathbf{r}_{ij}\bigr)$ term. Integrating over $\mathbf{r}_{ij}$, ΔG vanishes if $\mathbf{k}_m \neq \mathbf{k}_n$, while the wrinkle enforces a transformation $\mathbf{k}_m = \mathscr{M}_x \mathbf{k}_n$ due to its mirror-symmetric stacking configuration of the two layers as shown in Figs. 8.5(a,b). Here, $\mathscr{M}_x$ denotes the mirror-reflection with respect to transport direction x: $\mathscr{M}_x(k_x, k_y) = (-k_x, k_y)$. From the above rules of momentum conservation, we conclude that the transmission is only affected in the overlapping region of the Dirac cones. In the non-overlapping region, the correction $G_0 \Delta h G_0$ is vanishing, and the transmission retains the value of ideal, defect-free

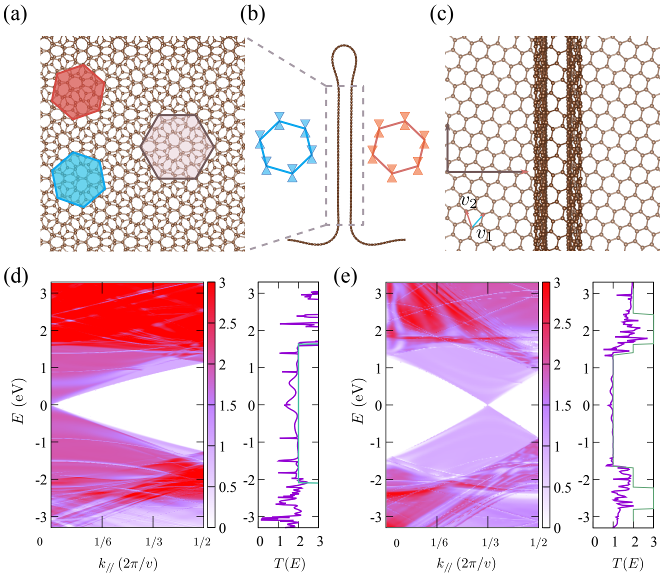

Figure 8.5 – Atomic structure of incommensurate wrinkle defined by the (1,2) direction: (a) local structure of the collapsed region equivalent to twisted bilayer graphene (unit cell is shown with the shaded region), (b) side-view with the sketch of the Brillouin zones and the Dirac cones of adjacent layers, and (c) top-view of the wrinkle illustrating the conservation of crystallographic orientation of graphene leads. Transmission maps $T(E,k_{//})$ for wrinkle models defined by (d) **v**=(1,4) and $\Delta_W = 80$ Å(class Ia), (e) **v**=(1,2) and $\Delta_W = 80$ Å(class Ib).

graphene. These results are verified by the explicit DFT transport calculations as shown in Fig. 8.5(d-e) for class Ia and class Ib wrinkles, respectively. The transmission maps $T(E,k_{//})$ have overall shape of the Dirac cone projections. Transmission values near the charge neutrality are $T \approx 2$ and $T \approx 1$ for class Ia and Ib configurations, respectively, indicating that interlayer tunnelling plays a minor role. At higher energies where the Dirac cones overlap, e.g. near $E \approx 2$ eV in Fig. 8.5(e), backscattering becomes significant leading to a series of transmission dips. We also point out that class Ia presents larger backscattering from the interlayer coupling since the projected Dirac cones overlap with each other.

8.6 Transport across graphene folds

We will now discuss folds as the ultimate regime of out-of-plane disorder in graphene. Folds realize triple-layer graphene configurations in their collapsed regions (Fig. 8.6(a-c)). Importantly, adjacent layers (pairs 1–2 and 2–3) in incommensurate folds are twisted with respect to each other, while the outside layers 1 and 3 are aligned. This configuration is equivalent to mirror-symmetric twisted trilayer graphene. While we still expect the effect of interlayer coupling to be weakened by the incommensuration, our DFT calculations predict a larger degree of backscattering in folds than in wrinkles (compare Figs. 8.5(e) and 8.6(d) for the the (1,2) direction). For the folded region of width $l_f = 40$ Å, the average transmission in

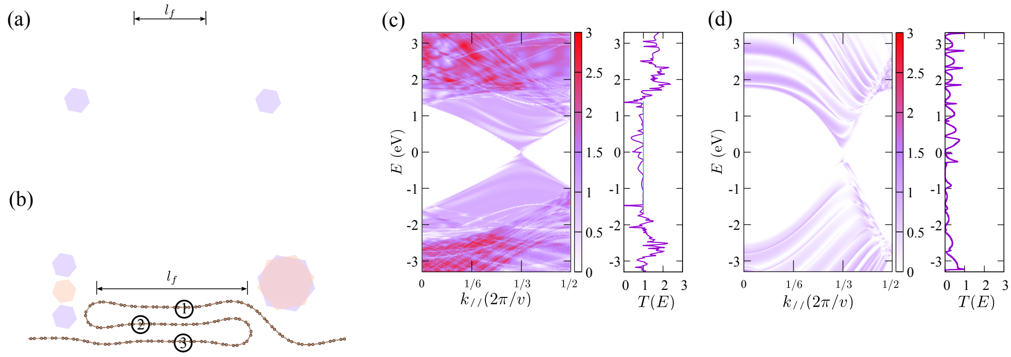

Figure 8.6 – (a) Atomic structure of an incommensurate fold defined by $\mathbf{v} = (1,2)$ as an example. (b) Side-view of the fold with layers numbered and Brillouin zone orientations indicated. Transmission maps $T(E, k_{//})$ for (c) the incommensurate fold shown in the above panels and (d) zigzag fold characterized by $\Delta_W = 80$ Å.

the energy interval (−0.15 eV, 0.15 eV) is 0.727, while in the wrinkle of equivalent $\Delta_W = 80$ Å it is 0.908. The observed transport behaviour raises the question of whether the enhanced backscattering in incommensurate folds as compared to wrinkles originates from the direct coupling of the outmost layers 1 and 3. The corresponding matrix elements of the Hamiltonian in localized-basis-set first-principles calculations (Soler *et al.*, 2002, Papior, 2022), are found to be negligible. The estimated Slater-Koster coupling also has a negligible magnitude of 10^{-4} eV. Therefore, we attribute the enhanced scattering to the fact that the number of interlayer tunneling channels is doubled in the folds. As expected, for a commensurate zigzag fold (Fig. 8.6(d)) we observe strong backscattering with transmission magnitudes lower than in the equivalent zigzag wrinkles (Fig. 8.2).

8.7 Tight-binding results for the transmission

In addition to the first-principles resulte, we present the results of tight-binding (TB) transmission calculations. Our TB calculations include nearest-neighbour (NN) intralayer hoppings (the π-type bonds between p_z orbitals) and the interlayer hoppings in the collapsed region of the wrinkle. The presence of only NN intralayer hoppings imply electron-hole symmetry of the pristine graphene layer, which reflects in the envelope of the transmission map $T(E, k_{//})$. Fig. 8.7 presents the transmission $T(E, k_{//})$ obtained from TB calculations for commensurate zigzag wrinkles characterized by the same lateral displacements $\Delta_W = 40$ Å, 60 Å, 120 Å and 240 Å as the ones used in our DFT calculations. The Slater-Koster TB model is able to reproduce the oscillating behaviour of the transmission observed in DFT results. Fig. 8.7(b) also provides a comparison of the TB and DFT transmissions at $k_{//} = 2\pi/(3a_0)$. One can observe good overall agreement between the two theories throughout the discussed energy range, apart from the small shift in energy of the two profiles. Our TB calculations also account for correct electron-hole asymmetry induced by the interlayer tunnelling.

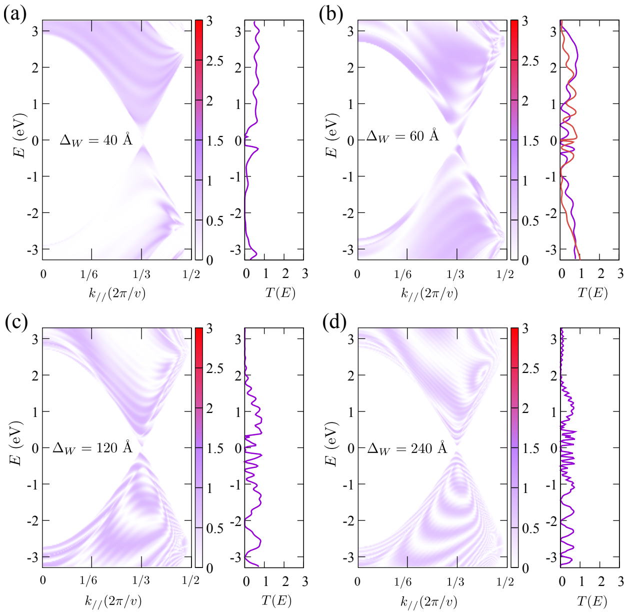

Figure 8.7 – Tight-binding results for the electronic transmission across zigzag graphene wrinkles. Ballistic transmissions $T(E, k_{//})$ across zigzag wrinkle models characterized by (a) Δ_W = 40 Å, (b) Δ_W = 60 Å, (c) Δ_W = 120 Å, (d) Δ_W = 240 Å. The side panels show the transmission probability at $k_{//} = 2\pi/(3a_0)$.

Fig. 8.8 presents the results of TB calculations for the incommensurate wrinkle models characterized by $\mathbf{v} = (1,4)$ and $\mathbf{v} = (1,2)$ wrinkles. As in DFT results we observe nearly perfect constant transmissions at low charge-carrier energies. The agreement between the two theories suggests that the Slater-Koster TB model provides a faithful description of the electronic transport in graphene with out-of-plane disorder, fully accounting for the effects of curvature and interlayer tunnelling.

8.8 Discussion

We investigated the effect of our-of-plane disorder on the electronic transmission in graphene. Different forms of the our-of-plane disorder exist in graphene, depending on the compressive displacement and the orientation of the deformation. Our work studied ballistic transmission through the wrinkles and folds using first-principle calculations, taking into account their width and interlayer commensuration.

The interlayer coupling was found to cause substantial oscillations in the electronic transmission across commensurate wrinkles. Such oscillations were found to originate from the quantum interference involving the interlayer tunneling channels. Based on DFT calculations, we propose a simple one-dimensional model that fully captures the observed oscillations. On the other hand, in incommensurate, "twisted" wrinkles the interlayer coupling is effectively

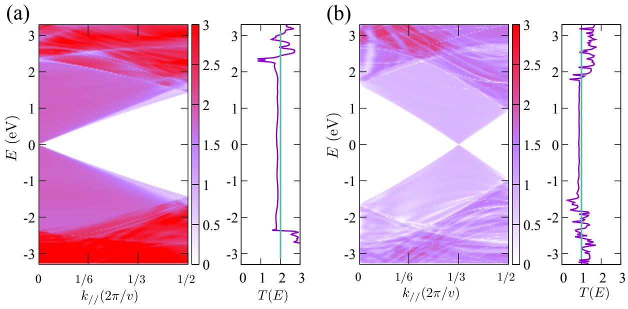

Figure 8.8 – Tight-binding results for the electronic transmission across incommensurate wrinkles. Ballistic transmissions $T(E, k_{//})$ across wrinkle models characterized by $\Delta_W = 80$ Å and (a) $\mathbf{v} = (1,4)$, (b) $\mathbf{v} = (1,2)$. The side panels show the transmission probability at $k_{//} = 2\pi/(3a_0)$.

weaker, and the transmission near the Fermi level preserves that of pristine, flat graphene. We have also found enhanced backscattering in folds that was attributed to the doubled contact region in this type of the out-of-plane disorder.

Our results offer an approach toward understanding the transport in mesoscopic graphene samples containing out-of-plane disorder of different type and arbitrary orientation. The theory of transmission across graphene wrinkles and folds is thus useful for designing graphene-based devices as well as fold-engineering of graphene. As a generalization, the principles presented in our work are expected to apply also to other types of 2D materials. Formation of locally twisted bilayers in the wrinkles and folds provides an interesting outlook for further works, e.g. the “twisted” wrinkles in the smaller-angle regime.

9 Concluding remarks

Low-dimensional systems are known to host different physical phenomena from bulk materials. As an example, the quantum Hall effect relies on the two-dimensional nature of the electron gas, where the topological Chern number is defined. Since the discovery of graphene (Novoselov *et al.*, 2004, 2005), the last few decades have seen an increasing number of works in the field of two-dimensional materials. The more recent works on twisted multilayers have further enriched the topic by providing another tunable degree of freedom (Cao *et al.*, 2018a,b).

This thesis investigates various phenomena in carbon-based low-dimensional nanostructures, with an emphasis on the role of band topology. It contains the theoretical work of physical observables in topological insulators and the computational research of topological effects in twisted multilayer graphene.

9.1 Overview

Two levels of research are involved on the topic of two-dimensional materials and topology: theoretical works based on abstract models and a study of moiré materials in atomistic models.

In Part I, we provide the magnetic response and edge states of Euler-class topological insulators. This part of the work aims to provide signatures for Euler class topology. Compared to the well-known Chern insulators, we inspect the magnetic-field response and edge states of Euler insulators. The toy-model results relate to the magic-angle twisted bilayer graphene systems where topological Euler bands with $E = \pm 1$ are reported. We also expect that the general deductions will apply to broader ranges of materials of Euler numbers greater than one. While such higher-Euler materials have not been reported yet, we would suggest a family of materials to consider. Similar to the mechanism in magic-angle TBG, where the Dirac points with ± 1 monopole charges evolve into $E = \pm 1$ Euler bands, the twisted bilayer materials with a higher monopole charge in each layer may possess $E > 1$.

Part II is mainly focused on twisted multilayer graphene. Since the discovery of correlated states and unconventional superconductivity, there have been extensive discussions on the topology of moiré flat bands and their effects on the interactions of electrons. We investigate the effect of underlying quantum geometry in twisted multilayer graphene. Typically, we calculate the topological numbers of flat bands and the corresponding Wannier diagrams. Such diagrams provide the maps of quantum Hall conductance, which are widely used in characterizing 2D materials as they resemble the results of transport measurements. The works in Part II thus discuss the effect of topological phases and their signatures in the magnetic response.

Lastly, Part III contains the standalone work of electronic transmission in graphene with the out-of-plane disorder. This category of disorder is intrinsic in low-dimensional materials, and its impact on transmission is essential for engineering 2D materials. We find that the orientation of out-of-plane disorder plays a prominent role in backscattering: wrinkles in a commensurate direction exhibit larger scattering than the incommensurate case. Such results connect to twistronics as well, since the incommensurate wrinkles or folds locally form twisted bilayer or trilayer graphene. We would expect the crossover of zero modes, snake states, and moiré bands to provide intriguing phenomena near the magic angle.

9.2 Outlook

In addition to the well-known quantum Hall effects, recent works have revealed that the topology of bands also affects electronic interactions. Examples of such interplay appear in the fractional Chern insulators (Neupert *et al.*, 2011) and the topological contribution to superfluid weights (Peotta and Törmä, 2015, Tian *et al.*, 2023). A natural continuation of the research will be to investigate the effect of band topology in the presence of interactions. As such effects are extensively discussed for the family of moiré materials, we have developed a set of tools aimed at post-TB many-body calculations. Such methods will hopefully be able to carry out the study of interactions, fully involving the quantum geometry of the eigenstates. Considering the interacting phases, two scenarios are of special interest: the electronic transport in the presence of phonons, and the transmission in interacting mesoscopic quantum dots.

Another dimension to explore lies in structural complexity. For example, recent progress on the hyperbolic band theory has enriched the content of the Bloch theorem by embedding a four-dimensional (4D) Bolza lattice on the hyperbolic tiling. In addition to the first Chern numbers, such 4D lattice also hosts the second Chern number which is absent in 2D reciprocal spaces [1]. A further category of structural complexity that arises naturally in various materials is the amorphous phase. While a constant curvature is produced by the tiling in a hyperbolic lattice, amorphous materials host non-homogeneous spatial curvature. The effect of local curvature fluctuation in amorphous materials may induce topological transitions. It will be of interest to explore the effect, for an improved interpretation of topological phase transition and the behavior of topological materials in the presence of defects.

---

[1] Generally, the n-th Chern number requires $2n$-dimensional base manifolds.

Bibliography

K. von Klitzing, G. Dorda, and M. Pepper, Physical Review Letters **45**, 494 (1980).

K. von Klitzing, Reviews of Modern Physics **58**, 519 (1986).

Y. Hatsugai, Physical Review Letters **71**, 3697 (1993).

D. J. Thouless, M. Kohmoto, M. P. Nightingale, and M. den Nijs, Physical Review Letters **49**, 405 (1982).

C. L. Kane and E. J. Mele, Physical review letters **95**, 226801 (2005a).

C. L. Kane and E. J. Mele, Physical Review Letters **95**, 146802 (2005b).

B. A. Bernevig, T. L. Hughes, and S.-C. Zhang, Science **314**, 1757 (2006).

B. A. Bernevig and S.-C. Zhang, Physical review letters **96**, 106802 (2006).

A. P. Schnyder, S. Ryu, A. Furusaki, and A. W. W. Ludwig, Physical Review B **78**, 195125 (2008).

A. Kitaev, AIP Conference Proceedings **1134**, 22 (2009).

C.-K. Chiu, J. C. Y. Teo, A. P. Schnyder, and S. Ryu, Reviews of Modern Physics **88**, 035005 (2016).

L. Fu and C. L. Kane, Physical Review B **76**, 045302 (2007).

A. M. Turner, Y. Zhang, R. S. K. Mong, and A. Vishwanath, Physical Review B **85**, 165120 (2012).

C.-K. Chiu and A. P. Schnyder, Physical Review B **90**, 205136 (2014).

C.-K. Chiu, H. Yao, and S. Ryu, Physical Review B **88**, 075142 (2013).

L. Fu, Physical Review Letters **106**, 106802 (2011).

C. Fang, M. J. Gilbert, and B. A. Bernevig, Physical Review B **86**, 115112 (2012).

R.-J. Slager, A. Mesaros, V. Juričić, and J. Zaanen, Nature Physics **9**, 98 (2013).

K. Shiozaki and M. Sato, Physical Review B **90**, 165114 (2014).

A. Alexandradinata, Z. Wang, and B. A. Bernevig, Physical Review X **6**, 021008 (2016).

E. Cornfeld and A. Chapman, Physical Review B **99**, 075105 (2019).

J. Kruthoff, J. de Boer, J. van Wezel, C. L. Kane, and R.-J. Slager, Physical Review X **7**, 041069 (2017).

H. C. Po, A. Vishwanath, and H. Watanabe, Nature Communications **8**, 50 (2017).

E. Khalaf, H. C. Po, A. Vishwanath, and H. Watanabe, Physical Review X **8**, 031070 (2018).

B. Bradlyn, Z. Wang, J. Cano, and B. A. Bernevig, Physical Review B **99**, 045140 (2019).

B. Bradlyn, L. Elcoro, J. Cano, M. G. Vergniory, Z. Wang, C. Felser, M. I. Aroyo, and B. A. Bernevig, Nature **547**, 298 (2017).

Z. Song, S.-J. Huang, Y. Qi, C. Fang, and M. Hermele, Science Advances **5**, eaax2007 (2019a).

Z.-D. Song, L. Elcoro, Y.-F. Xu, N. Regnault, and B. A. Bernevig, Physical Review X **10**, 031001 (2020a).

H. C. Po, H. Watanabe, and A. Vishwanath, Physical Review Letters **121**, 126402 (2018a).

Z.-D. Song, L. Elcoro, and B. A. Bernevig, Science **367**, 794 (2020b).

A. Bouhon, A. M. Black-Schaffer, and R.-J. Slager, Physical Review B **100**, 195135 (2019).

N. Marzari and D. Vanderbilt, Physical Review B **56**, 12847 (1997).

Y. Xu, L. Elcoro, G. Li, Z.-D. Song, N. Regnault, Q. Yang, Y. Sun, S. Parkin, C. Felser, and B. A. Bernevig 10.48550/ARXIV.2111.02433 (2021).

F. Xie, Z. Song, B. Lian, and B. A. Bernevig, Physical Review Letters **124**, 167002 (2020).

B. A. Bernevig, Z.-D. Song, N. Regnault, and B. Lian, Physical Review B **103**, 205413 (2021).

K.-E. Huhtinen, J. Herzog-Arbeitman, A. Chew, B. A. Bernevig, and P. Törmä, Physical Review B **106**, 014518 (2022).

K. von Klitzing, Physica B: Physics of Condensed Matter & C: Atomic, Molecular and Plasma Physics, Optics **126 B-C**, 242 (1984).

R. B. Laughlin, Physical Review B **23**, 5632 (1981).

H. Zhang, C.-X. Liu, X.-L. Qi, X. Dai, Z. Fang, and S.-C. Zhang, Nature physics **5**, 438 (2009).

W. A. Benalcazar, T. Li, and T. L. Hughes, Physical Review B **99**, 50 (2019).

W. A. Benalcazar, B. A. Bernevig, and T. L. Hughes, Science **357**, 61 (2017a).

G. Autès, Q. Wu, N. Mounet, and O. Yazyev, Mater. Cloud Arch **10** (2019).

X.-L. Qi, T. L. Hughes, and S.-C. Zhang, Physical Review B **78**, 195424 (2008).

S. Coh and D. Vanderbilt, Physical Review Letters **102**, 107603 (2009).

R. Resta, Journal of Physics: Condensed Matter **22**, 123201 (2010).

M.-C. Chang and Q. Niu, J. Phys.: Condens. Matter **20**, 193202 (2008).

M.-C. Chang and Q. Niu, Physical Review B **53**, 7010 (1996).

Y. Gao, S. A. Yang, and Q. Niu, Physical Review B **91**, 214405 (2015).

T. Thonhauser, D. Ceresoli, D. Vanderbilt, and R. Resta, Physical review letters **95**, 137205 (2005).

P. Streda, Journal of Physics C: Solid State Physics **15**, L1299 (1982a).

P. Streda, Journal of Physics C: Solid State Physics **15**, L717 (1982b).

I. Dana, Y. Avron, and J. Zak, Journal of Physics C: Solid State Physics **18**, L679 (1985a).

J. Shi, G. Vignale, D. Xiao, and Q. Niu, Physical Review Letters **99**, 197202 (2007).

T. Thonhauser, International Journal of Modern Physics B: Condensed Matter Physics, Statistical Physics, Applied Physics **25**, 1429 (2011).

Q. Wu, J. Liu, Y. Guan, and O. V. Yazyev, Physical Review Letters **126**, 056401 (2021).

G. Sundaram and Q. Niu, Physical Review B **59**, 14915 (1999).

N. Marzari, A. A. Mostofi, J. R. Yates, I. Souza, and D. Vanderbilt, Reviews of Modern Physics **84**, 1419 (2012).

S. Zhang, B. Xie, Q. Wu, J. Liu, and O. V. Yazyev, Chiral Decomposition of Twisted Graphene Multilayers with Arbitrary Stacking (2020a).

W. A. Benalcazar, B. A. Bernevig, and T. L. Hughes, Physical Review B **96**, 245115 (2017b).

Z. Song, C. Fang, and Y. Qi, Nature Communications **11**, 4197 (2020c).

G. Li, Y. Xu, Z. Song, Q. Yang, Y. Zhang, J. Liu, U. Gupta, V. Süβ, Y. Sun, P. Sessi, *et al.*, Advanced Materials , 2201328 (2022).

M. Barkeshli and X.-L. Qi, Physical Review X **2**, 031013 (2012).

S. Peotta and P. Törmä, Nature Communications **6**, 8944 (2015).

Y. Cao, V. Fatemi, S. Fang, K. Watanabe, T. Taniguchi, E. Kaxiras, and P. Jarillo-Herrero, Nature **556**, 43 (2018a).

F. Wilczek and A. Zee, Physical Review Letters **51**, 2250 (1983).

S. L. Sondhi, A. Karlhede, S. Kivelson, and E. Rezayi, Physical Review B **47**, 16419 (1993).

K. S. Novoselov, A. K. Geim, S. V. Morozov, D. Jiang, Y. Zhang, S. V. Dubonos, I. V. Grigorieva, and A. A. Firsov, Science **306**, 666 (2004).

K. S. Novoselov, D. Jiang, F. Schedin, T. J. Booth, V. V. Khotkevich, S. V. Morozov, and A. K. Geim, Proceedings of the National Academy of Sciences of the United States of America **102**, 10451 (2005).

X. Qian, J. Liu, L. Fu, and J. Li, Science **346**, 1344 (2014).

H. Jang, Y. J. Park, X. Chen, T. Das, M. S. Kim, and J. H. Ahn, Advanced Materials **28**, 4184 (2016).

L. Ju, Z. Shi, N. Nair, Y. Lv, C. Jin, J. Velasco, C. Ojeda-Aristizabal, H. A. Bechtel, M. C. Martin, A. Zettl, J. Analytis, and F. Wang, Nature **520**, 650 (2015).

Y. Han, K. Nguyen, M. Cao, P. Cueva, S. Xie, M. W. Tate, P. Purohit, S. M. Gruner, J. Park, and D. A. Muller, Nano Letters **18**, 3746 (2018).

K. K. Gomes, W. Mar, W. Ko, F. Guinea, and H. C. Manoharan, Nature **483**, 306 (2012).

K. Wang, B. Huang, M. Tian, F. Ceballos, M. W. Lin, M. Mahjouri-Samani, A. Boulesbaa, A. A. Puretzky, C. M. Rouleau, M. Yoon, H. Zhao, K. Xiao, G. Duscher, and D. B. Geohegan, ACS Nano **10**, 6612 (2016).

P. Moon and M. Koshino, Physical Review B - Condensed Matter and Materials Physics **90**, 1 (2014).

Y. Cao, V. Fatemi, A. Demir, S. Fang, S. L. Tomarken, J. Y. Luo, J. D. Sanchez-Yamagishi, K. Watanabe, T. Taniguchi, E. Kaxiras, *et al.*, Nature **556**, 80 (2018b).

H. C. Po, L. Zou, A. Vishwanath, and T. Senthil, Physical Review X **8**, 31089 (2018b).

O. V. Yazyev, Accounts of Chemical Research **46**, 2319 (2013).

L. Talirz, P. Ruffieux, and R. Fasel, Advanced Materials **28**, 6222 (2016).

Y. W. Son, S. M. Choi, Y. P. Hong, S. Woo, and S. H. Jhi, Physical Review B - Condensed Matter and Materials Physics **84**, 1 (2011).

E. Mariani, A. J. Pearce, and F. Von Oppen, Physical Review B - Condensed Matter and Materials Physics **86**, 1 (2012).

T. Cao, F. Zhao, and S. G. Louie, Physical Review Letters **119**, 1 (2017).

F. D. M. Haldane, Physical Review Letters **61**, 2015 (1988).

R. Bistritzer and A. H. MacDonald, Physical Review B - Condensed Matter and Materials Physics **84**, 1 (2011a).

M. Luo, , 1 (2019).

X. Liu, Z. Hao, E. Khalaf, J. Y. Lee, Y. Ronen, H. Yoo, D. Haei Najafabadi, K. Watanabe, T. Taniguchi, A. Vishwanath, *et al.*, Nature **583**, 221 (2020).

Z. Song, Z. Wang, W. Shi, G. Li, C. Fang, and B. A. Bernevig, Physical Review Letters **123**, 036401 (2019b).

X. Du, I. Skachko, F. Duerr, A. Luican, and E. Y. Andrei, Nature **462**, 192 (2009).

C. R. Dean, L. Wang, P. Maher, C. Forsythe, F. Ghahari, Y. Gao, J. Katoch, M. Ishigami, P. Moon, M. Koshino, and others, Nature **497**, 598 (2013).

H. C. Po, L. Zou, T. Senthil, and A. Vishwanath, Physical Review B **99**, 195455 (2019).

R. Bistritzer and A. H. MacDonald, Proceedings of the National Academy of Sciences of the United States of Americab **108**, 12233 (2011b).

B. Lian, F. Xie, and B. A. Bernevig, , 1 (2018).

Y. H. Zhang, H. C. Po, and T. Senthil, Physical Review B **100**, 1 (2019).

J. Liu, J. Liu, and X. Dai, Physical Review B **99**, 155415 (2019a).

G. Tarnopolsky, A. J. Kruchkov, and A. Vishwanath, Physical Review Letters **122**, 10.1103/PhysRevLett.122.106405 (2019).

K. Hejazi, C. Liu, and L. Balents, Physical Review B **100**, 1 (2019).

M. Schultz, U. Merkt, A. Sonntag, and U. Rössler, Physical Review B - Condensed Matter and Materials Physics **57**, 14772 (1998).

Z. F. Wang, F. Liu, and M. Y. Chou, Nano Letters **12**, 3833 (2012).

K. Kim, A. DaSilva, S. Huang, B. Fallahazad, S. Larentis, T. Taniguchi, K. Watanabe, B. J. LeRoy, A. H. MacDonald, and E. Tutuc, Proceedings of the National Academy of Sciences of the United States of America **114**, 3364 (2017).

C. Dutreix, H. González-Herrero, I. Brihuega, M. I. Katsnelson, C. Chapelier, and V. T. Renard, Nature **574**, 219 (2019).

J. C. Slater and G. F. Koster, Physical Review **94**, 1498 (1954).

F. Gargiulo and O. V. Yazyev, 2D Materials **5**, 015019 (2018).

J. Liu, Z. Ma, J. Gao, and X. Dai, Physical Review X **9**, 031021 (2019b).

J. M. Park, Y. Cao, L.-Q. Xia, S. Sun, K. Watanabe, T. Taniguchi, and P. Jarillo-Herrero, Nature Materials **21**, 877 (2022).

J.-M. Combes, P. Duclos, and R. Seiler, Rigorous atomic and molecular physics , 185 (1981).

J. Herzog-Arbeitman, A. Chew, and B. A. Bernevig, Physical Review B **106**, 085140 (2022).

D. R. Hofstadter, Physical Review B **14**, 2239 (1976).

G. H. Wannier, Physica Status Solidi B: Basic Solid State Physics **88**, 757 (1978).

W. Zhu, T. Low, V. Perebeinos, A. A. Bol, Y. Zhu, H. Yan, J. Tersoff, and P. Avouris, Nano Letters **12**, 3431 (2012).

J. A. Crosse, N. Nakatsuji, M. Koshino, and P. Moon, Physical Review B **102**, 035421 (2020).

A. A. Soluyanov and D. Vanderbilt, Physical Review B **83**, 035108 (2011).

M. Taherinejad, K. F. Garrity, and D. Vanderbilt, Physical Review B **89**, 115102 (2014).

F. Wu, T. Lovorn, and A. H. Macdonald, Physical Review Letters **118**, 1 (2017).

G. H. Wannier, Reviews of Modern Physics **34**, 645 (1962).

D. Gresch, G. Autes, O. V. Yazyev, M. Troyer, D. Vanderbilt, B. A. Bernevig, and A. A. Soluyanov, Physical Review B **95**, 075146 (2017).

A. Davydov, K. Choo, M. H. Fischer, and T. Neupert, Physical Review B **105**, 165153 (2022).

A. Abouelkomsan, Private communications .

Y. Meir and N. S. Wingreen, Physical Review Letters **68**, 2512 (1992).

M. Stone, ed., *Quantum Hall Effect* (World Scientific, Singapore, 1992).

D. Thouless, *Topological quantum numbers in nonrelativistic physics* (World Scientific, River Edge, 1998).

J. E. Avron, R. Seiler, and B. Simon, Physical Review Letters **51**, 51 (1983).

J. E. Avron, L. Sadun, J. Segert, and B. Simon, Communications in Mathematical Physics **124**, 595 (1989).

L. Fu, C. L. Kane, and E. J. Mele, Physical Review Letters **98**, 106803 (2007).

Y. L. Chen, J. G. Analytis, J.-H. Chu, Z. K. Liu, S.-K. Mo, X. L. Qi, H. J. Zhang, D. H. Lu, X. Dai, Z. Fang, S. C. Zhang, I. R. Fisher, Z. Hussain, and Z.-X. Shen, Science **325**, 178 (2009).

X.-L. Qi and S.-C. Zhang, Reviews of Modern Physics **83**, 1057 (2011).

H. Watanabe, H. C. Po, M. P. Zaletel, and A. Vishwanath, Physical Review Letters **117**, 096404 (2016).

A. Bouhon and A. M. Black-Schaffer, Physical Review B **95**, 241101(R) (2017).

K. Shiozaki, M. Sato, and K. Gomi, Physical Review B **95**, 235425 (2017).

J. Höller and A. Alexandradinata, Physical Review B **98**, 024310 (2018).

R. Thorngren and D. V. Else, Physical Review X **8**, 011040 (2018).

K. Shiozaki, C. Z. Xiong, and K. Gomi, Generalized homology and atiyah-hirzebruch spectral sequence in crystalline symmetry protected topological phenomena (2018).

J. Ahn, S. Park, and B.-J. Yang, Physical Review X **9**, 021013 (2019a).

V. Peri, Z.-D. Song, M. Serra-Garcia, P. Engeler, R. Queiroz, X. Huang, W. Deng, Z. Liu, B. A. Bernevig, and S. D. Huber, Science **367**, 797 (2020).

J. Ahn, D. Kim, Y. Kim, and B.-J. Yang, Physical Review Letters **121**, 106403 (2018).

A. Bouhon, Q. Wu, R.-J. Slager, H. Weng, O. V. Yazyev, and T. Bzdušek, Nature Physics **16**, 1137 (2020a).

A. Bouhon, T. Bzdušek, and R.-J. Slager, Physical Review B **102**, 115135 (2020b).

Y. X. Zhao and Y. Lu, Physical Review Letters **118**, 056401 (2017).

Q. Wu, A. A. Soluyanov, and T. Bzdušek, Science **365**, 1273 (2019).

S. Chen, A. Bouhon, R.-J. Slager, and B. Monserrat, Manipulation and braiding of Weyl nodes using symmetry-constrained phase transitions (2021).

B. Jiang, A. Bouhon, Z.-K. Lin, X. Zhou, B. Hou, F. Li, R.-J. Slager, and J.-H. Jiang, Nature Physics **17**, 1239 (2021).

B. Peng, A. Bouhon, B. Monserrat, and R.-J. Slager, Nature Communications **13**, 423 (2022a).

B. Peng, A. Bouhon, R.-J. Slager, and B. Monserrat, Physical Review B **105**, 085115 (2022b).

S. Park, Y. Hwang, H. C. Choi, and B.-J. Yang, Nature Communications **12**, 6781 (2021a).

G. F. Lange, A. Bouhon, B. Monserrat, and R.-J. Slager, Physical Review B **105**, 064301 (2022).

F. N. Ünal, A. Bouhon, and R.-J. Slager, Physical Review Letters **125**, 053601 (2020).

B. Lian, F. Xie, and B. A. Bernevig, Physical Review B **102**, 041402(R) (2020a).

B. Lian, Z. Liu, Y. Zhang, and J. Wang, Physical Review Letters **124**, 126402 (2020b).

I. Dana, Y. Avron, and J. Zak, Journal of Physics C: Solid State Physics **18**, L679 (1985b).

J. Herzog-Arbeitman, Z.-D. Song, N. Regnault, and B. A. Bernevig, Physical Review Letters **125**, 236804 (2020).

A. Hatcher, *Vector bundles and k-Theory* (Unpublished, 2003).

A. Bouhon and R.-J. Slager, arXiv 10.48550/ARXIV.2203.16741 (2022).

M. Graf and P. Vogl, Physical Review B **51**, 4940 (1995).

Q. Wu, S. Zhang, H.-F. Song, M. Troyer, and A. A. Soluyanov, Computer Physics Communications **224**, 405 (2018).

A. Alexandradinata and L. Glazman, Physical Review B **97**, 144422 (2018).

C. Wang, W. Duan, L. Glazman, and A. Alexandradinata, Physical Review B **100**, 014442 (2019).

F. Piéchon, A. Raoux, J.-N. Fuchs, and G. Montambaux, Physical Review B **94**, 134423 (2016).

Y. Hwang, J.-W. Rhim, and B.-J. Yang, Nature Communications **12**, 6433 (2021).

J.-W. Rhim, K. Kim, and B.-J. Yang, Nature **584**, 59 (2020).

J. Liu, Z. Ma, J. Gao, and X. Dai, , 1 (2019c).

A. Bouhon, 3-band and 4-band real symmetric tight-binding models with arbitrary Euler class, GitHub (2020).

L. Fidkowski, T. Jackson, and I. Klich, Physical review letters **107**, 036601 (2011).

C. K. Chiu, Y. H. Chan, and A. P. Schnyder, (2018).

M. Z. Hasan and C. L. Kane, Reviews of Modern Physics **82**, 3045 (2010).

R. Takahashi, Y. Tanaka, and S. Murakami, Physical Review Research **2**, 013300 (2020).

Y. Hwang, J. Ahn, and B.-J. J. Yang, Physical Review B **100**, 21 (2019).

L. Trifunovic and P. W. Brouwer, Physical Review X **9**, 011012 (2019).

J.-W. Rhim, J. H. Bardarson, and R.-J. Slager, Physical Review B **97**, 115143 (2018).

J. Ahn, S. Park, D. Kim, Y. Kim, and B. J. Yang, Chinese Physics B **28**, 10.1088/1674-1056/ab4d3b (2019b).

J. Ahn and B.-J. Yang, Physical Review B **99**, 235125 (2019).

D. Bauer, S. Talkington, F. Harper, B. Andrews, and R. Roy, Physical Review B **105**, 045144 (2022).

S. Yao and Z. Wang, Physical Review Letters **121**, 086803 (2018).

K. Zhang, Z. Yang, and C. Fang, Physical Review Letters **125**, 126402 (2020b).

B. Hunt, T. Taniguchi, P. Moon, M. Koshino, and R. C. Ashoori, Science **340**, 1427 (2013).

L. Ponomarenko, R. Gorbachev, G. Yu, D. Elias, R. Jalil, A. Patel, A. Mishchenko, A. Mayorov, C. Woods, J. Wallbank, *et al.*, Nature **497**, 594 (2013).

Z. Hao, A. Zimmerman, P. Ledwith, E. Khalaf, D. H. Najafabadi, K. Watanabe, T. Taniguchi, A. Vishwanath, and P. Kim, Science **371**, 1133 (2021).

J. M. Park, Y. Cao, K. Watanabe, T. Taniguchi, and P. Jarillo-Herrero, Nature **590**, 249 (2021b).

J. M. Park, Y. Cao, L. Xia, S. Sun, K. Watanabe, T. Taniguchi, and P. Jarillo-Herrero, arXiv preprint arXiv:2112.10760 (2021c).

Y. Zhang, R. Polski, C. Lewandowski, A. Thomson, Y. Peng, Y. Choi, H. Kim, K. Watanabe, T. Taniguchi, J. Alicea, *et al.*, arXiv preprint arXiv:2112.09270 (2021).

S. Hahn, K. Kim, K. Kim, X. Hu, T. Painter, I. Dixon, S. Kim, K. R. Bhattarai, S. Noguchi, J. Jaroszynski, *et al.*, Nature **570**, 496 (2019).

Y. Cao, J. M. Park, K. Watanabe, T. Taniguchi, and P. Jarillo-Herrero, Nature **595**, 526 (2021).

G. Chaudhary, A. MacDonald, and M. Norman, Physical Review Research **3**, 033260 (2021).

D. Shaffer, J. Wang, and L. H. Santos, Physical Review B **104**, 184501 (2021).

I. Das, C. Shen, A. Jaoui, J. Herzog-Arbeitman, A. Chew, C.-W. Cho, K. Watanabe, T. Taniguchi, B. A. Piot, B. A. Bernevig, and D. K. Efetov, Physical Review Letters **128**, 217701 (2022).

J. Herzog-Arbeitman, A. Chew, D. K. Efetov, and B. A. Bernevig, arXiv preprint arXiv:2111.11434 (2021).

Y. Sheffer and A. Stern, Physical Review B **104**, L121405 (2021).

A. Kruchkov, Physical Review B **105**, L241102 (2022a).

J. P. Provost and G. Vallee, Communications in Mathematical Physics **76**, 289 (1980).

N. N. Nam and M. Koshino, Physical Review B **96**, 1 (2017).

J. M. B. Lopes Dos Santos, N. M. R. Peres, and A. H. Castro Neto, Physical Review Letters **99**, 0 (2007).

S. Carr, D. Massatt, S. B. Torrisi, P. Cazeaux, M. Luskin, and E. Kaxiras, Physical Review B **98**, 224102 (2018).

A. Altland and M. R. Zirnbauer, Physical Review B **55**, 1142 (1997).

A. Kruchkov, arxiv (2022b).

F. K. Popov and A. Milekhin, Physical Review B **103**, 155150 (2021).

X. Hu, T. Hyart, D. I. Pikulin, and E. Rossi, Physical Review Letters **123**, 237002 (2019).

A. Julku, T. J. Peltonen, L. Liang, T. T. Heikkilä, and P. Törmä, Physical Review B **101**, 060505 (2020).

Z. Wang, G. Chaudhary, Q. Chen, and K. Levin, Physical Review B **102**, 184504 (2020).

M. Sigrist and K. Ueda, Reviews of Modern Physics **63**, 239 (1991).

V. Berezinskii, Soviet Physics–JETP [translation of Zhurnal Eksperimentalnoi i Teoreticheskoi Fiziki] **34**, 610 (1971).

J. M. Kosterlitz and D. J. Thouless, Journal of Physics C: Solid State Physics **6**, 1181 (1973).

D. R. Nelson and J. Kosterlitz, Physical Review Letters **39**, 1201 (1977).

H. Fertig, L. Brey, R. Côté, and A. MacDonald, Physical Review B **50**, 11018 (1994).

F. R. Lux, S. Ghosh, P. Prass, E. Prodan, and Y. Mokrousov, preprint arXiv:2103.01047 (2021).

E. Khalaf, S. Chatterjee, N. Bultinck, M. P. Zaletel, and A. Vishwanath, Science Advances **7**, eabf5299 (2021).

S. Chatterjee, N. Bultinck, and M. P. Zaletel, Physical Review B **101**, 165141 (2020).

Y. H. Zhang and T. Senthil, Physical Review B **99**, 10.1103/PhysRevB.99.205150 (2019).

A. G. Abanov and P. B. Wiegmann, Journal of High Energy Physics **2001**, 030 (2001).

T. Grover and T. Senthil, Physical Review Letters **100**, 156804 (2008).

A. L. Sharpe, E. J. Fox, A. W. Barnard, J. Finney, K. Watanabe, T. Taniguchi, M. A. Kastner, and D. Goldhaber-Gordon, Science **365**, 605 (2019).

M. Serlin, C. Tschirhart, H. Polshyn, Y. Zhang, J. Zhu, K. Watanabe, T. Taniguchi, L. Balents, and A. Young, Science **367**, 900 (2020).

H. Fertig, L. Brey, R. Côté, A. MacDonald, A. Karlhede, and S. Sondhi, Physical Review B **55**, 10671 (1997).

C.-H. Hsu and S. Chakravarty, Physical Review B **87**, 085114 (2013).

N. Nagaosa and Y. Tokura, Nature Nanotechnology **8**, 899 (2013).

Y. Tokura and N. Kanazawa, Chemical Reviews **121**, 2857 (2020).

F. Wu and S. D. Sarma, Physical Review B **102**, 165118 (2020).

T. Bömerich, L. Heinen, and A. Rosch, Physical Review B **102**, 100408 (2020).

P. San-Jose, J. González, and F. Guinea, Physical Review Letters **108**, 10.1103/PhysRevLett.108.216802 (2012).

P. J. Ledwith, G. Tarnopolsky, E. Khalaf, and A. Vishwanath, Physical Review Research **2**, 023237 (2020).

S. Mühlbauer, B. Binz, F. Jonietz, C. Pfleiderer, A. Rosch, A. Neubauer, R. Georgii, and P. Böni, Science **323**, 915 (2009).

S. Plimpton, Journal of Computational Physics **117**, 1 (1995).

A. Kruchkov, preprint arXiv:2105.14672 (2021).

R. King-Smith and D. Vanderbilt, Physical Review B **47**, 1651 (1993).

R. Resta, Europhysics Letters **22**, 133 (1993).

B. Zhang, Nature Physics **15**, 307 (2019).

X. Lu, P. Stepanov, W. Yang, M. Xie, M. A. Aamir, I. Das, C. Urgell, K. Watanabe, T. Taniguchi, G. Zhang, A. Bachtold, A. H. MacDonald, and D. K. Efetov, Nature **574**, 653 (2019).

P. Moon and M. Koshino, Physical Review B **85**, 195458 (2012).

H. S. Arora, R. Polski, Y. Zhang, A. Thomson, Y. Choi, H. Kim, Z. Lin, I. Z. Wilson, X. Xu, J.-H. Chu, *et al.*, Nature **583**, 379 (2020).

A. T. Pierce, Y. Xie, J. M. Park, E. Khalaf, S. H. Lee, Y. Cao, D. E. Parker, P. R. Forrester, S. Chen, K. Watanabe, *et al.*, preprint arXiv:2101.04123 (2021).

Y. Xie, A. T. Pierce, J. M. Park, D. E. Parker, E. Khalaf, P. Ledwith, Y. Cao, S. H. Lee, S. Chen, P. R. Forrester, *et al.*, preprint arXiv:2107.10854 (2021).

C. W. Chen, N. Lera, R. Chaunsali, D. Torrent, J. V. Alvarez, J. Yang, P. San-Jose, and J. Christensen, Advanced Materials **31**, 1 (2019).

G. W. Burg, J. Zhu, T. Taniguchi, K. Watanabe, A. H. MacDonald, and E. Tutuc, Physical Review Letters **123**, 197702 (2019).

C. Shen, Y. Chu, Q. Wu, N. Li, S. Wang, Y. Zhao, J. Tang, J. Liu, J. Tian, K. Watanabe, T. Taniguchi, R. Yang, Z. Y. Meng, D. Shi, O. V. Yazyev, and G. Zhang, Nat. Phys. **16**, 520 (2020).

B. Liu, G. Zhao, Z. Liu, and Z. F. Wang, Nano Letters , acs.nanolett.9b02719 (2019d).

N. Bultinck, E. Khalaf, S. Liu, S. Chatterjee, A. Vishwanath, and M. P. Zaletel, Physical Review X **10**, 031034 (2020).

E. Suárez Morell, J. D. Correa, P. Vargas, M. Pacheco, and Z. Barticevic, Physical Review B - Condensed Matter and Materials Physics **82**, 1 (2010).

F. Haddadi, Q. Wu, A. J. Kruchkov, and O. V. Yazyev, Nano Letters **20**, 2410 (2020).

P. C. Adak, S. Sinha, U. Ghorai, L. D. V. Sangani, K. Watanabe, T. Taniguchi, R. Sensarma, and M. M. Deshmukh, Physical Review B **101**, 125428 (2020).

P. Rickhaus, G. Zheng, J. L. Lado, Y. Lee, A. Kurzmann, M. Eich, R. Pisoni, C. Tong, R. Garreis, C. Gold, M. Masseroni, T. Taniguchi, K. Wantanabe, T. Ihn, and K. Ensslin, Nano Letters **19**, 8821 (2019).

Y. W. Choi and H. J. Choi, Physical Review B **100**, 201402 (2019).

F. J. Culchac, R. R. Del Grande, R. B. Capaz, L. Chico, and E. S. Morell, Nanoscale **12**, 5014 (2020).

N. R. Chebrolu, B. L. Chittari, and J. Jung, Physical Review B **99**, 235417 (2019).

E. Lee, A. Furusaki, and B.-J. Yang, Physical Review B **101**, 241109 (2020).

M. Koshino, Physical Review B **99**, 235406 (2019).

S. Liu, E. Khalaf, J. Y. Lee, and A. Vishwanath, Phys. Rev. Res. **3**, 013033 (2021).

N. Nemec and G. Cuniberti, Physical Review B - Condensed Matter and Materials Physics **75**, 1 (2007).

Y. Hasegawa and M. Kohmoto, Physical Review B **88**, 125426 (2013).

S. Sun, Z. Song, H. Weng, and X. Dai, Physical Review B **101**, 125118 (2020).

K. S. Novoselov, E. McCann, S. V. Morozov, V. I. Fal'ko, M. I. Katsnelson, U. Zeitler, D. Jiang, F. Schedin, and A. K. Geim, Nature Physics **2**, 177 (2006).

A. H. Castro Neto, F. Guinea, N. M. R. Peres, K. S. Novoselov, and A. K. Geim, Rev. Mod. Phys. **81**, 109 (2009).

B. Deng, Z. Pang, S. Chen, X. Li, C. Meng, J. Li, M. Liu, J. Wu, Y. Qi, W. Dang, *et al.*, ACS nano **11**, 12337 (2017).

E. Mariani and F. Von Oppen, Phys. Rev. Lett. **100**, 076801 (2008).

A. Croy, J. Phys. Mater. **3**, 02lt03 (2020).

A. L. de Lima, L. A. Müssnich, T. M. Manhabosco, H. Chacham, R. J. Batista, and A. B. de Oliveira, Nanotechnology **26**, 045707 (2015).

H. Hattab, A. T. N'Diaye, D. Wall, C. Klein, G. Jnawali, J. Coraux, C. Busse, R. van Gastel, B. Poelsema, T. Michely, *et al.*, Nano Lett. **12**, 678 (2012).

Y. Xie, Y. Chen, X. L. Wei, and J. Zhong, Phys. Rev. B **86**, 195426 (2012).

M. Pelc, W. Jaskólski, A. Ayuela, and L. Chico, Phys. Rev. B **92**, 085433 (2015).

Y. Kang, R. Qiu, M. Jian, P. Wang, Y. Xia, B. Motevalli, W. Zhao, Z. Tian, J. Z. Liu, H. Wang, H. Liu, and X. Zhang, Adv. Funct. Mater. **30**, 2003159 (2020).

M. A. H. Vozmediano, F. de Juan, and A. Cortijo, in *Journal of Physics: Conference Series*, Vol. 129 (IOP Publishing, 2008) p. 012001.

L. Ortolani, E. Cadelano, G. P. Veronese, C. Degli Esposti Boschi, E. Snoeck, L. Colombo, and V. Morandi, Nano Lett. **12**, 5207 (2012).

M. M. Benameur, F. Gargiulo, S. Manzeli, G. Autès, M. Tosun, O. V. Yazyev, and A. Kis, Nature communications **6**, 8582 (2015).

Y. Guo and W. Guo, J. Phys. Chem. C **117**, 692 (2013).

V. M. Pereira, A. H. Castro Neto, H. Y. Liang, and L. Mahadevan, Phys. Rev. Lett. **105**, 156603 (2010).

H. Nakajima, T. Morimoto, Y. Okigawa, T. Yamada, Y. Ikuta, K. Kawahara, H. Ago, and T. Okazaki, Sci. Adv. **5**, eaau3407 (2019).

M. I. Katsnelson and M. F. Prokhorova, Physical Review B - Condensed Matter and Materials Physics **77**, 1 (2008).

J. Zhang and E. P. Fahrenthold, Journal of Physical Chemistry Letters **11**, 1378 (2020).

S. Deng and V. Berry, Materials Today **19**, 197 (2016).

M. Wang, M. Huang, D. Luo, Y. Li, M. Choe, W. K. Seong, M. Kim, S. Jin, M. Wang, S. Chatterjee, Y. Kwon, Z. Lee, and R. S. Ruoff, Nature **596**, 519 (2021).

Z. Pan, N. Liu, L. Fu, and Z. Liu, J. Am. Chem. Soc. **133**, 17578 (2011).

M. Lanza, Y. Wang, A. Bayerl, T. Gao, M. Porti, M. Nafria, H. Liang, G. Jing, Z. Liu, Y. Zhang, *et al.*, J. Appl. Phys. **113**, 104301 (2013).

N. Liu, Z. Pan, L. Fu, C. Zhang, B. Dai, and Z. Liu, Nano Res. **4**, 996 (2011).

H. Hu, K. Xia, S. Zhao, M. Ma, and Q. Zheng, Extreme Mech. Lett. **42**, 101104 (2021).

R.-S. Ma, J. Ma, J. Yan, L. Wu, W. Guo, S. Wang, Q. Huan, L. Bao, S. T. Pantelides, and H.-J. Gao, Nanoscale **12**, 12038 (2020).

X. Fan, S.-W. Kim, J. Tang, X. Huang, Z. Lin, L. Zhu, L. Li, J.-H. Cho, and C. Zeng, Nano Lett. **21**, 2033 (2021).

J. C. Rode, D. Zhai, C. Belke, S. J. Hong, H. Schmidt, N. Sandler, and R. J. Haug, 2D Mater. **6**, 015021 (2018).

D. Luo, M. Choe, R. A. Bizao, M. Wang, H. Su, M. Huang, S. Jin, Y. Li, M. Kim, N. M. Pugno, B. Ren, Z. Lee, and R. S. Ruoff, Advanced Materials **34**, 2110509 (2022).

L.-Z. Yang, L.-H. Tong, C.-S. Liao, Q. Wu, X. Fu, Y.-Y. Zhou, Y. Tian, L. Zhang, L. Zhang, M.-Q. Cai, L. He, Z. Qin, and L.-J. Yin, Phys. Rev. Materials **6**, L041001 (2022).

LAMMPS, Molecular dynamics simulator, http://lammps.sandia.gov/.

J. H. Los and A. Fasolino, Physical Review B **68**, 024107 (2003).

A. N. Kolmogorov and V. H. Crespi, Physical Review B **71**, 235415 (2005).

E. Bitzek, P. Koskinen, F. Gähler, M. Moseler, and P. Gumbsch, Phys. Rev. Lett. **97**, 170201 (2006).

J. M. Soler, E. Artacho, J. D. Gale, A. García, J. Junquera, P. Ordejón, and D. Sánchez-Portal, Journal of Physics: Condensed Matter **14**, 2745 (2002).

K. Stokbro, J. Taylor, M. Brandbyge, and P. Ordejon, Annals of the New York Academy of Sciences **1006**, 212 (2003).

J. P. Perdew and A. Zunger, Physical Review B **23**, 5048 (1981).

N. Papior, sisl: v 0.12.3 (2022).

H. S. Lipson and A. Stokes, Proc. R. Soc. A **181**, 101 (1942).

B. Butz, C. Dolle, F. Niekiel, K. Weber, D. Waldmann, H. B. Weber, B. Meyer, and E. Spiecker, Nature **505**, 533 (2014).

M.-Y. Ni and K. Wakabayashi, Japanese Journal of Applied Physics **53**, 06JD03 (2014).

S. M. Gilbert, T. Pham, M. Dogan, S. Oh, B. Shevitski, G. Schumm, S. Liu, P. Ercius, S. Aloni, M. L. Cohen, *et al.*, 2D Materials **6**, 021006 (2019).

K. ichi Sasaki, S. Murakami, and R. Saito, Journal of the Physical Society of Japan **75**, 074713 (2006).

G. W. Semenoff, Physica Scripta **T146**, 014016 (2012).

P. San-Jose, R. V. Gorbachev, A. K. Geim, K. S. Novoselov, and F. Guinea, Nano Lett. **14**, 2052 (2014).

F. Gargiulo and O. V. Yazyev, Nano Lett. **14**, 250 (2014).

M. Büttiker, Phys. Rev. Lett. **57**, 1761 (1986).

O. V. Yazyev and S. G. Louie, Nat. Mater. **9**, 806 (2010).

T. Neupert, L. Santos, C. Chamon, and C. Mudry, Phys. Rev. Lett. **106**, 236804 (2011).

H. Tian, X. Gao, Y. Zhang, S. Che, T. Xu, P. Cheung, K. Watanabe, T. Taniguchi, M. Randeria, F. Zhang, *et al.*, Nature **614**, 440 (2023).

Yifei Guan

Date of Brith	1996-03-25
Office Address:	PH H2 454, EPFL 1015 Lausanne, Switzerland
E-mail:	yifei.guan@epfl.ch

Education

- 2019-Present: EPFL, Switzerland
  - PhD on Physics
    Date of oral exam: 30-05-2023
- 2014-2018 University of Electronic Sci.&Techs of China;
  - BEng. on Electronics Engineering

Experience

Research

- EPFL, Chair of Computational Condensed Matter Physics, Lausanne (04.2019-Present)
  Doctoral assistant
  Supervisor: Prof. Oleg Yazyev
- EPFL, Chair of Computational Condensed Matter Physics, Lausanne (06.2018-10.2018)
  Internship
  Supervisor: Prof. Oleg Yazyev
  - Computational study of band structure of twisted bilayer graphene for rigid and relaxed models.
  - Reveailing some new behaviors of Landau levels of twisted bilayer graphene.
- **Electronic state of local disorders in periodic graphene grain boundaries.** (07.2016-07.2017)
  Beijing National Laboratory for Condensed Matter Physics and Institute of Physics, CAS
  Supervisor: Prof. Guangyu Zhang
  - Computational study about bound states of point defects embedded in a periodic graphene grain boundary.
- **Graphene-based radio frequency devices**. (07.2016-07.2017)
  Beijing National Laboratory for Condensed Matter Physics and Institute of Physics, CAS
  Supervisor: Prof. Guangyu Zhang; Collaborator: Jinchen Wang
  - Contributed to the theoretical analysis and calculation on impedence properties of graphene. Particularly calculated RF impedence with Kubo formula.
- **Research project on phase transitions** (06.2015-06.2016)
  Supervisor: Dr. Yachun Gao
  - Investigated percolation transition in a complex network with classical interactions.

Teaching and Supervision

- EPFL

Quantum physics III	2021-2022, 2022-2023
Computational physics III	2019-2020, 2021-2022
Quantum transport in mesoscopic systems	2020-2021
Solid state physics I	2019-2020, 2020-2021

- In UESTC

Introductory Programming	2017-2018

Software Development

- Participant of the computational pack **WannierTools** project. homepage: `http://www.wanniertools.com/`
    - Contributed to the Landau level subroutines, which find out the electronic energy levels of materials under magnetic fields.

Research Interests

- Topological aspects of low-dimensional materials
- Defected materials and nanostructures
- Properties of self-assembled structures
- Interaction in topological materials

Publications

1. *Kekulé vortex in graphene*
   Yifei Guan, C. Dutreix, H. González-Herrero, M. M. Ugueda, I. Brihuega, M. I. Katsnelson, O. V. Yazyev*, and Vincent T. Renard*
   submitted to journal
2. *Symmetry and topology of hyperbolic Haldane models*
   `http://arxiv.org/abs/2304.03273`
   Anffany Chen, **Yifei Guan**, Patrick M. Lenggenhager, Joseph Maciejko, Igor Boettcher and Tomáš Bzdušek
3. *Bulk-boundary correspondence of topological Euler insulators*
   Yifei Guan, Adrien Bouhon and Oleg V. Yazyev
   Submitted to PRL
4. *Electronic transport in graphene with out-of-plane disorder*
   Yifei Guan and Oleg Yazyev†
   `https://arxiv.org/abs/2210.16629`
5. *Engineering SYK interactions in disordered graphene flakes under realistic experimental conditions*
   Marta Brzezinska*, **Yifei Guan***, Oleg V. Yazyev, Subir Sachdev, Alexander Kruchkov
   `https://arxiv.org/abs/2208.01032` (Accepted by Physical Review Letters)
6. *Re-entrant magic-angle phenomena in twisted bilayer graphene in integer magnetic fluxes*
   Yifei Guan, Oleg V. Yazyev, Alexander Kruchkov
   `https://doi.org/10.1103/PhysRevB.106.L121115`

7. *Unconventional Flat Chern Bands and 2e Charges in Skyrmionic Moiré Superlattices*
   Yifei Guan, Oleg V. Yazyev, Alexander Kruchkov
   Nano Letters, doi: 10.1021/acs.nanolett.3c00121
8. *Landau Levels of the Euler Class Topology*
   Yifei Guan*, Adrien Bouhon*, Oleg V. Yazyev
   `https://doi.org/10.1103/PhysRevResearch.4.023188`
9. *Landau Levels as a Probe for Band Topology in Graphene Moiré Superlattices*
   QuanSheng Wu, Jianpeng Liu, Yifei Guan, and Oleg V. Yazyev
   https://link.aps.org/doi/10.1103/PhysRevLett.126.056401

Manuscript in preparation

1. *Gap opening with magnetic field and electric field in twist bilayer graphene*
   Yifei Guan, Quansheng Wu and Oleg Yazyev
2. *Twisted bulk-boundary correspondence of fragile crystalline and Euler topological insulators*
   Tomáš Bzdušek , Aleksandra Nelson, **Yifei Guan**, Robert-Jan Slager, and Adrien Bouhon
3. *Direct mesoscopic and atomic electric field imaging of moiré heterostructures*
   Edoardo Lopriore, Mukesh Tripathi, Fedele Tagarelli, Marta Brzezińska, **Yifei Guan**, Hyun Goo Ji, Oleg V. Yazyev, Andras Kis

Theses and Contributions to books

1. Bachelor thesis: Photonic crystal and quasi-crystal structures and their light-trapping performance
   – Generated several basic photonic crystal and quasicrystals by projection algorithm.
   – Find out the optical properties of the structures by simulation.
2. Doctoral thesis: Topological effects in carbon-based 2D nanostructures